Dissertation

submitted to the
Combined Faculties of the Natural Sciences and Mathematics
of the Ruperto-Carola-University of Heidelberg, Germany
for the degree of
Doctor of Natural Sciences

Put forward by
Alexander Blättermann, M.Sc.
born in Halle (Saale)

Oral examination: January 13th, 2016

Impulsive control of the atomic dipole response in the time and frequency domain

Referees: **Prof. Dr. Thomas Pfeifer**
PD. Dr. Adriana Pálffy-Buß

Impulsive Kontrolle der atomaren Dipolantwort in der Zeit- und Frequenzdomäne — Die Dipolantwort eines angeregten Quantensystems gewährt direkten Einblick in die Elektronendynamik, die vom einfallenden Licht in Bewegung gesetzt wird. Spectroskopiemethoden wie die zeitaufgelöste Absorptionsspektroskopie nutzen die Tatsache, dass die Dipolantwort einen charakterisitschen Fingerabdruck im Spektrum des transmittierten Lichts hinterlässt. In dieser Arbeit wird ein allgemeines und leichtverständliches Modell vorgestellt, das es erlaubt die Dipoldynamik die von zwei ultrakurzen Lichtpulsen ausgelöst und manipuliert wird analytisch zu beschreiben. Die Beschreibung findet sowohl in der Zeit- als auch in der Frequenzdomäne statt. Darauf basierend wird eine zweidimensionale Spektraldarstellung der zeitaufgelösten Absorptionsspektren entwickelt, mit deren Hilfe sich verschiedene Mechanismen der Licht-Materie-wechselwirkung trennen und gezielt untersuchen lassen. Dies wird experimentell durch die Untersuchung von elektronischen Wellenpakten in doppelt-angeregtem Helium und in innervalenz-angeregtem Xenon demonstriert.
Zudem wird eine Methode zur in situ Charakterisierung der intensiven Laserpulse, welche zur Manipulation der Elektronendynamik des Quantensystems eingesetzt werden, vorgestellt und experimentell angewendet. Die Möglichkeit diese ultrakurzen und intensiven Laserpulse direkt in der Spektroskopieprobe zu analysieren erlaubt es die Elektronendynamik präzise zu vermessen und zu kontrollieren, sowie die Vergleichbarkeit von Experiment und Theorie zu verbessern.

Impulsive control of the atomic dipole response in the time and frequency domain — The dipole response of an excited quantum system gives direct insight into the electron dynamics triggered by the incoming light. Spectroscopy techniques such as (attosecond) transient absorption spectroscopy make use of the fact that the dipole response leaves its characteristic fingerprint on the transmitted light. In this work, a general and comprehensive model is introduced, which allows for an analytic description of dipole dynamics triggered and modified by two ultrashort light pulses in both time and frequency domains. Based on this description, a two-dimensional spectral representation of time delay–resolved absorption data is developed. The power of the method to separate different pathways of light–matter interaction, which allows for their individual investigation, is demonstrated experimentally by studying electronic wave packet dynamics in doubly excited helium and inner-valence excited xenon.
Furthermore, an *in situ* technique for characterization of the intense dressing laser pulse that drives (nonlinear) quantum dynamics in time-resolved absorption experiments is derived from the same analytic model and demonstrated experimentally. The possibility to characterize these ultrashort strong-field laser pulses directly within the spectroscopy target enhances the scope of transient absorption spectroscopy as it allows for the precise measurement and control of electron dynamics and increases the comparability between experiment and theory.

List of Publications

Parts of this work have been published or prepared in the following references:

A. Blättermann, C. Ott, A. Kaldun, T. Ding and T. Pfeifer.
Two-dimensional spectral interpretation of time-dependent absorption near laser-coupled resonances.
J. Phys. B: At. Mol. Opt. Phys. **47**, 124008 (2014).
(for additional information see [1])

A. Blättermann, C. Ott, A. Kaldun, T. Ding, V. Stooss, M. Laux, M. Rebholz and T. Pfeifer.
In situ characterization of few-cycle laser pulses in transient absorption spectroscopy.
Opt. Lett. **40**, 3464–3467 (2015).
(for additional information see [2])

Further publications with own contributions:

C.-T. Chiang, A. Blättermann, M. Huth, J. Kirschner, and W. Widdra.
High-order harmonic generation at 4MHz as a light source for time-of-flight photoemission spectroscopy.
Appl. Phys. Lett. **101**, 071116 (2012).
(for additional information see [3])

C.-T. Chiang, A. Blättermann, M. Huth, J. Kirschner, and W. Widdra.
Oscillator-based High-order Harmonic Generation at 4MHz for Applications in Time-of-Flight Photoemission Spectroscopy.
EPJ Web of Conferences **41**, 01019 (2013).
(for additional information see [4])

A. Blättermann, Cheng-Tien Chiang, J. Kirschner, and W. Widdra.
Atomic line emission and high-order harmonic generation in argon driven by 4-MHz sub-μJ laser pulses.
Phys. Rev. A **89**, 043404 (2014).
(for additional information see [5])

C. Ott, A. Kaldun, L. Argenti, P. Raith, K. Meyer, M. Laux, Y. Zhang, A. Blättermann, S. Hagstotz, T. Ding, R. Heck, J. Madrõnero, F. Martin and T. Pfeifer.
Reconstruction and control of a time-dependent two-electron wave packet.
Nature **516**, 374-378 (2014).
(for additional information see [6])

A. Kaldun, C. Ott, A. Blättermann, M. Laux, K. Meyer, T. Ding, A. Fischer, and T. Pfeifer.
Extracting Phase and Amplitude Modifications of Laser-Coupled Fano Resonances.
Phys. Rev. Lett. **112**, 103001 (2014).
(for additional information see [7])

V. Stooß, A. Kaldun, C. Ott, A. Blättermann, T. Ding, and T. Pfeifer.
Inversion symmetry breaking of atomic bound states in strong and short laser fields.
arXiv:1506.01182 (2015).
(for additional information see [8])

T. Ding, C. Ott, A. Kaldun, A. Blättermann, K. Meyer, V. Stooß, M. Rebholz, P. Birk, M. Hartmann, A. Brown, H. Van Der Hart, and T. Pfeifer.
Time-resolved four-wave-mixing spectroscopy for inner-valence transitions.
arXiv:1510.08698 (2015).
(for additional information see [9])

Contents

Chapter 1

Introduction

The journey is the reward.

This statement by the ancient Chinese scholar Confucius is deeply enrooted in the nature of many branches of science. It is not only the initial and the final state of a process that are of importance. Very often, it is the course—or the dynamics—of the process itself that is at least of the same importance. Having precise knowledge on the dynamics of processes comprises two great advantages: The insight and the deeper understanding of the process itself, which often proves useful on its own. And second, the possibility to use this knowledge and actively intervene the process to increase its efficiency (if the processes is wanted, e.g. photosynthesis [10]), to block it (if the process is unwanted, e.g. the uncontrolled division of cancer cells [11]) or to tailor the outcome of the process (e.g. in chemical synthesis reactions).
One of the major obstacles in getting insight into the course of a process is the time scale at which the dynamics of the process evolve. Everything that does not occur on the time scale of our normal perception, e.g. a few days to a few milliseconds, needs extra care or tools to be resolved in time. On the large–time scale side are processes like the evolution of the universe or the formation of mountain ranges which span millions to billions of years. This thesis, however, is dedicated to the other extreme of time scales: Electronic processes in atoms (or in ensembles of atoms like molecules or condensed materials) occur on the few-femtosecond (1 fs$= 10^{-15}$ s) and even attosecond (1 as$= 10^{-18}$ s) time scale. One femtosecond is so short that it takes light, which only needs about 1 second to go from the earth to the moon, more than 3300 fs to travel just 1 mm. Further, capturing a single lightning strike (duration $\approx$ 10 ms) with a hypothetical camera that takes one image per femtosecond, it would take 13000 years to watch the full movie (at 24 frames per second). The need to study these processes lies in the fundamental role they play in nature. To name only a few examples, ultrafast electronic processes determine charge migration in organic photovoltaics [12] and chemical bond formation and breaking [13], or could be utilized to establish ultrafast signal processing [14].

Having such incredibly fast dynamics, there is only one well established tool to study electronic process on their natural time scale: ultrashort pulses of light. Traditionally, femtosecond and attosecond light pulses have very different properties based on the

way they are generated. Femtosecond light pulses are usually generated by lasers. The invention of modelocking [15] where typically the Kerr-lens effect is employed [16] boosted the achievable pulse durations to ever shorter values. Further technological achievements made it possible to increase the pulse energy by 5 and more orders of magnitude and to compress these pulses temporally to a few femtoseconds (see Sec. 2.1.2 for details). These—often called strong-field—laser pulses, as their intensity can easily excess $10^{14}\,\mathrm{W/cm^2}$, typically consist of only a few cycles of the electromagnetic carrier wave [17–19]. They are the working horse of what is called strong-field and attosecond physics as they provide enough intensity to drive nonlinear dynamics in the investigated quantum system and they are used to create the even shorter attosecond pulses, which to date provide the ultimate time resolution. The process used to create attosecond pulses from femtosecond pulses is called high-order harmonic generation, which is an extremely nonlinear frequency conversion discovered in 1987 [20]. It typically produces a train of attosecond pulses [21] or with some effort (see Sec. 2.1.3) isolated attosecond pulses [22], which have been reported to fall below durations of 100 attoseconds [19, 23]. Compared with the intense femtosecond pulses, which are usually situated in the visible to near-infrared (NIR) region of the spectrum, the attosecond pulses are located in the extreme-ultraviolet (XUV) and are orders of magnitude less intense. In most experiments, the femtosecond NIR pulse and the attosecond XUV pulse are used in a pump–probe scheme, which can be applied to study and control ultrafast dynamics in atoms [6, 24–26], molecules [27, 28], and solids [14, 29–31]. However, there are also techniques with attosecond resolution were only the NIR pulse is used, e.g. high-harmonic spectroscopy [32–35] or angular streaking [36, 37]. Here, the attosecond timing information is achieved by resolving the cycle structure of the NIR pulse.

In order to deduce dynamical information about the target's response to the short and possible intense laser pulses, a "reaction product" of the light–matter interaction process has to be captured and evaluated. This product can either be a charged particle, e.g. a photoelectron (as in attosecond streaking and angular streaking) or a photoion (as in the reaction microscope), or light, e.g. a linear (as in transient absorption spectroscopy) or a non-linear (as in high-harmonic spectroscopy) optical response.
In the last years, the method of attosecond transient absorption spectroscopy (ATAS) has proven to be very powerful when it comes to measuring bound-state dynamics, because it allows to study the absorption lines of bound–bound transitions, whereas in photoelectron or -ion techniques, an electron has to be liberated from the system in order to generate an observable reaction product. Besides this main difference, there are further advantages of ATAS compared with the other techniques. For example, the intensity of the NIR can be chosen in broad range from zero to weak intensities with perturbative interactions – all the way up to the strong-field regime where the NIR pulses may drive non-linear processes like strong-field ionization. In contrast, methods like high-harmonic spectroscopy and angular streaking require strong-field laser pulses in order to generate a detectable response, which limits the study of targets under more natural weak-field conditions.

The key subject of absorption spectroscopy is the dipole response of the quantum system

with respect to the incident light fields. It contains the information about the system's evolution and manifests itself as a characteristic absorption line in the spectrum of the transmitted light. In order to get the complete picture about the ongoing physics from the measured absorption data, the signature spectral line has to be linked to the dipole response in the time domain, which again has to be connected to the actual quantum dynamics of light–matter interaction.

In this thesis, a universal model is introduced, in which the time-domain evolution of the dipole response under the influence of the two time-delayed light pulses as well as its frequency-domain representation can be treated analytically. The quantum-mechanical process of light–matter interaction is condensed into a single parameter. This draws the connection between the actual physics and the outcome of the experiment, i.e. the absorption spectrum, in a comprehensive way. The key of this model is to treat both light pulses as infinitesimally short Dirac-δ functions. Based on this approach, the effect of the light–matter interaction can be treated as a sudden change of the dipole moment's amplitude and phase. The amount and time-delay dependence of this amplitude and phase jump is modeled according to the process that is to be described.
Based on the mathematical framework of this model, two fundamental improvements to the ATAS technique are introduced within this thesis:

1) Introduction of a two-dimensional–spectral representation of the time delay–resolved data, which allows for a direct separation of different coupling pathways and their specific study.

2) Implementation of an *in situ* method for characterization of the few-cycle NIR pulses directly from measured absorption spectra.

The first method is introduced theoretically and is then applied to investigate the ultrafast dynamics in coherently excited superpositions of quantum states—so called wave packets—under the influence of the dressing NIR laser. The first of two studies can be considered as a proof-of-principle experiment to demonstrate the method. Here, the dynamics of a wave packet of two doubly excited states in helium are studied. The two states are transiently coupled via a two-NIR-photon transition, which leads to a characteristic beating of the time delay–resolved absorbance. This beating is then transferred to the spectral domain, where it is separated from other effects, which allows to precisely determine the beat frequency, the phase that is imprinted by the laser coupling, and the intensity dependence of the effect.
The second study involves states that are created by XUV excitation of an inner-valence electron (4d shell) of xenon to an excited shell (6p). Due to the strong spin–orbit coupling, the two states of different total angular momentum are separated by almost 2 eV. The probing of the coherent wave packet is proposed to be performed by means of strong-field ionization of the excited electron by virtue of intense NIR light. Theoretical calculations predict an effective coupling of the states, which gives rise to a spectral signature of this event. However, under the current experimental conditions, the signature is expected to be very faint if detectable at all. Hence, the power of the two-dimensional–spectral representation to separate this signature from other simultaneously occurring effects plays an important role for detecting this strong-field effect on a spin–orbit wave packet.

The second method that is proposed and demonstrated within this thesis adds another

feature to ATAS: the possibility to characterize the few-cycle strong-field laser pulses *in situ*. Knowledge of the laser-pulse properties is crucial in order to draw quantitative conclusions from measurement results and to steer quantum dynamics in a controlled fashion. So far, only the photoelectron based methods for attosecond spectroscopy had an appropriate technique for pulse characterization, namely attosecond streaking, available. Here, the fact that the NIR laser pulse transiently shifts the energy of XUV-excited states, and thus introduces a shift of the dipole phase, is utilized. By means of the analytical model mentioned before, this phase shift is related to the transformation of the absorption line, and can thus be extracted from measured spectra. Therefore, the pulse properties are determined exactly where the XUV beam and the NIR beam intersect with the spectroscopy target—or in other words—where the quantum dynamics experiment is performed. This information can directly be used to increase the comparability between experiment [6, 7, 14, 26, 38–42] and theory [43–45].

This thesis is structured the following way: In Chap. 2, the fundamental physics of light–matter interaction are presented in a condensed fashion. The chapter covers the basics of ultrashort laser pulses, their interaction with a quantum system and the according response of the system. A subsection introduces the helium atom as one of the major spectroscopy targets in this thesis. Afterwards, Chap. 3 introduces the experimental setup that was used to collect the presented experimental results. The central model, which allows to connect the time-domain picture of controlling the dipole moment to the spectral outcome, is explained in Chap. 4. This lays the basis of the two methods presented in the following two chapters. Chapter 5 is devoted to the two-dimensional absorption spectroscopy (2DAS) method, which allows to separate different pathways of light–matter interaction. The second method, *in situ* characterization of few-cycle NIR pulses, is presented in Chap. 6. Finally, the work presented in this thesis is concluded in Chap. 7.

Chapter 2

Fundamentals

This chapter will give an introduction to the fundamental physical aspects of ultrafast atomic physics and light–matter interaction that play a role throughout the thesis. Since ultrashort laser pulses are the key instrument to get access to the time scale of electronic processes in atoms, the first section is devoted to their mathematical description and their experimental realization. Afterwards, a short introduction to the treatment of quantum n-level systems is presented as well as an overview on time-dependent perturbation theory. As the dipole response of a quantum system is the key quantity of all measurements and concepts presented in this work, it is described in the fourth section where also the related quantities of absorption and dispersion are derived. This is followed by the introduction of the ponderomotive potential, which plays an essential role for the pulse characterization technique presented in Chap. 6. Finally, the physics of the helium atom as one of the main spectroscopy targets investigated here is introduced, thereby focusing on the doubly excited manifold and its characteristic Fano resonances.

2.1 Ultrashort pulses of light

In order to access the extremely fast dynamics of electrons in atoms, molecules, and solids, an ultrafast measurement technique is needed. An often used approach is the pump–probe scheme where a pump event triggers ultrafast dynamics in the system under study and a time-delayed probe event probes for the system's response to the pump. In most cases concerning electron dynamics the pump and probe events are interactions of the system with ultrashort laser pulses. As these pulses nowadays can have durations in the femto- and even sub-femtosecond regime, the electron motion can be resolved to a great extend.
In this section, first of all a general formalism for describing ultrashort light pulses will be introduced, and afterwards techniques for the generation of such pulses will be described. Further information can be found in dedicated textbooks [46–48] and review articles [49–51].

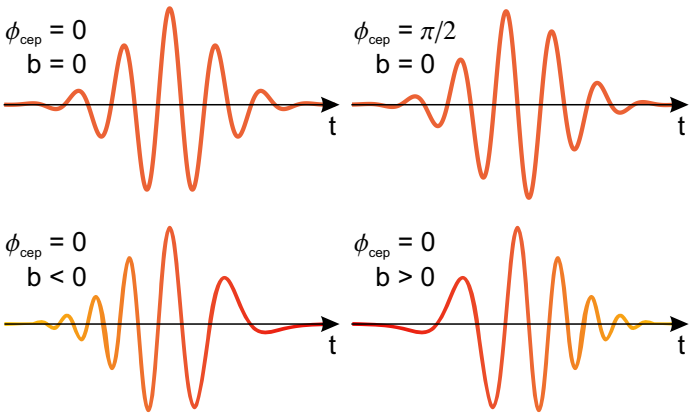

Fig. 2.1: *Schematic of the effect of ϕ_{cep} and b in Eq. 2.2. Panel (a) shows an unchirped cosine waveform whereas (b) shows the corresponding sine waveform which results from a CEP of $\pi/2$. The pulses displayed in the lower panels exhibit a down- (c) and upchirp (d), which results in a frequency sweep across the pulse envelope.*

2.1.1 Mathematical description

A suitable description of ultrashort pulses of linearly polarized light is given by the real-valued one-dimensional electric field as a function of time $E(t)$. In general, $E(t)$ can be decomposed into a term that varies rapidly in time, i.e. the carrier wave, and a term that is slowly variyng in time, i.e. the pulse envelope $\mathscr{E}$:

$$E(t) = \mathscr{E}(t)\cos\left[\phi(t)\right]. \tag{2.1}$$

The shape of the envelope can be complicated, however, for a theoretical treatment it is often approximated by simple analytical functions, e.g. Gaussian, $\cos^2$ or sech^2 (the soliton solution of many laser oscillators). The temporal phase ϕ can usually be written as a power series in t:

$$\phi(t) = \phi_{\mathrm{cep}} + \omega_{\mathrm{c}} t + bt^2 + \ldots \tag{2.2}$$

Here, ϕ_{cep} is the carrier-envelope phase (CEP) of the pulse, which determines the offset between the maximum of the envelope and the crest of the wave cycle. This parameter becomes important for pulses that consist only of a few optical cycles, i.e. the envelope width is of the same order as the optical cycle, so that the CEP really determines the wave form of the electric field and its intensity distribution. The carrier frequency ω_{c} is the center oscillation frequency of the wave, and b is the so-called chirp parameter, which determines the modulation of the frequency across the pulse. One can define the instantaneous frequency as the effective speed at which the phase changes:

$$\omega_{\mathrm{inst}} = \frac{\mathrm{d}\phi(t)}{\mathrm{d}t} = \omega_{\mathrm{c}} + 2bt + \ldots, \tag{2.3}$$

which shows that for $b > 0$ the frequency linearly shifts upwards across the pulse (upchirp), whereas for $b < 0$ the frequency shifts downward (downchirp). If a pulse is chirped, its time $\times$ bandwidth product is not minimized, which means the pulse is not compressed to the minimum duration supported by the spectral bandwidth. The effect of these parameters is displayed in Fig. 2.1. An alternative description of the laser pulse is possible in the frequency domain and is given by the Fourier transform of $E(t)$:

$$\tilde{E}(\omega) = \int_{-\infty}^{\infty} E(t) e^{i\omega t}\,\mathrm{d}t. \tag{2.4}$$

The spectrum $\tilde{E}(\omega)$ is a complex function, which is symmetric around $\omega = 0$ because $E(t)$ is real-valued, and which can in general be written in terms of an amplitude and phase:

$$\tilde{E}(\omega) = \tilde{\mathscr{E}}(\omega) e^{i\tilde{\phi}(\omega)}. \tag{2.5}$$

Similar to Eq. 2.2, the spectral phase $\tilde{\phi}(\omega)$ is also usually expanded as power series about the carrier frequency:

$$\tilde{\phi}(\omega) = \tilde{\phi}_0 + \tau(\omega - \omega_c) + \tilde{b}(\omega - \omega_c)^2 + ... = \tilde{\phi}_0 + \tau\Omega + \tilde{b}\Omega^2 + ... \tag{2.6}$$

with $\Omega = \omega - \omega_c$. The first two terms do not affect the pulse duration or shape. In fact, a phase term linear in ω is equal to retardation of the pulse by a time τ. The third term of the power series, however, represents a linear chirp of the pulse and causes temporal broadening in the time domain representation. In the following τ and $\tilde{b}$ will be related to the well-known group delay (GD) and group delay dispersion (GDD) that occur when a pulse traverses a (linear) medium.

The propagation of light in a dielectric medium is governed by the wave equation, the frequency space representation of which is the optical Helmholtz equation

$$\left[\frac{\partial^2}{\partial z^2} + \omega^2 \varepsilon(\omega)\mu_0\right] \tilde{E}(\omega, z) = 0 \tag{2.7}$$

where ε is the dielectric constant of the material and μ_0 the vacuum permeability. For a given electric field $\tilde{E}(\omega, 0)$ at the beginning of the medium, the general solution to Eq. 2.7 is given by

$$\tilde{E}(\omega, z) = \tilde{E}(\omega, 0) e^{-ik(\omega)z} \tag{2.8}$$

with

$$k(\omega)^2 = \omega^2 \varepsilon(\omega)\mu_0. \tag{2.9}$$

The wave vector $k(\omega)$ can be expanded about the carrier frequency ω_c yielding

$$k(\Omega) = k_c + \left.\frac{\mathrm{d}k}{\mathrm{d}\omega}\right|_{\omega_c} \Omega + \frac{1}{2}\left.\frac{\mathrm{d}^2 k}{\mathrm{d}\omega^2}\right|_{\omega_c} \Omega^2 + ... \tag{2.10}$$

Here, the first-order coefficient $\mathrm{d}k/\mathrm{d}\omega|_{\omega_c}$ is the inverse group velocity (GV) v_g and the second-order coefficient is related to the group velocity dispersion (GVD):

$$\left.\frac{\mathrm{d}^2 k}{\mathrm{d}\omega^2}\right|_{\omega_c} = -\frac{1}{v_g^2}\left.\frac{\mathrm{d}v_g}{\mathrm{d}\omega}\right|_{\omega_c}. \tag{2.11}$$

By comparing Eq. 2.10 to Eq. 2.6 expressions for the GD and GDD can be determined:

$$\tau = \frac{1}{v_g} z \tag{2.12}$$

$$\tilde{b} = -\frac{1}{2v_g^2}\left.\frac{\mathrm{d}v_g}{\mathrm{d}\omega}\right|_{\omega_c} z \tag{2.13}$$

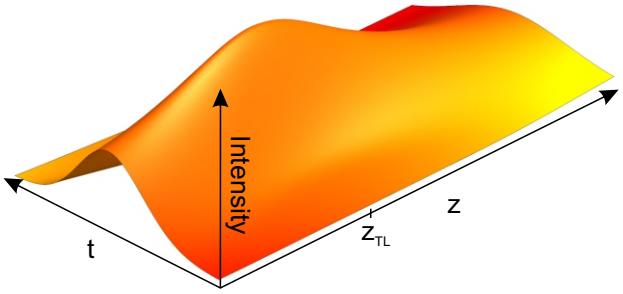

Fig. 2.2: *Influence of a dispersive medium on the pulse intensity profile. The initial chirp of the pulse is compensated by the medium's GDD at z_{TL}. Afterwards the overcompensation sets in and leads to temporal broadening of the pulse.*

This means that in addition to a delay of the pulse, i.e. the GD, every optical element that has a non-vanishing GVD will add a certain amount of GDD and will thus introduce or eliminate—depending on the sign of the GDD—a chirp of the pulse. This in turn will lead to a modified pulse duration. To give an example, a 1 mm thin fused-silica window introduces a GDD of $+35\,\mathrm{fs}^2$ at 800 nm. This means that the spectral components next to 800 nm are delayed by 35 fs per petahertz with respect to the 800 nm part of the spectrum. The broader the spectrum the more delay between the spectral components is encountered, so that for short pulses with a broad spectrum this amount of glass already has tremendous effects. The situation is depicted in Fig. 2.2 where an initially upchirped pulse is travelling in a medium with positive GVD. At a certain distance z_{TL} the initial chirp is compensated for by the GDD introduced by the medium: the pulse is transform limited. After that point the pulse starts to accumulate a net positive GDD and becomes broader again. This is a typical situation when the chirp of a pulse is defined by a chirped-mirror compressor, which is usually designed to overcompensate the incoming chirp. Afterwards a pair of glass wedges is used for fine tuning the net GDD of the compressor setup.
In addition to the second-order dispersion described here in detail, higher orders of dispersion, starting at third-order dispersion (TOD), have to be taken into account for practical pulse compression below ≈ 30 fs. As shown in Fig. 2.3, TOD does not only stretch the pulse, it also introduces distortions of the pulse shape as it introduces asymmetry and pre or post pulses.
In the following, the experimental generation of femto- and attosecond light pulses is discussed.

2.1.2 Generation of intense femtosecond laser pulses

The following section will give a short introduction to modern femtosecond laser pulse generation. The focus lies on the titanium sapphire (Ti:sa) technology, as this is currently the basis for most state-of-the-art strong-field and attosecond experiments and was used to obtain the results of this thesis. While this section provides a general overview of principals and fundamentals of laser pulse generation, Sec. 3.2 deals with the specific laser system used in the experiments of the later chapters.

The basis of such a laser system is the broadband femtosecond oscillator, which provides the initial seed pulses that are later amplified [52, 53]. Pulsed operation is commonly achieved via passive modelocking—a technique where a large number of the resonator's longitudinal modes are forced to oscillate in phase, so that the superposition results in a

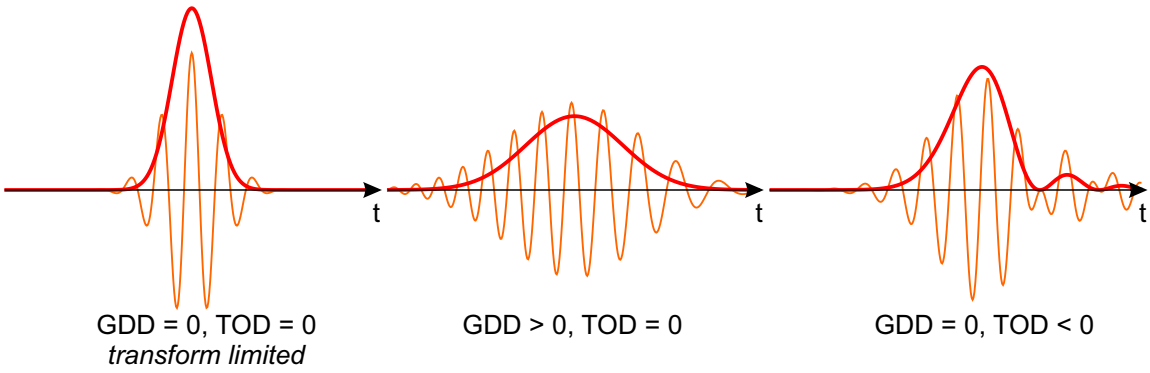

Fig. 2.3: *Comparison of the electric field (orange, thin) and intensity (red, thick) of transform limited and chirped Gaussian pulses. As discussed previously a non-zero GDD causes a frequency chirp and leads to pulse broadening and consequently a reduction of the peak intensity while the intensity profile remains Gaussian. In contrast, TOD introduces distortions to the pulse shape including asymmetry and in this case a post pulse.*

train of pulses separated by the repetition rate. To ensure stable operation, a mechanism is necessary that favors pulsed over continuous operation. Such a mechanism is called self-amplitude modulation (SAM) and practically often achieved via Kerr-lens modelocking (KLM). Here, for the high peak power mode caused by pulsed operation, the nonlinear Kerr effect leads to self-focusing (Fig. 2.4 (a)) and thereby increases the round-trip gain compared with the weak-power mode in continuous operation. This difference in gain is usually achieved by a better overlap with the pump volume due to the spatial confinement as a result of self-focusing. Stable operation starts from noise: a pulse spontaneously formed inside the cavity will experience greater net gain than the other modes and will thus grow to a stable pulse after several round-trips. If the pulse, for instance, accumulates a long leading or trailing edge, those weak-power parts of the pulse will experience poor self-focusing, and therefore less gain than the high-power center part of the pulse. Hence, KLM helps to maintain a short pulse. In fact, KLM or in general SAM is the only mechanism that provides stabilization of the pulse, making it one of the most important intra-cavity processes.

Since the pulse duration is ultimately limited by the spectral bandwidth, the laser transition must be broad in order to achieve short pulses, which makes Ti:sa a very attractive material. The fluorescence peaks around 1.59 eV (780 nm) and has a bandwidth of almost 0.4 eV [52]. However, to get to the few-femtosecond regime, additional spectral broadening has to be performed. This is done by self-phase modulation (SPM), which is (like SAM) caused by the Kerr effect inside the Ti:sa crystal (Fig. 2.4 (b)). As spectral broadening is accompanied by the accumulation of spectral phase (positive GDD around the carrier wavelength), a compression mechanism with negative GDD has to be present in the cavity in order to maintain a short pulse. Chirped mirrors are ideal tools for this task as they can directly replace normal mirrors without the need for additional optics. In principle, chirped mirrors are multilayer mirrors where the periodicity of the layers depends on the position along the mirror's normal direction [54]. This leads to a wavelength dependent penetration depth or time delay, and therefore, introduces a chirp (mostly GDD). As most materials exhibit positive GDD, chirped mirrors are usually designed in order to introduce negative GDD. The interplay of SAM, SPM and negative GDD can lead to a

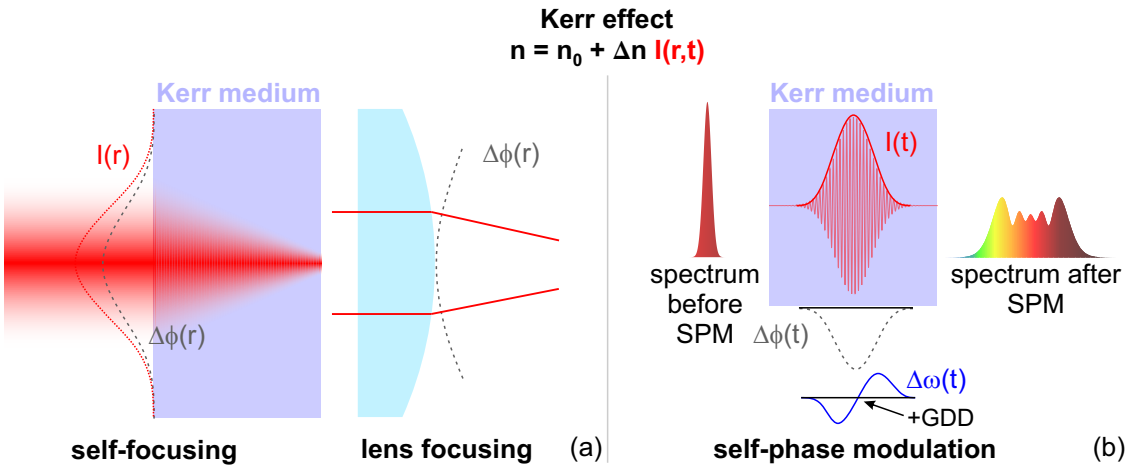

Fig. 2.4: *Two consequences of the nonlinear Kerr effect, which introduces an intensity dependence of the refractive index. (a) Self-focusing or Kerr lensing as a result of the spatial intensity distribution. The additional phase $\Delta\phi(r)$ is proportional to the beam intensity profile, leading to a curved phase front. This has a similar effect as the glass-thickness distribution in an ordinary focusing lens (right) and causes focusing of the beam. (b) Self-phase modulation as a result of the temporal intensity distribution. Here, $\Delta\phi(t)$ follows the pulse intensity, which introduces additional spectral components $\Delta\omega$ increasing the spectral bandwidth. The temporal distribution of the added frequencies across the pulse envelope means that the spectrally broadened pulse is chirped. Around the center frequency, the chirp is almost linear and resembles the accumulation of +GDD.*

stable generation of pulses in the sub-6 fs regime [55, 56].

In order to drive highly nonlinear processes like high-order harmonic generation (HHG) the pulse energy delivered by typical femtosecond oscillators is usually not sufficient (for a few exceptions see e.g. Ref. [3,5,57,58]) in order to reach the peak intensities of roughly 10^{14} W/cm^2 necessary for these processes. Therefore, the pulses have to be amplified in a separate step. As direct amplification of the ultrashort pulses would lead to damage in the amplifier gain medium, the pulses are stretched to the pico- or nanosecond level prior to amplification and are recompressed afterwards. This concept is called chirped pulse amplification (CPA) [59] and is very successful for generating multi-mJ pulses down to 20 fs [60]. The stretcher unit usually consists of massive glas blocks, in which positive GDD as well as higher order dispersion is accumulated. The recompression is done with the help of prism or grating compressors, which are able to compensate for the previously added GDD. TOD accumulated in the glass is compensated by means of special TOD mirrors, which leave the GDD introduced by the stretcher almost unaffected but reduce the unwanted TOD [61]. The amplification step in between is straight-forward: the stretched pulses are sent multiple times through a gain medium, usually a Ti:sa crystal pumped by a nanosecond-pulsed pumplaser (commonly a few kHz repetition rate, several 10 watts output power), until saturation sets in. There are two common designs for the amplification stage: the multipass amplifier where the geometry defines a fixed number of passes through the gain medium, and the regenerative amplifier, which is built like a cavity from which the pulse is released at a certain number of round-trips. If the final amplification has to be further increased a second amplification stage might be used to boost the pulse energy. Since the thermal load in the gain medium is a limiting factor, the achievable

average power is limited to a few to ≈ 20 W. Hence, the repetition rate has to be dropped to the kHz level if mJ pulse energies are desired. This can be done by selecting individual pulses at the repetition rate of the kHz pump laser, which then experience (and deplete) the gain in the pumped medium, whereas the majority of the pulses is dumped. In practice, this can be done by means of a Pockel's cell synchronized to the kHz pump laser and the oscillator pulse train.
Since it is not possible to uniformly amplify the complete bandwidth of the oscillator (because of a process called gain narrowing) the achievable duration of the amplified pulses is considerably longer compared with the oscillator output. To get into the few-cycle regime, the spectrum has to be broadened sufficiently. The most direct approach is to broaden the spectrum via SPM in a noble gas. This can be done either in a gas-filled hollow-core fiber, which creates a high power mode inside the hollow core, and thus, makes SPM efficient [62,63], or by using the effect of filamentation where an interplay of self-focusing and plasma defocusing sustains an extended zone of high intensity without the need for a wave guide [64,65]. After spectral broadening, the acquired spectral phase has to be compensated, which is preferably done by means of a chirped mirror compressor and a pair of glass wedges [66]. Depending on the achieved bandwidth and the ability to compress the pulses, typical pulse durations range from 10 down to 4 fs [18,19]. The result of the spectral broadening depends on many aspects such as

- gas species (mostly noble gases like neon and argon)
- gas pressure (in the regime of a few bar)
- medium length (typically about 1 m)
- peak intensity (determined by many factors, e.g. input power, beam quality, fiber inner-diameter ...)

and can lead to spectra spanning almost two optical octaves. As it is not possible to design chirped mirrors for such large bandwidths, an approach called light synthesis was demonstrated [67], which divides the bandwidth in several spectral channels, compresses each channel separately, and then recombines them to produce optical pulses shorter than 1 fs [68]. An alternative approach uses the concept of optical parametric amplification (OPA) and the related optical parametric chirped-pulse amplification (OPCPA). Also here, different spectral channels can be set up and individually amplified and compressed, which is also promising to produce sub-cycle light pulses [69].
Once the few-cycle pulses have been generated, they can be utilized as a driver for the generation of even shorter pulses at higher photon energy as shown below, or they can be used in the actual experiment as pump or probe in the pump–probe scheme.

2.1.3 Generation of XUV light and attosecond pulses

In order to access electron dynamics in excited states, many atomic systems require photon energies in the order of several 10 eV or more, i.e. in the XUV or soft x-ray spectral region. Typical scenarios for the use of this kind of light are the excitation of several

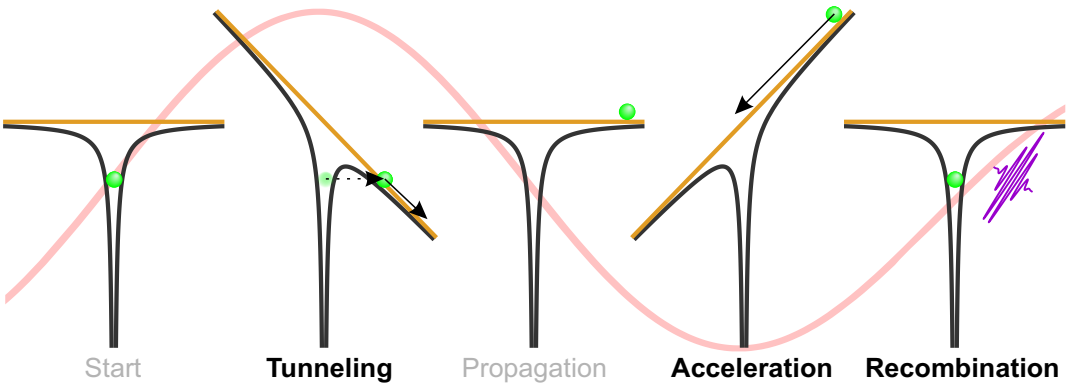

Fig. 2.5: *The 3-step model with the main steps tunneling, acceleration and propagation. The atomic potential bent by the strong laser field (red curve) is shown in black and the linear potential of a dipole in the laser field is shown in orange. The arrows indicate motion of the electron (green) and the emitted burst of XUV light is drawn in violet.*

electrons at once (so-called doubly excited states) and the excitation of strongly bound electrons from inner-valence or core states. Preferably this light should come in the form of pulses, which are short enough to resolve the electronic motion on its natural attosecond time scale. The well known process of high-order harmonic generation (HHG) is able to satisfy both needs [50,51]. In the last years, both photon energies exceeding 1 keV [70] as well as pulse durations of less than 100 as [19,23] have been demonstrated. The HHG process is a highly nonlinear quantum-mechanical process, however, its principle idea can be understand in terms of a quasi-classical picture—the 3-step model—introduced by Corkum in 1993 [71] and illustrated in Fig. 2.5. In order to achieve HHG, typically a noble gas target is exposed to the strong electric field of a femtosecond laser pulse with intensities on the order of 10^{14} W/cm^2. The electric field of the laser is strong enough to considerably deform the atomic potential, which allows a part of the valence-electron wave function to tunnel into the continuum. This process is called strong-field or more precisely tunnel ionization and can be described theoretically be means of the ADK theory [72,73]. According to this theory the ionization rate is given by

$$w_\mathrm{i} = \omega_\mathrm{A} \left(\frac{2e}{n^*}\right)^{2n^*} \frac{I_\mathrm{P}}{2\pi n^*} \left(\frac{3\mathscr{E}(t)}{\pi(2I_\mathrm{P})^{3/2}}\right)^{1/2} \left(\frac{2(2I_\mathrm{P})^{3/2}}{\mathscr{E}(t)}\right)^{2n^*-|m|-1} \exp\left[-\frac{2(2I_\mathrm{P})^{3/2}}{3\mathscr{E}(t)}\right] f_{l,m}. \tag{2.14}$$

Here n^* is the effective principle quantum number ($n^*_\mathrm{Ar} = 0.93$) in the underlying hydrogen model (for hydrogen $n^* = 1$), and $\omega_\mathrm{A} = 4.134 \times 10^{16}$/s is the atomic frequency. I_P (in units of Hartree, 1 Hartree = 27.2 eV) is the ionization potential of the studied atomic species, and $\mathscr{E}(t)$ (in units of the atomic field strength 5.142×10^{11} V/m) is the electric-field envelope of the laser. The coefficient $f_{l,m}$ is given by

$$f_{l,m} = \frac{(2l+1)(l+|m|)!}{2^{|m|}\,|m|!(l-|m|)!} \tag{2.15}$$

Species	He	Ne	Ar	Kr	Xe	Rd
$\mathbf{I_P}$ **(eV)**	24.6	21.6	15.8	14.0	12.1	10.7

Table 2.1: *Ionization potentials of the six noble gases.*

where l and m are the quantum numbers of angular momentum. Using the complete electric field $E(t)$ rather than the envelope $\mathscr{E}(t)$, Eq. 2.14 becomes

$$w_{\mathrm{i}} = \omega_{\mathrm{A}} \left(\frac{2e}{n^*}\right)^{2n^*} \frac{I_{\mathrm{P}}}{2\pi n^*} \left(\frac{2(2I_{\mathrm{P}})^{3/2}}{|E(t)|}\right)^{2n^*-|m|-1} \exp\left[-\frac{2(2I_{\mathrm{P}})^{3/2}}{3|E(t)|}\right] f_{l,m}. \tag{2.16}$$

Since Eq. 2.14 is highly nonlinear in the electric field strength of the ionizing laser, the ionization process is confined to only a fraction of the laser half-cycle. As an example, for $I_{\mathrm{P}} = 15.8\,\mathrm{eV}$ (the ionization potential for argon), a peak electric field of 0.05 a.u. (accordingly $8.8 \times 10^{13}\,\mathrm{W/cm^2}$), and a driving-laser wavelength of 730 nm the effective ionization window is just about 250 as long. If the oscillation period of the electric field is short compared to the electronic time scale, e.g. as often in the case of ionization via an X-ray free electron laser, the ionization is described via multiphoton absorption rather than by the tunneling picture of Eq. 2.14 and 2.16 (see also Sec.2.5). Either way, ionization is the first step of the HHG process after which a valence electron is liberated from it's parent ion.

Being in the continuum, the electron experiences the force imposed by the laser electric field and is accelerated away from its parent ion. When the electric field switches sign, the force is reversed and the electron is driven back. Upon recollision, the kinetic energy that the electron has gained in the laser field plus the binding energy can be converted into a high-energy photon (besides other strong-field processes) with

$$\hbar\omega = E_{\mathrm{kin}} + I_{\mathrm{P}}. \tag{2.17}$$

This recombination is the final step in the three-step model. From Eq. 2.17 the choice of noble gases as the generation medium becomes obvious: the higher the ionization potential, the higher the photon energy (see Tab. 2.1 for the ionization potentials). Furthermore, a high ionization potential reduces the generation of plasma, which would introduce strong distortions to the spatial and temporal characteristics of the laser. However, this means in turn that the ionization probability is reduced, which leads to less efficiency of the XUV generation. Quantum mechanically, the high–kinetic-energy continuum wave function of the returning electron interferes with the remaining bound wave function, which leads to an ultrafast and coherent oscillation of the electron density, and thus drives an oscillating dipole moment. This results in the emission of high-energy radiation. The kinetic energy of the returning electron depends on the moment of ionization within the optical cycle. The maximum kinetic energy is gained when the electron is ionized shortly after the crest of the optical half-cycle, as it has a long time for being accelerated back to the ion by the subsequent half-cycle of opposite sign. A classical calculation yields the peak kinetic energy to be

$$E_{\mathrm{kin,\,max}} = 3.17 U_{\mathrm{P}} \tag{2.18}$$

where U_{P} is the ponderomotive potential of the laser, which is described in detail in Sec. 2.5. It is proportional to the laser intensity and wavelength squared. Hence, high

driving laser intensities are necessary to achieve high photon energies. Also, increasing the carrier wavelength of the driving laser leads to higher photon energies, as the acceleration periods become longer. However, this comes at the expense of lower efficiencies. It was shown experimentally that the integrated harmonic yield scales approximately with λ^{-6} to λ^{-7} [74].
Looking at the harmonic spectrum, there is a universal behavior: The spectral intensity typically drops quickly for the first (low-order) harmonics, but then levels out over a broad range—the so-called plateau—before it comes to a sharp *cut-off*, which marks the highest achievable photon energy given by $I_P + 3.17U_P$. The comb-like structure, which the term *harmonics* refers to, is the result of spectral interference: usually the driving laser pulse consists of at least a few half-cycles, each of which leads to the emission of an attosecond burst of XUV light creating a train of attosecond pulses (APT) [21]. The spectrum of each attosecond pulse is continuous but the interference results in a $2\omega_c$ modulation of the spectrum. For the first experiments [20] and many years after, the appearance of such created XUV light in form of odd harmonics of the driving laser was natural. Only when it became possible to isolate a single attosecond pulse in 2001, the harmonic structure of the spectrum disappeared [22]. In order to create an isolated attosecond pulse (IAP), the XUV light generated by only one half-cycle of the driving laser has to be selected, or the XUV emission itself has to be confined to a single half-cycle. The first technique that led to IAPs was to use a few-cycle driving laser pulse of cosine wave form with a high contrast between the center and the neighboring half-cycles, which creates a significant difference between the cut-off energies of each individual half-cycle. By spectrally selecting only those highest photon energies emitted by the center half-cycle, an IAP is created. To date, beside this method called amplitude gating, a variety of other methods has been demonstrated [75].

The major drawback of HHG in gaseous media as a source for XUV light and attosecond pulses is the very low conversion efficiency of about 10^{-4} to 10^{-6}. This currently limits the application of XUV light generated by HHG to linear processes, since the probability of a second- or higher-order XUV-induced process is extremely low. Approaches to generate high harmonics from dense targets, e.g. water droplets [76] or solids [34], are thus promising ways to pursue in the future in order to possibly compete with free electron laser sources in terms of XUV intensity.
In Sec. 3.3, more technical aspects of HHG of the specific experimental setup used in this work are presented.

2.2 The *n*-level system—theoretical foundation for numerical treatment

Since quantum dynamics of excited atoms interacting with strong and short laser pulses are the main topic of this thesis, it is important to understand how quantum systems evolve in time. As there is usually at least one strong-field pulse applied in the pump–probe scenario, perturbative approaches might fail in describing all aspects of light–matter interaction. This makes an exact treatment of the quantum mechanical problem necessary.

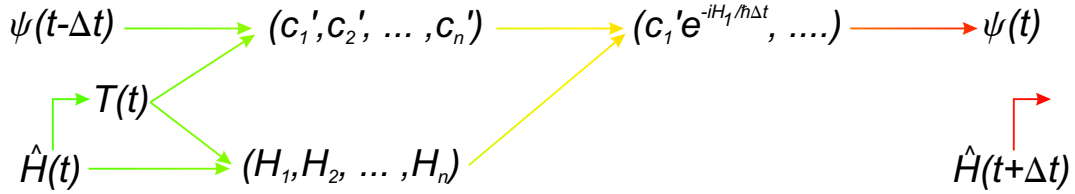

Fig. 2.6: *Principle of numerical treatment of a coupled n-level system. First, the transformation matrix T is determined for the current Hamiltonian, and with its help the transformation to the Eigensystem is performed. Then the Eigenstate is propagated in time, which eventually yields the next time step of the wave function.*

Therefore, this section provides the basics for the numerical simulation of the experiments performed within this work. Such simulations are the key in order to get insight into the physics taking place during the experiment.
In quantum mechanics, a system is defined by its Hamilton operator $\hat{H}$, which determines the system's temporal evolution according to the time-dependent Schrödinger equation

$$\hat{H}\,|\psi\rangle = i\hbar\frac{\partial}{\partial t}\,|\psi\rangle\,. \tag{2.19}$$

Here, $|\psi\rangle$ is the wave function. If the system can be described by a finite number n of descrete states, e.g. if couplings to other states can be neglected, the Hamiltonian can be represented as a Hermitian $n\times n$ matrix and the wave function in terms of an n dimensional state vector:

$$\hat{H} = \begin{pmatrix} E_1 & W_{12} & & W_{1n} \\ W_{21} & E_2 & & W_{2n} \\ & & \cdots & \\ W_{n1} & W_{n2} & & E_n \end{pmatrix} \qquad |\psi\rangle = \begin{pmatrix} c_1(t) \\ c_2(t) \\ \cdots \\ c_n(t) \end{pmatrix}. \tag{2.20}$$

E_j are the energies of the n known unperturbed states, c_j are the complex coefficients of the states, and W_{ij} are the coupling matrix elements between the states i and j. In cases of interaction with a laser pulse that can be described by its electric field $E(t)$, the coupling elements are time-dependent and in the case of a pure dipole interaction may be written as

$$W_{ij}(t) = \langle\psi_i|\,\hat{d}\,|\psi_j\rangle\,E(t) = d_{ij}E(t) \tag{2.21}$$

where $\hat{d}$ is the dipole operator and d_{ij} are the dipole transition matrix elements. In order to solve the time-dependent Schrödinger equation for such a system, one can use the fact that for the Eigensystem of the Hamiltonian, i.e. the representation where $\hat{H}$ is diagonal, the time evolution is trivial: the coefficient c_i' of each Eigenstate is just accumulating a phase which evolves with its respective Eigenfrequency $H_i/\hbar$. The tranformation from the system of the unperturbed states (Eq. 2.20) to the Eigensystem of $\hat{H}$ is done by numerical diagonalization of $\hat{H}$

$$T\hat{H}T^{\dagger} = \begin{pmatrix} H_1 & 0 & & 0 \\ 0 & H_2 & & 0 \\ & & \cdots & \\ 0 & 0 & & H_n \end{pmatrix} \qquad T\begin{pmatrix} c_1 \\ c_2 \\ \cdots \\ c_n \end{pmatrix} = \begin{pmatrix} c_1' \\ c_2' \\ \cdots \\ c_n' \end{pmatrix} \tag{2.22}$$

Here, T and its conjugate transpose $T^\dagger$ are the unitary transformation matrices composed of the Eigenvectors of $\hat{H}$. Since $\hat{H}$ itself is time-dependent, this diagonalization is valid only for an infinitesimally short time interval. Numerically, this time interval has a finite duration Δt and for this duration $\hat{H}$ is assumed to be constant. Therefore, the time step size has to be sufficiently small in order to achieve correct results. For each time step the diagonalization and propagation of the wave function are performed yielding the complete–time-resolved response of the quantum system. The algorithm is sketched in Fig. 2.6.
The finite lifetime of the excited states is introduced empirically by adding an imaginary part $i\Gamma_i$ to the energy values E_i, where Γ_i is the decay rate of the state i taken from literature.
Further details of the specific simulations are described in the respective chapters.

2.3 Time-dependent perturbation theory

In order to simplify calculations and to find analytic expressions in quantum dynamics, the very helpful concept of time-dependent perturbation theory was developed (the derivations are based on Ref. [77], as an English textbook see Ref. [78]). Here, the perturbation $\hat{W}$ in contrast to the general treatment of the previous section is required to be small for the perturbative description to be accurate. In the context of this thesis, this is usually the case when transitions between the ground state and excited states introduced by the attosecond XUV light are considered, or when transitions among excited states by means of weak NIR pulses are considered. The basic idea is to expand the wave function of the perturbed system in terms of the perturbation strength λ, which is used to scale $\hat{W}$. In the following derivation the Schrödinger equation reads

$$i\hbar\frac{\partial}{\partial t}\left|\psi(t)\right\rangle = \left[\hat{H}_0 + \lambda\hat{W}(t)\right]\left|\psi(t)\right\rangle \tag{2.23}$$

where $\hat{H}_0$ is the Hamiltonian of the unperturbed system. The solution of Eq. 2.23 can always be written as a superposition of the Eigenstates $|i\rangle$ (with energy $\hbar\omega_i$ and coefficient $c_i(t)$) of $\hat{H}_0$, which form a complete basis:

$$\left|\psi(t)\right\rangle = \sum_i c_i(t)e^{-i\omega_i t}\left|i\right\rangle. \tag{2.24}$$

Substitution of this Ansatz into Eq. 2.23 yields

$$\sum_i i\hbar\frac{\partial}{\partial t}c_i(t)e^{-i\omega_i t}\left|i\right\rangle = \sum_i c_i(t)e^{-i\omega_i t}\lambda\hat{W}(t)\left|i\right\rangle. \tag{2.25}$$

Projection of this equation onto state $|j\rangle$ cancels the first summation and leads to a system of differential equations for the coeffecients $c_j(t)$:

$$i\hbar\frac{\partial}{\partial t}c_j(t) = \lambda\sum_i c_i(t)e^{i\omega_{ji}t}\left\langle j\right|\hat{W}(t)\left|i\right\rangle. \tag{2.26}$$

Here, $\omega_{ji} = \omega_j - \omega_i$. Up to now, no approximation was made so that Eq. 2.26 is equivalent to Eq. 2.23. The next step is to develop the coefficients c_j as a power series in terms of λ:

$$c_j(t) = c_j^{(0)}(t) + \lambda c_j^{(1)}(t) + \lambda^2 c_j^{(2)}(t) + ... \tag{2.27}$$

Neglecting terms of λ^2 and higher orders, substitution of this expression into Eq. 2.26 yields:

$$i\hbar \frac{\partial c_j^{(0)}(t)}{\partial t} + \lambda i\hbar \frac{\partial c_j^{(1)}(t)}{\partial t} = \lambda \sum_i c_i^{(0)}(t) e^{i\omega_{ji}t} \langle j| \hat{W}(t) |i\rangle. \tag{2.28}$$

By that the assumption $\lambda \ll 1$ was made so that $1 \gg \lambda \gg \lambda^2 ...$. The 0th order expression contains only one term

$$i\hbar \frac{\partial c_j^{(0)}(t)}{\partial t} = 0 \qquad 0^{\text{th}} \text{ order in } \lambda \tag{2.29}$$

which means that the major part $c_j^{(0)}(t)$ of the total coefficient $c_j(t)$ is unaffected by the perturbation and remains constant

$$c_j^{(0)}(t) = c_j^{(0)}(0) = c_j^{(0)}. \tag{2.30}$$

The 1st order expression then reads

$$i\hbar \frac{\partial c_j^{(1)}(t)}{\partial t} = \sum_i c_i^{(0)} e^{i\omega_{ji}t} \langle j| \hat{W}(t) |i\rangle \qquad 1^{\text{st}} \text{ order in } \lambda. \tag{2.31}$$

The solution of this system of differential equation is straight forward since it is decoupled:

$$c_j^{(1)}(t) = -\frac{i}{\hbar} \sum_i c_i^{(0)} \int_0^t e^{i\omega_{ji}t'} \langle j| \hat{W}(t') |i\rangle \, \mathrm{d}t'. \tag{2.32}$$

In the dipole control model, which will be introduced in Chap. 4, the perturbation, i.e. the interaction of the atom with ultrashort laser pulses, is treated as instantaneous and thus defined by a Dirac-δ function $W(t) = W_0 \, \delta_{\text{Dirac}}(t - \tau)$. In turn, the integration in Eq. 2.32 simplifies to:

$$c_j^{(1)}(t) = -\frac{i}{\hbar} \sum_i c_i^{(0)} e^{i\omega_{ji}\tau} W_{ji} \tag{2.33}$$

so that the final expression for the coefficient $c_j(t)$ in first-order perturbation theory with δ-perturbation reduces to

$$c_j(t) = c_j^{(0)} - \lambda \frac{i}{\hbar} \sum_i c_i^{(0)} e^{i\omega_{ji}\tau} W_{ji}. \tag{2.34}$$

For a coupling of only two states this yields

$$c_1(t) = c_1^{(0)} - \lambda \frac{i}{\hbar} c_2^{(0)} e^{i\Delta\omega\tau} W_{12} \tag{2.35}$$

$$c_2(t) = c_2^{(0)} - \lambda \frac{i}{\hbar} c_1^{(0)} e^{-i\Delta\omega\tau} W_{21}. \tag{2.36}$$

This result will be used in the dipole control model to find analytical expressions for the absorption spectrum of perturbatively coupled states.

2.4 The dipole response—absorption and refraction

When an atom is exposed to a light field, an oscillating dipole moment is initiated. Quantum mechanically, a superposition of electronic states, e.g. the ground state and an excited state, is created, which leads to a non-vanishing and oscillating expectation value of the dipole operator. In a classical sense, the electrons are driven by the oscillating electric field $E(t)$ of the light wave, which forces them to perform an oscillatory motion. This initiated dipole oscillation acts back on the original light field in the form of the polarization P, which is described by the wave equation:

$$\left[\frac{\partial^2}{\partial z^2} - \frac{1}{c^2}\frac{\partial^2}{\partial t^2}\right] E(t,z) = \mu_0 \frac{\partial^2}{\partial t^2} P(t,z) \tag{2.37}$$

with c the vacuum speed of light. The right-hand-side of Eq. 2.37, i.e. the dipole accelaration, acts like a source of the electric field: the dipole oscillation creates a field that interferes with the original field and by that mediates the effects of absorption and dispersion. For a linear response of the medium, the general solution to Eq. 2.37 was already obtained in Sec. 2.1.1 by solving the Helmholtz equation, which is the frequency domain representation of the wave equation:

$$\tilde{E}(\omega,z) = \tilde{E}(\omega,0)e^{-ik(\omega)z} \qquad k(\omega)^2 = \omega^2 \varepsilon(\omega)\mu_0. \tag{2.38}$$

Equation 2.37 is connected to Eq. 2.38 by performing a Fourier transform and introducing the linear polarization P in terms of the medium's susceptibility χ:

$$\tilde{P}(\omega,z) = \varepsilon_0 \chi(\omega)\tilde{E}(\omega,z). \tag{2.39}$$

This yields:

$$\left[\frac{\partial^2}{\partial z^2} + \frac{\omega^2}{c^2}(1+\chi(\omega))\right] \tilde{E}(\omega,z) = 0 \tag{2.40}$$

where the definition of the dielectric constant $\varepsilon(\omega) = \varepsilon_0(1+\chi(\omega))$ is used to obtain Eq. 2.38. It is convenient to introduce the susceptibility χ as a complex quantity:

$$\chi(\omega) = \chi'(\omega) + i\chi''(\omega). \tag{2.41}$$

Thus, the wave vector k in Eq. 2.38 can be written as

$$k(\omega) = \frac{\omega}{c}\sqrt{1+\chi'(\omega)+i\chi''(\omega)}. \tag{2.42}$$

The square root term is in general a complex number, the real part of which corresponds to the refractive index n and introduces dispersion, while the imaginary part gives rise to absorption (or gain) and is described by the absorption coefficient α:

$$-\frac{1}{2}\alpha = \mathrm{Im}\left[\frac{\omega}{c}\sqrt{1+\chi'+i\chi''}\right]. \tag{2.43}$$

In the case of a weakly absorbing material ($\chi', \chi'' \ll 1$), e.g. a dilute gas target, the absorption coefficient can be approximated by

$$\alpha \approx -\frac{\omega}{c}\chi''. \tag{2.44}$$

The absorption coefficient as a function of ω can be measured directly via Lambert-Beer's law in an absorption spectroscopy experiment

$$I(z) = I(0)e^{-\alpha z}, \tag{2.45}$$

which also gives access to the related microscopic quantities. The absorption cross-section σ is given by the absorption coefficient α per number density ρ of absorbers, e.g. atoms. Similar, the atomic dipole moment d (in the frequency domain $\tilde{d}$), is related to the macroscopic polarization P by $d = P/\rho$, and to the cross-section via

$$\sigma(\omega) = \frac{\omega}{\varepsilon_0 c}\mathrm{Im}\left[\frac{\tilde{d}(\omega)}{\tilde{E}(\omega)}\right]. \tag{2.46}$$

Thus, measurement of the absorption spectrum gives direct insight into the system's microscopic response. Furthermore, by simulation of the system and its response to laser light, the expected absorption spectrum is readily derived and allows for interpretation of measurement results.
Closely related to these quantities is the optical density (OD), which is commonly used in the absorption-spectroscopy community and defined via

$$I_{\mathrm{out}}(\omega) = I_{\mathrm{in}}(\omega)\, 10^{-\mathrm{OD}(\omega)}. \tag{2.47}$$

2.5 Ponderomotive potential

In strong-field physics, the ponderomotive potential or ponderomotive energy is a key parameter of the laser pulse and is related to—though distinct from—the pulse intensity. A free electron (charge $q_\mathrm{e} = -1.602 \times 10^{-19}\,\mathrm{C}$, mass $m_\mathrm{e} = 9.109 \times 10^{-31}\,\mathrm{kg}$) that is exposed to a laser electric field (amplitude E_0, intensity I, carrier frequency ω_c, carrier wavelength λ_c) is subject to a quivering motion, which raises the electron's energy. The force experienced by the electron results in an acceleration

$$\ddot{x}(t) = \frac{q_\mathrm{e} E(t)}{m_\mathrm{e}}. \tag{2.48}$$

From that, the velocity and the position can be calculated by integration. For a plain wave $E(t) = E_0 \cos(\omega_\mathrm{c} t + \phi)$, the solution can be obtained analytically. Assuming the electron experiences the electric force from time $t = 0$, e.g. due to photoionization at that time, starting at $x(0) = 0$ and with zero initial velocity, the solution to Newton's equation is given by:

$$\dot{x}(t) = \frac{q_\mathrm{e} E_0}{m_\mathrm{e}\omega_\mathrm{c}}\left[\sin(\omega_\mathrm{c} t + \phi) - \sin(\phi)\right] \tag{2.49}$$

$$x(t) = \frac{q_\mathrm{e} E_0}{m_\mathrm{e}\omega_\mathrm{c}^2}\left[-\cos(\omega_\mathrm{c} t + \phi) + \cos(\phi)\right] - \frac{q_\mathrm{e} E_0}{m_\mathrm{e}\omega_\mathrm{c}} t \sin(\phi). \tag{2.50}$$

The first term of Eq.2.50 describes the quivering motion of the electron due to the oscillating force. The quiver amplitude is given by

$$x_\mathrm{quiv} = \frac{q_\mathrm{e} E_0}{m_\mathrm{e}\omega_\mathrm{c}^2}. \tag{2.51}$$

The second term corresponds to a drift motion that is introduced depending on the laser phase at time $t = 0$, e.g. at the instant of ionization. Because of that, the electron will usually revisit the origin only a few times or maybe not at all. This phenomenon is observed in strong-field physics where the electron might or might not recombine with the ion (HHG) or rescatter off the ion (above-threshold ionization). Equation 2.49 also contains the quivering (first term in brackets) and drift (second term in brackets) motion. The mean kinetic energy contained in the quivering part of the electron motion is obtained via averaging over one optical cycle. This quantity is called the ponderomotive potential:

$$U_\mathrm{P} = \langle E_\mathrm{quiv} \rangle = \frac{m_\mathrm{e}}{2} \langle \left[\frac{q_\mathrm{e} E_0}{m_\mathrm{e} \omega_\mathrm{c}} \sin(\omega_\mathrm{c} t + \phi) \right]^2 \rangle = \frac{q_\mathrm{e}^2}{4 m_\mathrm{e}} \frac{E_0^2}{\omega_\mathrm{c}^2} = \frac{q_\mathrm{e}^2}{2 c \varepsilon_0 m_\mathrm{e}} \lambda_\mathrm{c}^2 I \tag{2.52}$$

U_P acts as an additional potential on top of, for instance, the ionization potential. For an electron that is liberated from an atom in the presence of a strong laser field, not only the energy to overcome the binding energy I_P has to be supplied by the laser field but also the energy for the unavoidable quivering motion. Therefore the ionization potential is effectively increased:

$$I_\mathrm{P}' = I_\mathrm{P} + U_\mathrm{P}, \tag{2.53}$$

which has even been measured time-dependently for an ultrashort dressing laser field [79]. Substituting the physical constant symbols of Eq. 2.52 by their values yields a ponderomotive potential of 9.32 eV per $\mu\mathrm{m}^2$ and $\mathrm{TW/cm}^2$. In many strong-field phenomena, the ponderomotive potential is the crucial parameter that determines the on-going processes rather than the laser intensity. One prominent example is the well-known cut-off law in HHG (see Eqs. 2.17 and 2.18 in Sec. 2.1):

$$\hbar \omega_\text{cut-off} = I_\mathrm{P} + 3.17 U_\mathrm{P}. \tag{2.54}$$

The wavelength dependence of U_P makes mid-infrared lasers in the few-µm regime very attractive for HHG as they allow for much higher cut-off energies compared to traditional Ti:sa lasers at around 780 nm. In contrast, for an X-ray free electron laser, like the *linac coherent light source* (LCLS), the wavelength is around 5 to 0.5 nm, which reduces the ponderomotive potential by factor of 10^4 to 10^6. Hence, although the peak intensities of these different light sources can be similar, the physics arising from the interaction with matter might be quite different. Keldysh introduced the γ parameter (named after him the Keldysh parameter)

$$\gamma = \sqrt{\frac{I_\mathrm{P}}{2 U_\mathrm{P}}}, \tag{2.55}$$

which helps to distinguish between two regimes of strong-field physics: the tunneling regime (see Sec. 2.1.3) for $\gamma \ll 1$ and the multiphoton regime for $\gamma \gg 1$. In the tunneling regime, the laser period is typically long compared to the electronic time scale, so that the laser field appears quasi-static and bends the atomic potential slowly allowing for tunneling of an electron. By contrast, in the multiphoton regime, the laser oscillation is fast compared to the electronic time scale. Strong-field ionization is treated as the absorption of many laser photons rather than tunneling of the electron. As an example, in the case of Ar ($I_\mathrm{P} = 15.8$ eV) exposed to a Ti:sa laser pulse of 780 nm and 1×10^{14} $\mathrm{W/cm}^2$ the Keldysh parameter amounts to $\gamma = 1.18$, which is just in between the two regimes.

Nevertheless, this situation is usually treated with the ADK formula (Eq. 2.16), which yields reasonable results even though it is a true tunneling theory.
In Chap. 6 the effect of the ponderomotive potential of an ultrashort strong-field laser pulse on highly excited states is used in order to characterize the duration and intensity of the pulse.

2.6 The helium atom

The helium atom consisting of a nucleus and two electrons is the simplest system one can think of that exhibits electronic correlation. However, Coulomb interaction among the electrons make its theoretical description hard so that, similar to the classical three-body problem of celestial mechanics, a closed-form analytical solution could not be presented to date and numerical solutions are computationally very expensive. That is one of the reasons why helium is still a very interesting object to study in atomic physics: the atomic structure is simple compared to heavier atoms, nevertheless, electronic correlations are present in contrast to atomic hydrogen giving rise to complex physics. The electronic energy levels of helium that can be reached via single photon absorption span a broad range from 21.22 eV above the $1s^2$ ground state for the 1s2p first excited state – up to 78.98 eV for the threshold of complete ionization of the atom. The first ionization threshold, i.e. the energy for removing one electron while the second electron remains in the ground state, is 24.59 eV—the highest of all atoms. Between 24.59 eV and 78.98 eV lies an energy range of states were both electrons are in not in the 1s shell. These *doubly excited* states are unstable and ionize spontaneously. Section 2.6.1 is devoted to their physics and characteristic spectral response, which are both determined by electron–electron interaction.

Table 2.2 summarizes the energy levels and decay rates of a series of dipole-allowed singly and doubly excited states. There is a variety of further states, but these are either dipole forbidden or have a (much) lower cross-section than the states listed above. In this thesis the doubly excited manifold shown in the table is of particular interest. Chapters 5 and 6 both present measurements focusing on these states. Therefore, more details about these states are discussed in the following section.

2.6.1 Autoionization and Fano lines

The singly excited states of helium exhibit a Lorentzian line shape, which is commonly observed in absorption spectroscopy of many atoms. By contrast, the doubly excited states show a very different absorption behavior. If measured at sufficient resolution, e.g. as in Ref. [82], the line shape, a so-called Fano profile, turns out to be asymmetric. Fano was the first to develop a theory that could explain the physics behind this kind of line shape [84]. In simple words, the explanation of the asymmetric line shape is the following: Since the doubly excited states are located above the first ionization threshold, there are two possible quantum pathways that lead to the same final state. (1) Excitation of a doubly excited state by XUV light and subsequent autoionization due to Coulomb repulsion of the two electrons, which leads to a free electron and a remaining electron in the 1s shell.

Configuration	Energy (eV)	Decay rate (meV)
singly excited states		
$1s^2$	0	
1s2p	21.22	0.0074
1s3p	23.09	0.0023
1s4p	23.74	0.0010
1s5p	24.05	0.0005
1s6p	24.21	0.0003
1s7p	24.31	0.0002
doubly excited states		
2s2p	60.15	37.4
$2p^2$	62.06	6 (dipole-forbidden)
sp_{23+}	63.66	8.2
sp_{24+}	64.47	3.5
sp_{25+}	64.82	1.8
sp_{26+}	65.00	1.0
sp_{27+}	65.11	0.7

Table 2.2: *Energies and decay rates of a selection of singly and doubly excited states in helium that are dipole-allowed with respect to the ground state. The notation sp_{2n+} refers to a linear combination of 2snp+2pns. Data from [80–83]*

(2) Direct ionization of one ground state electron by an XUV photon, while leaving the second electron in the 1s shell. Both final states are indistinguishable, which gives rise to interference. As the phases of both pathways are not identical, the interference is not completely constructive. If it was completely constructive, the absorption line would be Lorentzian. Fano's original theory is based on treating a discrete state (the doubly excited state) that resides within a continuum of states (the direct ionization continuum). If there is an interaction among these states (Coulomb interaction), the new Eigenstates are a mixture of the discrete state and the continuum states, with the transition cross-section following the Fano profile. Based on this theory, the line shape is parametrized by the so-called Fano q-parameter:

$$\sigma \propto \frac{|q+\varepsilon|^2}{1+\varepsilon^2} \qquad \varepsilon = \frac{\omega-\omega_\mathrm{r}}{\Gamma/2} \tag{2.56}$$

The q parameter is the ratio of the different coupling strengths

$$q = \frac{\mathrm{GD}}{\pi\,\mathrm{GC}\times\mathrm{DC}} \tag{2.57}$$

where GD is the coupling matrix element between the ground state (G) and the discrete state (D), GC is the matrix element between ground state and the continuum states (C), and DC is the so-called configuration interaction, i.e. the coupling between the discrete state and the continuum (here, Coulomb interaction of the two electrons). The line shape for different values of the q-parameters is shown in Fig. 2.7. The case of $q \gg 1$ gives rise to the Lorentzian line shape since effectively the direct ionization pathway is suppressed.

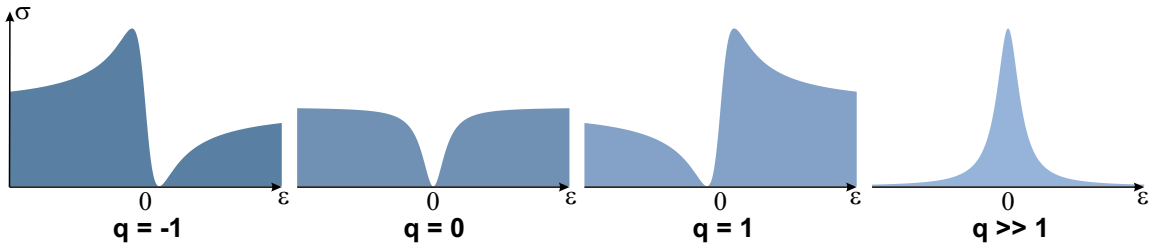

Fig. 2.7: *Absorption line shape for different values of the Fano q-parameter. The resonance position and width are identical because of the use of ε.*

For $q = 0$ a so-called window resonance arises: the absorption cross-section on resonance is minimized. For other values of q the line is asymmetric as it is the case for the doubly excited states of Tab. 2.2. A comprehensive derivation of the physics behind the Fano profiles can also be found in Ref. [85].

In the experiment, there is usually a relatively flat background caused by other continuum transitions that do not interfere with the discrete state.

These considerations suggest that the helium atom can be considered a quantum interferometer. Just like its optical counter part, the Michelson interferometer, it consists of two arms: a fixed arm, which is the fast and non-resonant direct ionization channel, and a second tunable arm, which is the doubly excited state that autoionizes after a certain lifetime. This finite lifetime allows for the manipulation of the arm: By dressing the atom with a strong laser field the phase acquired on the second interferometer arm can be controlled, which manifests itself in the absorption line shape [26]. A detailed description of this kind of line shape modification is given in Chap. 4.

Chapter 3

Experimental setup

In this chapter, the concept of attosecond transient absorption spectroscopy and its experimental realization in the frame of this work shall be discussed. While the general principles of femto- and attosecond pulse generation were presented in Sec. 2.1, technical and experimental details are provided here. In addition to transient absorption spectroscopy, the photoelectron based method of attosecond streaking is currently implemented in the experimental setup, and is discussed in this chapter. Finally, a brief overview on how the recorded spectra are processed is given. Further details regarding the attosecond beamline can be found in [86–88].

3.1 Transient absorption spectroscopy

The principle of traditional absorption spectroscopy is simple. An experimental setup consists of three ingredients:

1. The light source, e.g. a Xe arc lamp, a laser, or a synchrotron radiation source.
2. The spectroscopy target, e.g. a gas of atoms or molecules or a solid.
3. The spectrometer, which consists of
   (a) the monochromator, e.g. a grating or a prism
   (b) the detector, e.g. a charge coupled device (CCD) camera or a photographic film

The light emitted from the light source is sent through the spectroscopy target, and the transmitted light is spectrally resolved and recorded. By comparing this spectrum to a reference spectrum, i.e. the spectrum without the target, the spectroscopic fingerprint of the target medium can be obtained. Depending on the photon-energy regime, different properties of the target can be accessed, e.g. rotational (μeV), vibrational (meV), or electronic (eV) properties. As the electronic properties of the target are the main research subject in this thesis, the focus is put on these in the following. The typical stationary absorption spectrum already contains a lot of information about the target's electronic

structure. The position of the absorption lines reveals the level spacing of the accessible states whereas the natural line width, i.e. disregarding spectrometer resolution and broadening mechanisms, is determined by the lifetime of the states. Furthermore, the exact line shape, as was shown in Sec. 2.6, encodes information about the environment of the state. However, traditional absorption spectroscopy is very limited with regard to accessing dynamics of the electron system. Thus, a time-resolved version of absorption spectroscopy was developed: the so-called transient absorption spectroscopy (TAS). As many other time-resolved methods, TAS is in principle a pump–probe scheme applied to stationary absorption spectroscopy. A pump pulse, which is often but not always rather strong compared to the probe pulse, is sent through the spectroscopy target in order to trigger some dynamics—or in other words—to bring the system into a non-equilibrium state. After a certain time delay τ, the probe pulse is sent through the medium in order to probe the effect of the pump pulse on the system by recording the probe pulse absorption spectrum. By varying the time delay between pump and probe, the evolution of the dynamics is resolved in time. In general, pump and probe pulse can have completely different photon energy, which is often called two-color configuration. In order to access the electronic dynamics in highly excited states, the photon energy of the probe must be in the XUV to soft-x-ray regime [38, 89]. Furthermore, since the goal is to resolve electron dynamics on their natural time scale, the pulse duration needs to be in the attosecond regime. This leads to the technique of *attosecond transient absorption spectroscopy* (ATAS). As the achievable intensity in the attosecond XUV regime is not sufficient to perform an attosecond pump and probe step, up to now, the second pulse in ATAS is always a femtosecond pulse (typically in the NIR). Compared with the competing techniques, such as photoelectron-spectroscopy-based methods (e.g. the attosecond streak camera [90–92], the reaction microscope also referred to as cold target recoil ion momentum spectrocopy (COLTRIMS) [93–96], and angular streaking [36, 37, 97]) and high-harmonic spectroscopy [32, 98, 99], ATAS provides certain advantages. First of all, ATAS intrinsically gives access to bound–bound transitions, whereas in photoelectron or photoion methods an electron has to be liberated from the system eventually in order to detect a signal. From the experimental point of view, ATAS is an all-optical technique. This means that instead of a rather complicated electron spectrometer where for example space-charge effects, static electric and magnetic fields, and more rigorous vacuum conditions have to be considered, an optical spectrometer is sufficient. Last but not least, ATAS allows the target to be studied in both weak and strong-field regimes. Thus, the target may be investigated in a close-to-natural environment with weak–laser-induced perturbations up to the case of highly nonlinear interactions at laser intensities exceeding 10^{13} W/cm^2. These properties make ATAS a very attractive complement to the other methods.

In the first ATAS experiments, a strong NIR pulse was used as the pump step, e.g. leading to strong-field ionization of krypton atoms [40]. The time-delayed attosecond XUV pulse was considered the probe, which in the example of strong-field–ionized krypton was used to probe for the ionic states. However, there is a second scheme of performing ATAS experiments or a second way of interpretation. In this scheme, the XUV rather than the NIR pulse is considered the pump, as it promotes the target electrons to highly excited states. This excitation gives rise to the dipole response, as discussed in Sec. 2.4. During the finite lifetime of the dipole response the femtosecond NIR pulse is sent in and interacts with the system. As described in detail in Chap. 4, this interaction leaves its fingerprint

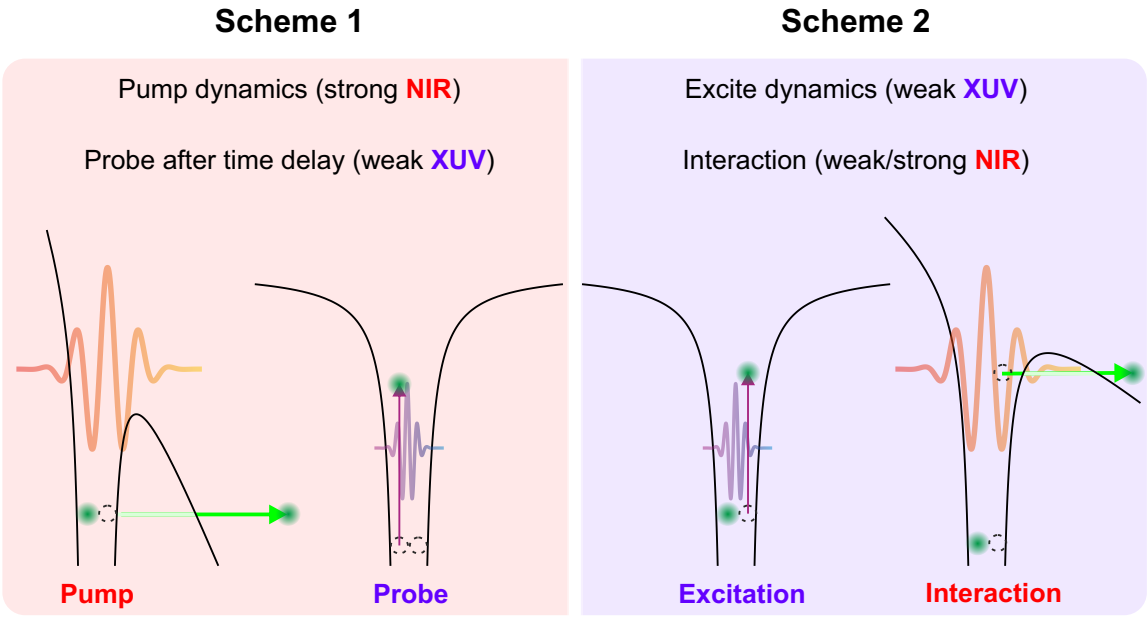

Fig. 3.1: *Comparison of the two common schemes of attosecond transient absorption spectroscopy. A typical scenerio for scheme 1 is strong-field ionization of atoms with an intense NIR pulse as the pump step. Followed by a weak XUV pulse to probe the ionic states and dynamics induced by the pump. A similar scenario in the sense of scheme 2 involves the weak XUV pulse to promote electrons to excited states, which is followed by an NIR pulse interacting with the excited system. For a strong NIR pulse this would give rise to strong-field inonization of the excited states as shown above. A weaker NIR pulse could lead to a perturbative coupling of states for example. The effect of the NIR pulse is manifested in the dipole response, and thus, in the XUV absorption spectrum.*

in the dipole response. The coherent superposition of the dipole response and the XUV pulse form the transmitted spectrum, which can be considered the probe of the dynamics. This is the reason why the NIR can influence the XUV spectrum, although the NIR pulse arrives at the target after the XUV pulse is already gone. In that sense, the XUV pulse can be regarded as both pump (excitation of electrons) and probe (formation of the transmitted spectrum), while the NIR pulse acts in between. Because of that, instead of using the phrases pump and probe the two pulses are referred to as excitation (XUV pulse) and interaction (NIR pulse). Figure 3.1 shows a comparison of the two schemes. In this theses, by referring to ATAS the second scheme is meant, which is also known as perturbed polarization decay [100].
In the following sections, the experimental apparatus to perform the ATAS experiments shown in this work is described.

3.2 Femtosecond laser system

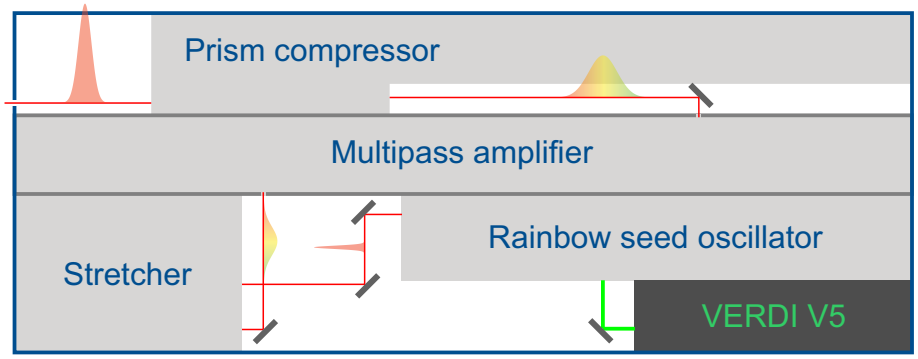

Fig. 3.2: *Schematic drawing of laser system Femtopower Compact Pro CEP by Femtolasers GmbH operating according to the CPA prinicple. The oscillator pulses are stretched by passing them through thick glass blocks in the stretcher. Third-order dispersion (TOD) accumulated in the stretcher is compensated by TOD mirrors. Afterwards, the pulses are amplified by going 9 times through the amplifier gain medium, which is also a Ti:sapphire crystal. Finally, the amplified pulses are recompressed to* < 30 *fs in the prism compressor.*

The basics of amplified femtosecond laser systems are described in the introductory chapter (see Sec. 2.1.2). The laser system used for the experiments presented in this thesis is a commercial Ti:sapphire system from the company Femtolasers (meanwhile Spectra Physics), which is illustrated in Fig. 3.2. The Femtopower Compact Pro CEP houses the oscillator (model: Rainbow seed CEP3) including the pump laser (Verdi V5, Coherent), the multipass (9 passes) CPA stage, and the prism compressor. The Q-switched kHz pump laser (DM-30, Photonics industries) for the amplifier is installed next to the Femtopower and provides the typically used pump powers of 30 W. The laser systems delivers sub-30 fs pulses with about 0.7 mJ pulse energy at a repetition rate of 4 kHz. The unamplified pulses of the Rainbow seed oscillator are generated at 78 MHz with sub-10 fs duration and 2 nJ pulse energy. The central wavelength is 790 nm. As an additional feature, the laser pulses can in principle be CEP stabilized, which however was not made use of in the results presented here (partly because the CEP infrastructure had to be removed due to technical issues). The beam pointing of the output is stabilized to reduce fluctuation in the following section of the setup.
The laser output is then spectrally broadened by focusing the beam into a neon-filled hollow-core fiber (Fig. 3.3 (a)). Typically a neon pressure between 1.5 and 2.5 bar is used. The fiber has a length of about 100 cm, a core diameter of 250 µm and is located in a commercial housing (Kaleidoscope, Femtolasers). As shown in the figure, a glowing plasma jet is generated before the fiber entrance. Since plasma introduces pulse and beam distortions the amount of plasma should be kept low. Also nonlinear effetcs in the entrance and exit window require the beam diameter on the windows to be as large as possible. After spectral broadening the linearly acquired and SPM-induced chirp is compensated for by a chirped-mirror compressor (PC70, Ultrafast Innovations), which is designed to reduce the chirp of a typical hollow-core fiber compressor between 500 and 1000 nm. The fiber and chirped-mirror compressor output is characterized by means of a spectrometer (HR4000+ 200 - 1100 nm, Ocean Optics) and a second-order interferometric autocorre-

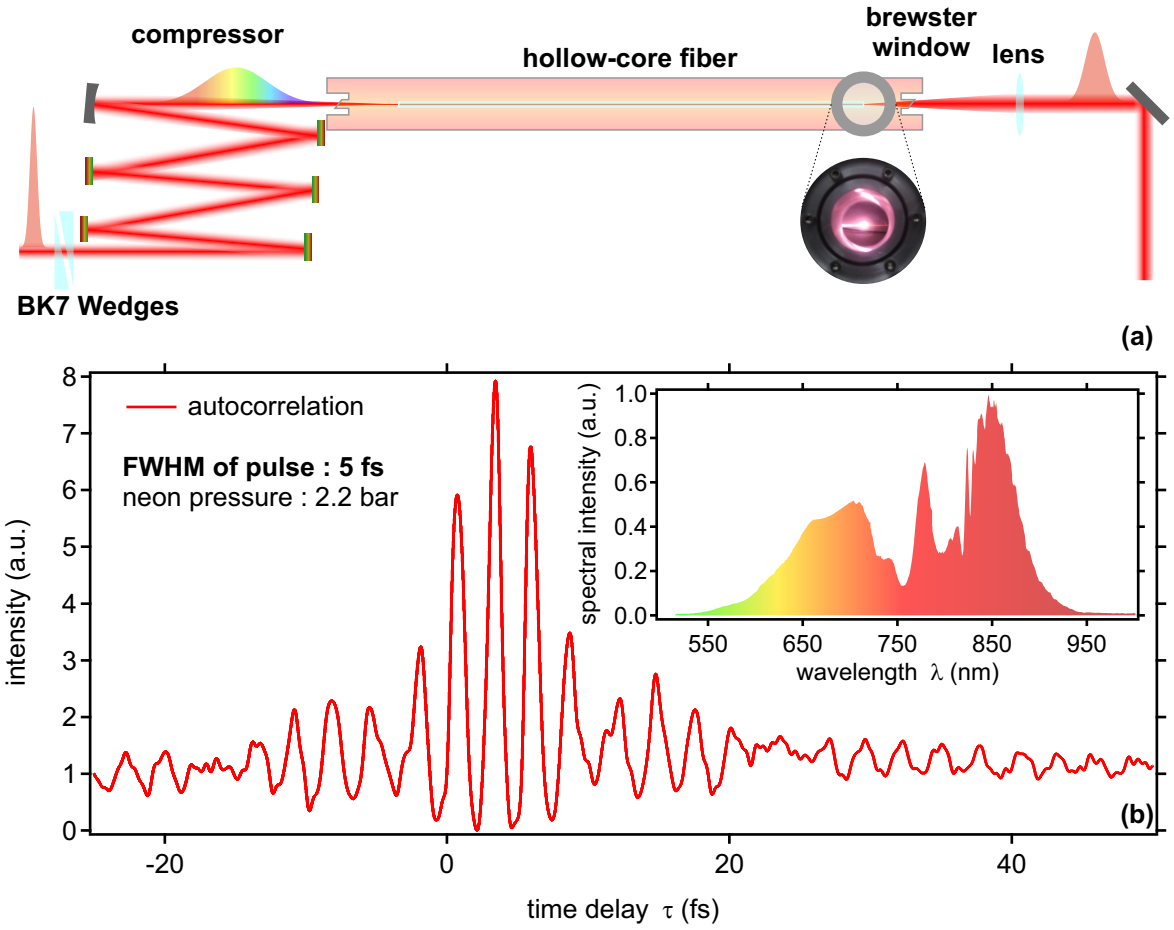

Fig. 3.3: *(a) Principle of pulse compression via hollow-core fiber and chirped mirrors. The input pulse is focused ($f = 1$ m) into a hollow-core glass fiber filled with neon. SPM leads to broadening of the spectrum and introduces a chirp to the pulse, which is compensated for by a chirped mirror compressor. Fine tuning of the dispersion is achieved with a pair of wedges. (b) Typical autocorrelation and spectrum after hollow-core fiber and chirped-mirror compressor. The spectrum ranges from 550 - 950 nm, thus spanning almost a whole octave. The pulse duration obtained from the interferometric autocorrelation is about 5 fs. The two side maxima indicate the presence of a weak post pulse.*

lator (Femtometer, Femtolasers). A typical spectrum and autocorrelation are shown in Fig 3.3 (b). The pulse duration retrieved from the autocorrelation is about 5 fs FWHM, which can be regarded as a rough estimate of the true pulse duration. The pulse energy at this point is reduced by almost 50 % to about 350 µJ due to losses in the hollow-core fiber and chirped-mirror compressor. Unfortunately, the blue part of the spectrum is not reflected by the chirped mirrors, although it is the most important part for achieving the shortest pulses. Therefore, a new mirror compressor (Mosaic OS, Femtolasers) with mirrors covering a range of 450 - 950 nm is planned to be used in the near future.

For pulses in the few-cycle regime, autocorrelation is not an ideal tool for pulse characterization especially because the presence of a chirp can lead to false interpretation of the autocorrelation signal. Thus, a dispersion-scan (d-scan) setup [101] was implemented recently, which allows for a complete reconstruction of the laser pulses (except for the CEP) similar to the well established techniques of spectral interferometry for direct electric field

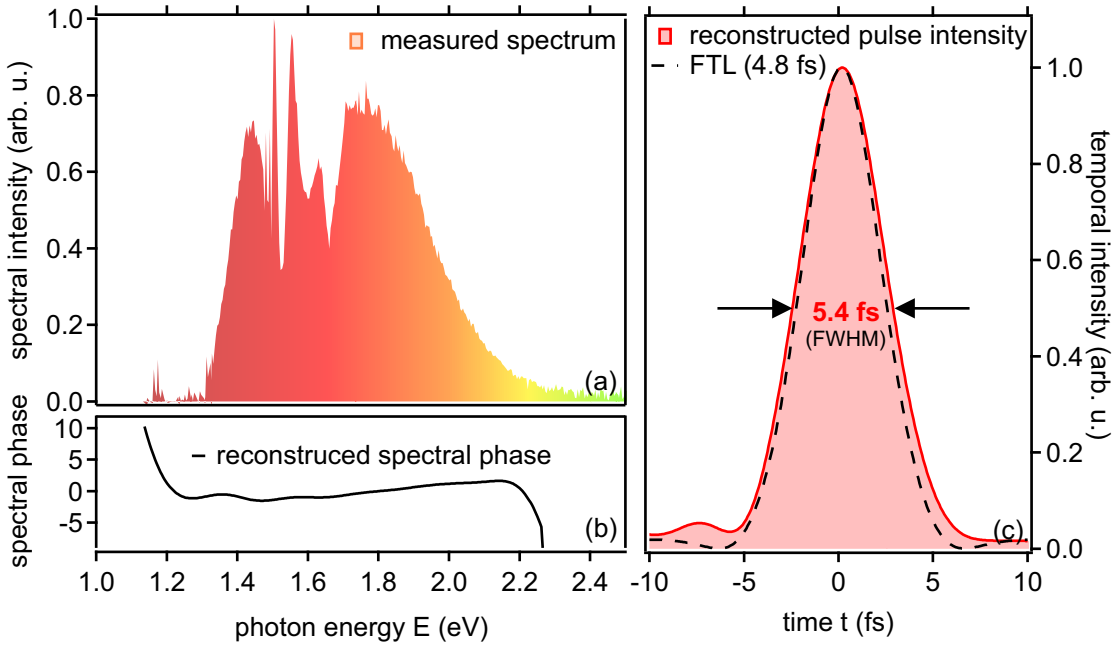

Fig. 3.4: *(a) Input spectrum (amplitude) of the laser after spectral broadening in the hollow-core fiber and compression in the chirped-mirror compressor. (b) Extracted spectral phase as the main result of the d-scan measurement and evaluation. (c) Reconstructed laser pulse (red) given by the Fourier transform of the spectrum (amplitude and phase) compared to the transform limited pulse (black).*

reconstruction (SPIDER) [102] and frequency-resolved optical gating (FROG) [103]. In the d-scan method, the second harmonic generation (SHG) spectrum of the laser that is to be characterized is recorded as a function of the amount of glass the laser pulses pass through. The amount of glass, and thus the dispersion added to the incoming pulse, is precisely controlled via a motorized pair of wedges. By knowing the input spectrum of the laser and the dispersion characteristic of the glass wedges (n-BK7), an algorithm tries to extract the spectral phase of the laser pulse by fitting a calculated SHG spectrum to the measured spectrum. The result of such a d-scan measurement is depicted in Fig. 3.4. The reconstructed pulse of 5.4 fs FWHM duration demonstrates the successful generation of few-cycle pulses by the hollow-core fiber compressor setup. The deviation from the Fourier limited pulse of 4.8 fs FWHM duration is only 0.6 fs indicating an almost flat spectral phase. Note that the autocorrelation measurement and d-scan measurement are not directly comparable as they were recorded under slightly different conditions.
Further pulse characterization is done in the experimental vacuum chamber by means of an *in situ* technique in transient absorption spectroscopy conceived and developed in this thesis work(see Chap. 6) as well as a currently developed attosecond streak camera (see Sec. 3.3.1).
These laser pulses can now be focused to reach intensities in the order of 10^{14} to 10^{15} W/cm^2, which is necessary in order to drive high-harmonic generation.

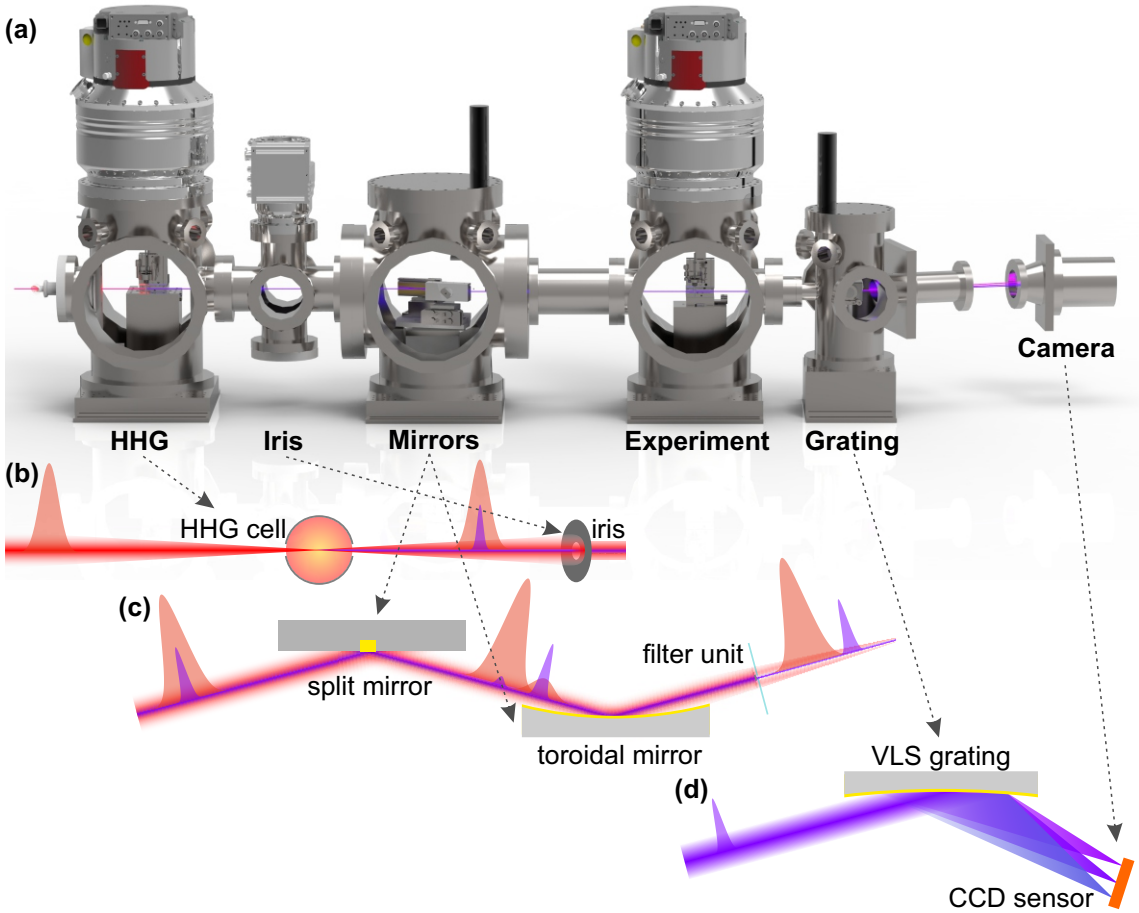

Fig. 3.5: *(a) Complete beamline with NIR and XUV beam path drawn. The harmonic generation chamber is followed by the iris chamber and the mirror chamber, which also houses the filter unit. After the temporal separation of the pulses, the experimental chamber with the target gas cell and the second filter, as well as the spectrometer consisting of the grating and the camera follow. (b), (c), and (d) show details of the two beams and pulses passing the optical elements in the different chambers.*

3.3 Attosecond spectroscopy beamline

After the Ti:sapphire pulses are spectrally broadened and compressed, they are used to drive HHG (see Sec. 2.1.3) in order to produce attosecond pulses of XUV light, and in the second step, they are combined with the generated XUV beam to perform the transient absorption experiment.

XUV light is strongly absorbed in the atmosphere as the photon energy easily exceeds the ionization potential of all gases. Therefore, the beam has to be generated and guided in a system of vacuum chambers—the beamline—shown in Fig. 3.5 (a). A Brewster-angled window marks the entrance of the chamber setup. The laser is focused by a spherical mirror ($f = 50\,\text{cm}$) into a gas cell, typically filled with neon or argon at 10 - 100 mbar backing pressure (Fig. 3.5 (b)). The gas cell has an inner diameter of 2 mm with two drilled holes allowing the laser beam to enter the cell. Taking into account

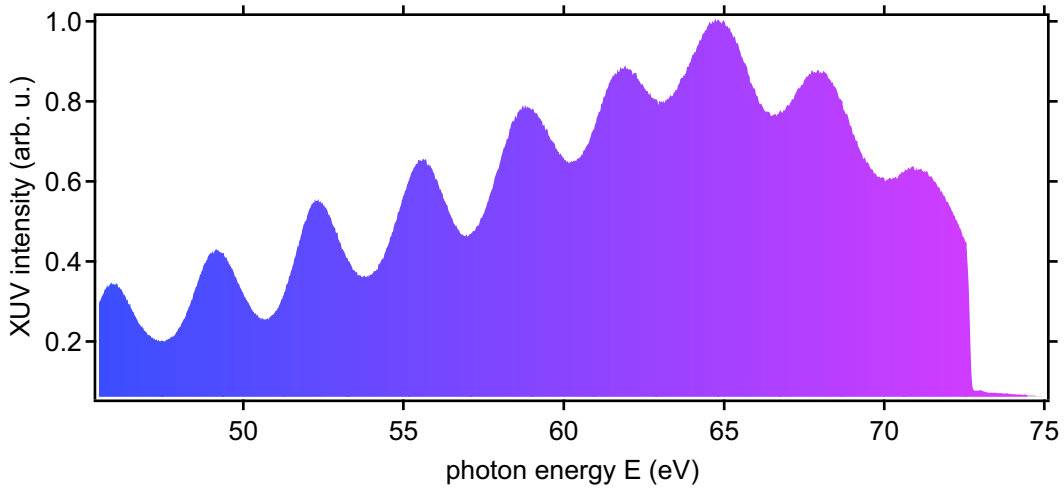

Fig. 3.6: *High harmonic spectrum generated in neon in the energy region between 45 and 75 eV used for the experiments in this work. The sharp cutoff near 72.3 eV is cause by the Al filters used to remove the copropagating NIR light.*

the gas jet emerging from the holes, the effective generation-medium length is about 3 mm. To account for the high gas load, a 2300 l/s turbo molecular pump (HiPace 2300, Pfeiffer Vacuum) is installed reducing the pressure in the chamber to 10^{-4} to 10^{-3} mbar. Typically photon energies between 20 and 100 eV are emitted in the form of a train of a few attosecond pulses. By spectroscopically selecting the high-energy part of the spectrum, attosecond pulses originating from weaker half-cycles of the driving pulse are discarded. A typical harmonic spectrum generated in neon is shown in Fig. 3.6. The relatively continuous intensity distribution around 65 eV indicates the presence of only one major and a few minor attosecond pulses in that energy region (a flat spectrum is only a real evidence for the generation of an IAP if the CEP is stabilized). The duration of each attosecond burst is unknown because up to now the attosecond pulse duration is not accessible by means of transient absorption spectroscopy. The attosecond streak camera that is currently under construction (see next section) will be able to deliver both the XUV as well as the NIR pulse durations. The sharp drop in intensity is caused by the absorption edge of aluminum filters (described below) around 72.3 eV. After the harmonic generation, a motorized iris aperture is placed in order to control the intensity of the NIR, which is one of the major degrees of freedom. In contrast to the NIR beam, the much narrower XUV beam is barely affected by the iris position. Only if the zero-aperture iris is close to shut, the XUV beam intensity is reduced.

Next, the two co-propagating beams are reflected off of a split mirror under grazing incidence in order to introduce a time delay between the corresponding pulses (Fig. 3.5 (c)). The narrow XUV beam almost exclusively hits the gold-coated inner part of the mirror, whereas most of the strongly diverging NIR beam hits the silver-coated outer mirror. A piezo is used to move the inner mirror with respect to the outer mirror with sub-µm precision. Typically a step size of 171.15 as is used for scanning one pulse across the other in the pump–probe scheme. The interferometric stability of the split mirror setup is on the order of 10 as. In order to completely separate the XUV pulse from the NIR pulse, the part of the NIR hitting the inner mirror and the part of the XUV hitting the outer mirror have to be removed. This is accomplished by a filter unit that consists

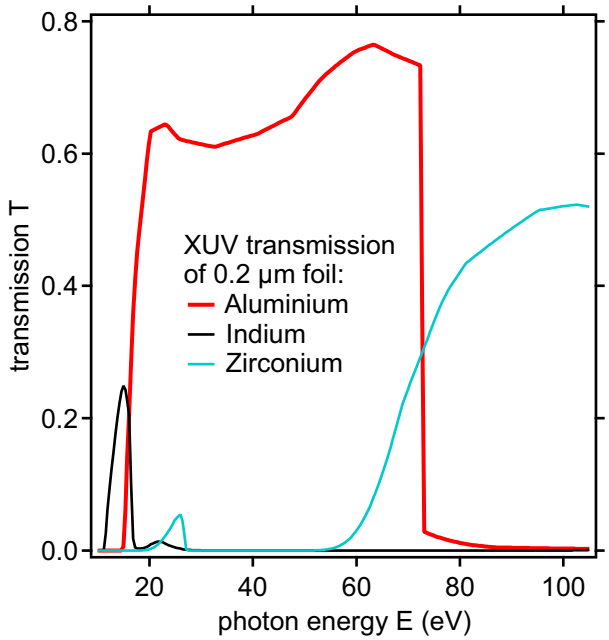

Fig. 3.7: *XUV transmission for the different filter materials of the 0.2 µm thin metal foil filters used in the experiments. Aluminum (red) shows a broad transmission window between 16 and 73 eV making it suitable for many experiments with innervalence- or doubly-excited noble gases. The rather narrow transmission window of Indium (black) starts already around 11 eV, which allows for spectroscopy of molecules and less strongly bound states of atoms. Zirconium (blue) exhibits a broad transmission region above 60 eV allowing for the spectroscopy of highly excited states, e.g. around the double ionization threshold of helium. Data taken from [104].*

of a 2 µm thin polymer membrane with a center hole, and a metal foil filter covering this hole. The XUV beam is transmitted by the metal filter (200 nm thin aluminum for all data presented, replacable by, e.g., indium or zirkonium filters for different spectral regions, see Fig. 3.7) and can only pass the hole in the polymer membrane because it is strongly absorbed (optical density of 5 for XUV light) by the membrane material (nitrocellulose). On the other hand, the NIR passes the whole membrane except for the hole because it is reflected by the metal filter in front. By that, a complete spatial and thus temporal separation of the pulses can in principle be achieved. However, due to micro holes and cracks in the metal foil and incomplete coverage of the hole, a small amount of NIR light leaks through the center part of the filter unit leading to a weak additional NIR pulse on top of the XUV pulse. This leakage pulse leads to a population of otherwise dipole forbidden states (e.g. states of S and D symmetry in the case of He) in the initial population step by means of two-photon interaction (XUV + NIR or XUV - NIR). Although this effect is unwanted in many situations and thus minimized, it can be exploited in the sense of a four-wave-mixing scheme as recently shown [9].

Placed between the split mirror and the filter unit, a gold-coated toroidal mirror (Hellma Optics) images the generation volume into the experimental gas cell, where the actual pump–probe experiment takes place. To increase reflectivity, the mirror is hit under 15° grazing incidence, which is the reason for the toroidal shape: a spherical mirror would introduce strong astigmatism under these conditions as the beam experiences two different effective radii of curvature for the meridional and sagittal plane. For a torus, the two different radii of curvature just compensate for astigmatism, which leads to better image quality and higher peak intensity. Note that spherical aberration is still present, as the torus has a circular curvature. However, the 1:1 imaging property and the small size of at least the XUV beam help to minimize aberrations.
The chamber housing the experimental cell is pumped by another 2300 l/s turbo pump since the gas load during an experiment is comparable to that in the generation chamber

in order to increase the optical density of the target for adequate signal-to-noise ratio. The NIR intensity in the experimental cell can reach up to about 10^{13} W/cm^2, which is enough to study strong-field effects. After the experimental cell, the NIR beam is dumped by means of another metal filter (also aluminum here) as it would cause damage to the sensor of the XUV camera. This filter is followed by a gold-coated variable line space (VLS) grating (avg. 1200 groves / mm, Hitachi) hit under grazing incidence (Fig. 3.5 (d)). The surface of the grating is cylindrically shaped with focusing propeties in the dispersive plane and no curvature in the perpendicular direction. Therefore, the XUV beam profile is unaffected in the vertical direction, which allows to control the beam quality. By contrast, in the horizontal plane, identical spectral components hitting the grating across the extended beam profile are focused in single line. Using a VLS grating, the foci of each wavelength are situated along a flat plane rather than on a curved surface (the Rowland circle) as it would be the case for an ordinary cylindrical grating. This is because the variable line spacing itself introduces a focusing property: Depending on the position on the grating the diffraction angle varies across the beam profile due to the varying line spacing. Hence, the diffracted rays emerging from different positions on the grating can meet at some point in space. The grove spacing can be designed in such a way that it flattens the image plane of the concave grating surface. The photon energy range of the grating is 20 - 110 eV, which is dispersed and focused (in the dispersive plane) along the 110 mm long image line. Thus, the 27 mm large camera sensor (1340 pixels) covers a considerable region of the spectral bandwidth. In order, to record the full spectral range the camera is moved along the gratings' image plane by means of a home-built camera suspension. The CCD chip is back-illuminated and thermoelectrically cooled to -50 °C, which allows for low noise and short integration times (typically 100 ms - a few seconds). The resolution of the spectrometer is about 20 meV (standard deviation) at 60 eV photon energy.

3.3.1 Photoelectron streak camera

In order to extend the scope of the beamline beyond transient absorption measurements towards photoelectron experiments, and to establish a powerful femto- and attosecond pulse characterization method, an attosecond streak camera [90–92] is currently build up. The principle of the attosecond streak camera shown in Fig. 3.8 (a) is the following: The (isolated) attosecond pulse triggers single-photon ionization in the target gas. The low frequency NIR pulse acts as the streaking field, which is super-imposed and scanned over the XUV pulse by varying the time delay. Since the attosecond pulse is much shorter than the optical cycle of the NIR, the beginning of the NIR-electron interaction is well confined in time. The liberated electrons will acquire a certain momentum change Δp, which is determined by the NIR's vector potential A at the time of photo ionization:

$$\Delta p = q_\mathrm{e} \int_{t_0}^{\infty} E(t)\mathrm{d}t = q_\mathrm{e} A(t_0) \tag{3.1}$$

Thereby, the vector potential, and with that also the electric field, of the NIR pulse is directly mapped to the momentum shift of the photoelectrons, which can be measured via an electron time-of-flight (TOF) spectrometer. Hence, the streaking technique allows for the direct measurement of the oscillating electric field—the wave form—of the pulse. This

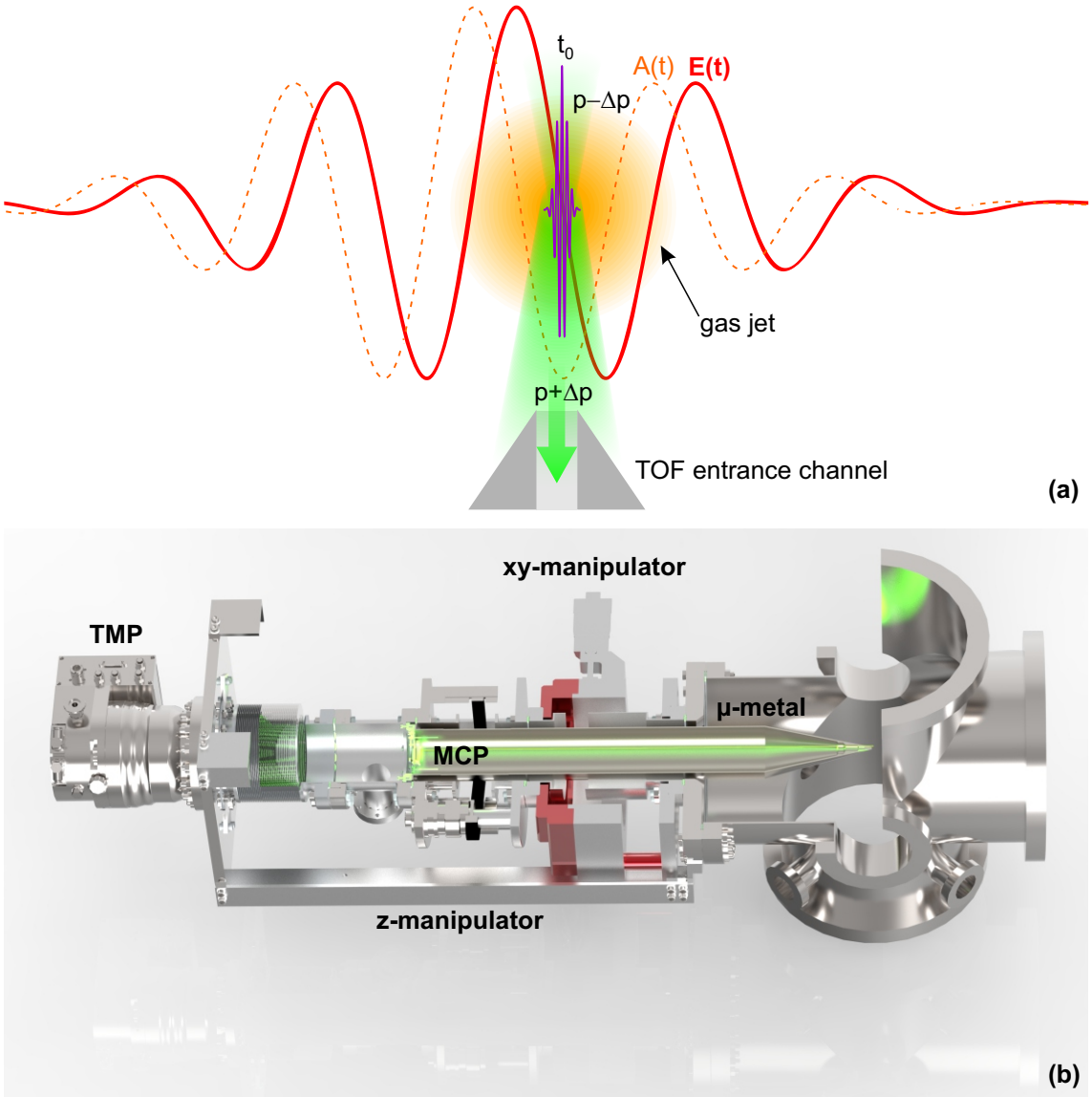

Fig. 3.8: *(a) Principle of attosecond streaking. The attosecond XUV pulse (purple) photoionizes the target gas at time t_0 and the free photoelectrons are dressed by the NIR pulse (electric field red, vector potential orange dashed). Thus, the final electron momentum is shifted by $\Delta p = q_e A(t_0)$ depending on the delay between XUV and NIR. This momentum shift can be measured by means of an electron time-of-flight spectrometer (TOF). (b) Drawing of movable photoelectron streak camera with key components named. The path of the photoelectrons is indicated by the green trace inside the μ-metal shield.*

makes the streak camera an analog of the oscilloscope in the petahertz domain. Furthermore, using the numerical frequency- resolved optical gating for complete reconstruction of attosecond bursts (FROG CRAB) algorithm it is possible to reconstruct the attosecond pulse [105]. Alternatively, the reconstruction of attosecond beating by interference of two- photon transitions (RABBITT) technique can be used to reconstruct attosecond pulse trains [106]. Besides the possibilities of femto- and attosecond pulse reconstruction, the streak camera allows to investigate fundametal aspects of quantum dynamics such as time delays in photoemission [25].
The heart of the streak camera is the TOF spectrometer, which mainly consists of a magnetic-field–free drift tube made from μ-metal and the microchannel plate detector (MCP) as shown in Fig. 3.8. The drift tube has a tip with a 1 mm diameter entrance channel, which can be moved close to the experimental cell along all axes in order to collect electrons emerging from a gas jet. The small entrance channel acts both as a momentum filter for the photoelectrons, since only those electrons leaving the target along the NIR-laser polarization are of interest, as well as a differential pumping stage. Differential pumping of the TOF volume is necessary in order to assure safe operation of the MCP detector and to maximize the mean free path of the photoelectrons. Together with a 300 l/s TMP (HiPace 300, Pfeiffer) at the back of the TOF apparatus, pressure of up to 10^{-3} mbar in the experimental chamber is expected to be reduced to 10^{-6} mbar in the TOF. For 10^{-3} mbar, the mean free path is ≤ 10 cm, (according to [107] where a mean free path of 67 nm in the atmosphere was reported) whereas for 10^{-6} mbar the mean free path easily exceeds the dimensions of the vacuum chamber allowing for unobscured travel of the electrons. The electrons reaching the end of the drift tube are accelerated onto the MCP, which amplifies the signal so that it can be processed electronically. The flight distance of the electrons is about 60 cm so that electrons with 40 eV kinetic energy need about 160 ns to travel this distance. The energy resolution is in principle determined by the time-of-flight and the temporal resolution of the detector electronics. A key parameter is the dead time of the MCP and read-out electronics, which determines how long after an event the electronics need for the next event to be recorded. The MCP dead time is very small due to the large amount of channels, which can detect electrons simultaneously. However, the read-out electronics put limits on the dead time of the system. In addition, the time resolution of the MCP and amplifier determines whether two consecutive events can be resolved in time, so that the read-out electronics have a chance to register both events. A NIM module converts the analog signal of the MCP into standardized NIM pulses, which are then counted by a computer scalar card. Once completely assembled and installed, the streak camera will add a powerful tool for pulse characterization to the beamline and it will be used in quantum dynamics measurements to complement transient absorption spectroscopy.

3.4 Data processing

The handling of spectroscopic data is described in detail in Ref. [88], so that the description here is restricted to the most important basics.

For the data shown in this thesis, the hardware binning mode of the CCD camera was used, which records a one-dimensional array of intensity values. Each value is collected from a vertical strip of camera pixels over a user-defined range. In order to calibrate the photon energy axis, several absorption lines of known energy are used to establish a calibration function, which converts pixel number to photon energy. Therefore, the exact resonance position on the camera chip is fitted for each spectral line and the discrete points are interpolated with a parabolic function. In order to reconstruct the absorption spectrum, knowledge of the background and a reference are necessary. The background $B(\omega)$ is determined by shutting all gas valves, so that only NIR stray light leaking on the camera chip and the camera noise itself contribute to the image. The reference $R(\omega)$ is recorded with XUV light but no absorbing target, in order to compare it to the actual measurement $M(\omega)$ to determine the optical density $\mathrm{OD}(\omega)$ of the gas target. Ideally, the relation between these quantities is given by

$$M(\omega) = B(\omega) + (R(\omega) - B(\omega))10^{-\mathrm{OD}(\omega)}, \tag{3.2}$$

which allows for the determination of OD from the three measured spectra. However, due the fluctuations of (mainly) the laser pulse energy, which is amplified due to the nonlinearity of HHG, it is often the case that measurement and reference cannot be compared to each other because the overall shape of the spectrum fluctuates. There are currently three ways to deal with this problem. The first, and most direct way, is to simultaneously record measurement and reference. This implies that a portion of the XUV light has to be picked off before the interaction with the gas target and has then to be recorded be another XUV spectrometer. Such a technique will be implemented in a new version of the current beamline, which is currently set up. The second approach to generate a useful reference is to derive it from the measurement. For spectral lines that are narrow compared to the overall structure of the spectrum, which is mainly determined by the harmonic modulation of approximately 3.5 eV, a lowpass filter can be effectively applied to the spectrum in order to remove these lines. The spectrum without the resonance lines serves then as a reference. This approach, for instance, works well for the narrow lines of doubly excited helium. However, the non-resonant absorption due to transitions to the continuum is not retrieved by this method. If the absorption lines are too broad, the lowpass filtering will introduce artifacts. In this case, one can try to roughly remove the absorption lines from the spectrum previously in order to support the lowpass filter. A third approach is to construct a reference from a set of measured references that matches best with the absorption experiment data. The construction might be realized as a linear combination of measured references or by singular value decomposition (see e.g. Ref. [108]).
With that the major processing of experimental data is accomplished and further analysis, which is presented in the subsequent chapters, can be performed.

Chapter 4

The dipole control model

The following chapter deals with a physical description of impulsive quantum control that is the basis for the methods described in chapters 5 and 6 as it helps to bridge the gap between time and frequency domain in a comprehensive analytical way. Furthermore, it allows to retrieve amplitude and phase information about light–matter interaction processes from time-resolved spectra. In the model conceived and developed in this thesis, the system is described via its dipole moment, which is controlled in the time domain—it is thus named *dipole control model* (DCM). The main content of this chapter has been published in Ref. [1], so that the presentation will adhere closely to the publication.

4.1 General concept

The starting point is the temporal dipole response $d(t)$ of an isolated quantum state after excitation by an ultrashort light pulse $E_{\mathrm{ex}}(t)$, e.g. an attosecond XUV pulse, at time $t = 0$. The pulse duration shall be small compared to the lifetime of the excited state so that it can be approximated by a Dirac-δ function. As the dipole response oscillates with the resonance frequency ω_{r} it is subject to an exponential decay with a decay rate Γ (Fig. 4.1 (a)). To calculate the dipole response, first-order time-dependent perturbation theory can be used. The coefficient of the excited state $|1\rangle$ is given by

$$c_1(t) = \frac{1}{i\hbar}\int_0^\infty e^{i\omega_{\mathrm{r}}t'}\,\langle 1|\,d\,E_{\mathrm{ex}}(t)\,|0\rangle\,\mathrm{d}t' = \frac{1}{i\hbar}d_{10}E_0 \tag{4.1}$$

Here, d is the dipole operator, $|0\rangle$ is the ground state (energy is chosen to be 0), $d_{10} = \langle 1|\,d\,|0\rangle$ is the dipole matrix element between ground and excited state, and E_0 is the amplitude of the Dirac-δ pulse. With that the wave function $|\psi(t)\rangle$ evaluates to

$$|\psi(t)\rangle = |0\rangle + \frac{1}{i\hbar}d_{10}E_0 e^{-i\omega_{\mathrm{r}}t}\,|1\rangle \tag{4.2}$$

from which the time-dependent dipole moment can be calculated as the expectation value of the dipole operator:

$$d(t) = \langle\psi(t)|\,d\,|\psi(t)\rangle = \frac{1}{i\hbar}E_0\,{d_{01}}^2\left[e^{-i\omega_{\mathrm{r}}t} - e^{i\omega_{\mathrm{r}}t}\right] = \frac{-2E_0\,{d_{01}}^2}{\hbar}\sin(\omega_{\mathrm{r}}t) \tag{4.3}$$

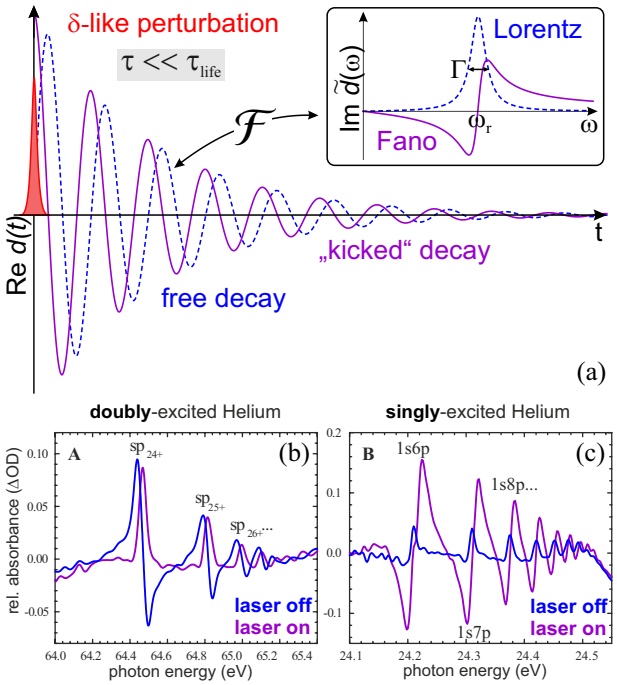

Fig. 4.1: *(a) Excitation (not shown) followed by a free decay (dashed blue) and phase-kicked decay (solid purple) due to interaction with a second dressing laser pulse (red) directly after the excitation step. The corresponding spectral response is displayed in the inset. (b) Natural Fano lines (red) of doubly excited states of helium are transformed to a symmetric Lorentzian line (blue) upon interaction with an NIR pulse. (c) Same situation as in (b) but for singly excited helium where the natural line shape is Lorentzian and can be transformed into a Fano-like line shape by virtue of the laser pulse. The data of (b) and (c) is taken from [26]*

Here, the relation $d_{01} = d_{10}^*$ was used. Introducing an exponential decay of the wave function $\exp(-\Gamma/2t)$ leads to the same exponential behavior of the dipole moment. To simplify the analytical treatment, a complex representation of $d(t)$ is chosen, which is equivalent to treating only the positive frequencies of the spectrum and thus justified for the considerations presented here. This leads to the dipole response that will be used in the following:

$$d(t>0) \propto i e^{i\omega_r t - \frac{\Gamma}{2}t}. \tag{4.4}$$

The spectral line shape of the absorption cross-section $\sigma(\omega) \propto \omega \,\mathrm{Im}\left[\tilde{d}(\omega)/\tilde{E}(\omega)\right]$ associated with this freely decaying dipole is determined by the imaginary part of the Fourier transform of Eq. 4.4:

$$\mathrm{Im}\left[\tilde{d}(\omega)\right] = \mathrm{Im}\left[\int_{-\infty}^{\infty} d(t) e^{-i\omega t} \mathrm{d}t\right] \propto \mathrm{Im}\left[\frac{i}{i(\omega-\omega_r)+\Gamma/2}\right] \tag{4.5}$$

This is because the spectrum of the δ-like pulse is uniform and the factor ω can be neglected for the common case of $\Gamma \ll \omega_r$. Therefore, the imaginary part of the dipole response is regarded as the main observable in transient absorption measurements using ultrashort excitation pulses. Equation 4.5 resembles a Lorentzian line centered about ω_r with its full width at half maximum (FWHM) equal to the decay rate Γ. By adding an initial phase ϕ_0 to the dipole oscillation of Eq. 4.4, the absorption line shape can be continuously converted into a Fano-like line shape [26]. Furthermore, a direct relation between ϕ_0 and the Fano-q-parameter can be found:

$$\phi_0 = 2\arg(q-i) \quad \leftrightarrow \quad q = -\cot\left(\frac{\phi_0}{2}\right) \tag{4.6}$$

It was experimentally demonstrated that the initial phase of the dipole response can be effectively controlled by means of an ultrashort NIR laser pulse dressing the excited state

right at the beginning of the decay [26]. In the corresponding absorption spectra, the spectral line could be modified substantially: the original asymmetric Fano line shape due to the autoionizing nature of the studied states (see Sec. 2.6) could be converted into a symmetric Lorentzian line shape and *vice versa* by controlling the NIR intensity as shown in Fig. 4.1 (b) and (c). Thereby, absorption could be transformed into transparency or even gain. The underlying physical mechanism was identified to be a non-resonant shift of the excited state's energy due to the laser dressing, which causes a phase shift if integrated over a certain time: the phase gets a *kick* with respect to the free decay (Fig. 4.1 (a)). If the delay τ between the excitation and the dressing laser is small compared to the lifetime of the excited state, and if the dressing laser pulse duration is also much shorter than the lifetime, it could be shown that the line shape is well described by the general Fano formula.
For the DCM, this restriction is lifted making the time delay a completely accessible dimension allowing for the interpretation of time-resolved measurements. In the following, a second laser pulse interacting with the system at arbitrary time delay τ is introduced to the model. This gives rise to a perturbed dipole decay or (macroscopically) a perturbed polarization decay [45, 100].
Because of the δ-approximation of both optical pulses, which again is justified if the pulse durations are short compared to the state's lifetime, the excitation / dressing scheme of ATAS can be divided in three temporal regions. For $t < 0$ the excitation pulse did not act so that the excited state is empty, which leads to a vanishing dipole response. The second region is the region of free decay, which begins at the time of excitation $t = 0$ and ends at $t = \tau$ as soon as the dressing laser pulse arrives. In this region, the dipole response is governed by the field-free dynamics as derived above

$$d(0 < t < \tau) \propto i e^{i\omega_r t - \frac{\Gamma}{2}t} = f_1(t). \tag{4.7}$$

The dressing laser field will then impulsively interact with the system and this interaction will leave its fingerprint in the dipole response. However, after the interaction the system is again field free and evolves naturally. Hence, the dipole response after the dressing laser pulse can in general be written as the field-free response, i.e. f_1, modified in amplitude and phase, which shall be described by the complex dipole control parameter A:

$$d(\tau < t) \propto A\, f_1(t) \tag{4.8}$$

By choosing A, a variety of light–matter interaction processes can be modeled. For example a pure modification of the dipole phase, i.e. $|A| = 1$, can be used to simulate the effect of a non-resonant energy shift, whereas a pure modification of the amplitude, i.e. $\mathrm{Im}[A] = 0$, can be used to model ionization of the excited state. In general, A depends on the time delay τ with $A(\tau < 0) = 1$.
Combining the three temporal sections to a piecewise function yields:

$$d_\tau(t,\tau) \propto \begin{cases} 0 & t < 0 \\ f_1(t) & 0 < t < \tau \\ A(\tau) f_1(t) & t > \tau \end{cases}, \tag{4.9}$$

which is the central time-domain equation of the DCM and which is illustrated in Fig. 4.2 (a). The structure of A can often be described as one of two prototype structures:

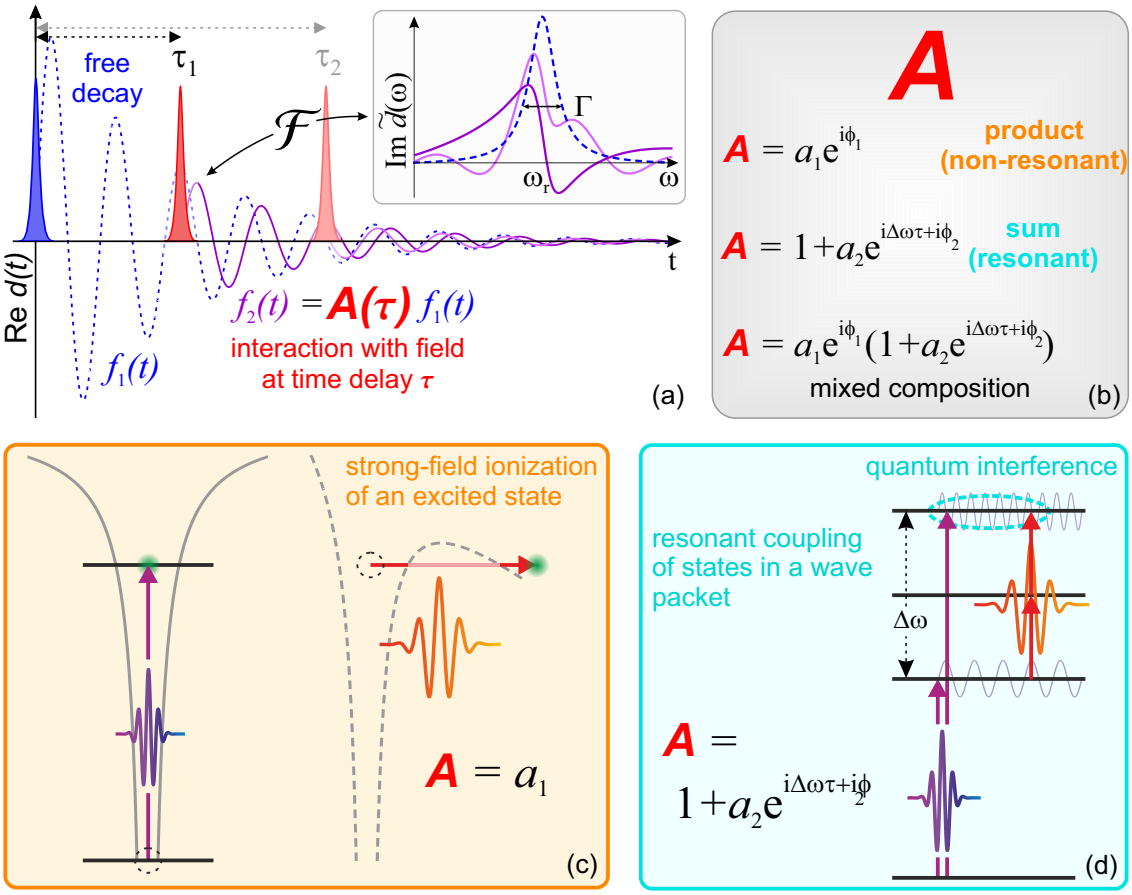

Fig. 4.2: *(a) Illustration of the dipole control model. The excitation (blue pulse) is followed by free decay (dashed blue), which is interrupted by the dressing pulse (red) at arbitrary time delay (τ_1). The perturbed dipole decay (solid purple) gives rise to a modified spectrum (see inset). The perturbation is parametrized by the complex quantity A. Pale colors indicate a different time-delay (τ_2) leading to a different spectrum. (b) Structure of the complex dipole control parameter A, which modifies the dipole response after interaction of the excited state with the laser pulse (in δ-approximation) and leads to a perturbed dipole decay. Different types of interaction are described by different structures of A as described in detail in the main text. (c) Example for a non-resonant type of interaction. In strong-field ionization, the real $A = a_1$ resembles the part of the dipole moment that remains bound after the ionization event. (d) Example for a resonant type of interaction. During the excitation a coherent superposition of two dipole-allowed states, i.e. a wave packet, is created. Depending on the timing τ of the dressing laser pulse, either a portion in-phase or out-of-phase (or anywhere in between) is added to the wave function, leading to an increased or decreased state amplitude, and thus an increased or decreased dipole moment. The perturbative treatment of the two-photon transition via an intermediate state yields A and leads to a quantum path interference with the beat frequency $\Delta\omega$ given by the level spacing.*

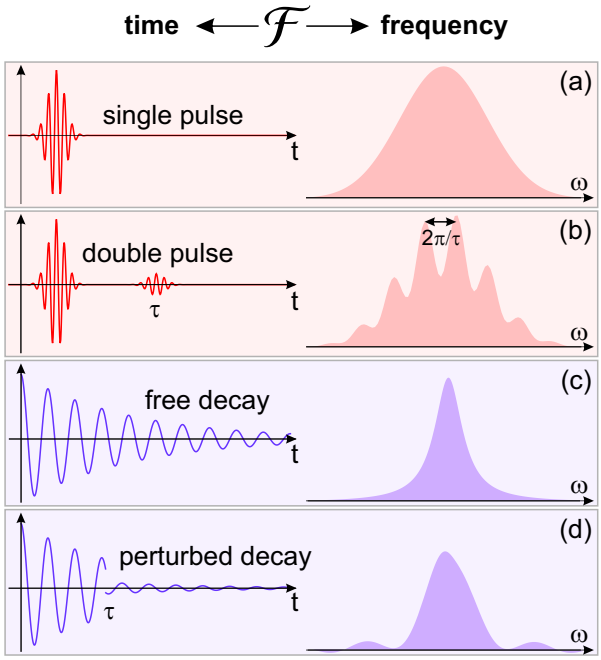

Fig. 4.3: *Spectral interference: comparison of laser pulses and (perturbed) dipole response. (a) Single laser pulse featuring a smooth spectrum. (b) The presence of a time-delayed (time delay τ) second pulse leads to a sinusoidal modulation of the spectrum with a fringe spacing of $2\pi/\tau$. This is caused by spectral interference: the spectral components of the two pulses have different spectral phases due to the delay of the second pulse with respect to the first pulse (see Sec. 2.1.1), so that an interference pattern arises. (c) In the case of the free decay—similar to the single pulse—all components interfere constructively leading to a sharp and smooth absorption spectrum. (d) Interference of the perturbed part with the free part leads to modulations and broadening of the absorption spectrum.*

a product of terms or a sum of terms. The product form $A = a_1 e^{i\phi_1}$ is suitable to describe non-resonant processes like strong-field ionization or non-resonant transient level shifts, e.g. a ponderomotive shift as shown in Chap. 6. On the other hand, the sum form $A = 1 + a_2 e^{i\Delta\omega\tau + i\phi_2}$ is derived from perturbative coupling to another state with an energy separation of $\hbar\Delta\omega$ (see Sec. 2.3, Eq. 2.36). In principle, all parameters may depend explicitly on τ. Figure 4.2 (b) summarizes the fundamental structures and introduces an example of a mixed composition, which can be used to describe a combination of interaction processes. One example of the non-resonant and resonant case is given in Fig. 4.2 (c) and (d), respectively.

4.2 From time domain to frequency domain

Since spectroscopy techniques give access to the spectral representation of the dipole response rather than the time-domain representation, the (complex) time delay–dependent spectrum $\tilde{d}_\tau(\omega,\tau)$ will be derived from Eq. 4.9. The piecewise description of the dipole response makes Fourier transform convenient:

$$\tilde{d}_\tau(\omega,\tau) = \int_{-\infty}^{\infty} d_\tau(t,\tau) e^{-i\omega t}\mathrm{d}t \propto \int_0^\tau f_1(t) e^{-i\omega t}\mathrm{d}t + A(\tau)\int_\tau^\infty f_1(t) e^{-i\omega t}\mathrm{d}t. \tag{4.10}$$

By substituting Eq. 4.7 into Eq. 4.10 the complex spectrum can be calculated analytically without specifying $A(\tau)$:

$$\tilde{d}_\tau(\omega,\tau) \propto i\frac{1 - e^{i(\omega_\mathrm{r}-\omega)\tau - \frac{\Gamma}{2}\tau}(1 - A(\tau))}{i(\omega-\omega_\mathrm{r}) + \Gamma/2} \tag{4.11}$$

In correspondence to Eq. 4.9, this is the central equation of the DCM in the spectral domain. For convenience, Eq. 4.11 shall be simplified by introducing $\gamma = \Gamma/2$, the detuning from the resonance frequency $\delta = \omega - \omega_\mathrm{r}$ (not to be confused with the Dirac-δ function δ_Dirac), and the complex dipole spectrum $\tilde{D}_\tau(\delta,\tau) = \tilde{d}_\tau(\omega_\mathrm{r}+\delta,\tau)$. With that, Eq. 4.11 reduces to

$$\tilde{D}_\tau(\delta,\tau) \propto -\frac{1-e^{-i\delta\tau-\gamma\tau}(1-A(\tau))}{\delta - i\gamma} \tag{4.12}$$

Note that, for simplicity the functions and equations presented throughout the thesis depend on the angular frequencies ω or δ and ν. However, in the figures containing experimental data or simulations of experimental situations, the data will explicitly depend on the XUV photon energy $\hbar\omega$ or the Fourier energy $\hbar\nu$ with electron volts (eV) as the standard unit. The time delay τ is used in units of femtoseconds.

Equation 4.12 already gives insight into the physics going on during a transient absorption experiment. In the case of $A(\tau) = 1$, i.e. in the absence of any interaction between the dressing laser field and the excited state, the term in parentheses equates to 0, so that the complex spectrum becomes independent of τ and yields nothing but the natural line shape of the excited state. If light–matter interaction leads to a perturbed dipole decay, i.e. for $A(\tau) \neq 1$, several complex-valued terms of possibly different phase are present in the numerator. This gives rise to time delay–dependent spectral interference and the according interference patterns. The situation is similar to a double-pulse configuration, which causes a sinusoidal modulation of the spectral intensity compared to a single pulse (Fig. 4.3 (a) and (b)). The same phenomenon leads to the formation of the well-known frequency combs for a long train of pulses [109–111] or the harmonic comb of HHG. In the case of a perturbed dipole decay, the two temporal regions before and after the dressing laser field also interfere spectrally leading to a characteristic modulation of the absorption spectrum as shown in Fig. 4.3 (c) and (d).
The exponential factor $\exp(-\gamma\tau)$ damps the effect of the term in parentheses, i.e. the perturbation, for increasing time delay τ of the perturbation with respect to the excitation. Hence, the line shape converges against the natural line for $\tau \to \infty$ as a steadily decreasing fraction of the decaying dipole response is affected by the dressing laser.
Substitution of $A(\tau)$ in Eq. 4.12 by either the non-resonant case (product form, case 1) or the resonant case (sum form, case 2) enables further evaluation of the complex spectrum as well as of the absorption spectrum given by

$$\sigma_\tau(\delta,\tau) \propto \mathrm{Im}\left[\tilde{D}_\tau(\delta,\tau)\right] \qquad \text{(Sec. 2.4)} \tag{4.13}$$

The complex spectra for the two example cases are

$$\tilde{D}_{\tau,1}(\delta,\tau) \propto -\frac{1-e^{-i\delta\tau-\gamma\tau}(1-a_1 e^{i\phi_1})}{\delta - i\gamma} \tag{4.14}$$

$$\tilde{D}_{\tau,2}(\delta,\tau) \propto -\frac{1-a_2 e^{-i\delta\tau-\gamma\tau}e^{i\Delta\omega\tau+i\phi_2}}{\delta - i\gamma}. \tag{4.15}$$

Evaluating the imaginary part, which is directly proportional to experimental absorption data, of Eq. 4.12, 4.14 and 4.15 yields

$$\sigma_\tau(\delta,\tau) \propto \frac{1}{\delta^2+\gamma^2}\left[\gamma + e^{i\delta\tau-\gamma\tau}(\gamma+i\delta)\,(A(\tau)-1)\right] + \text{c.c.} \tag{4.16}$$

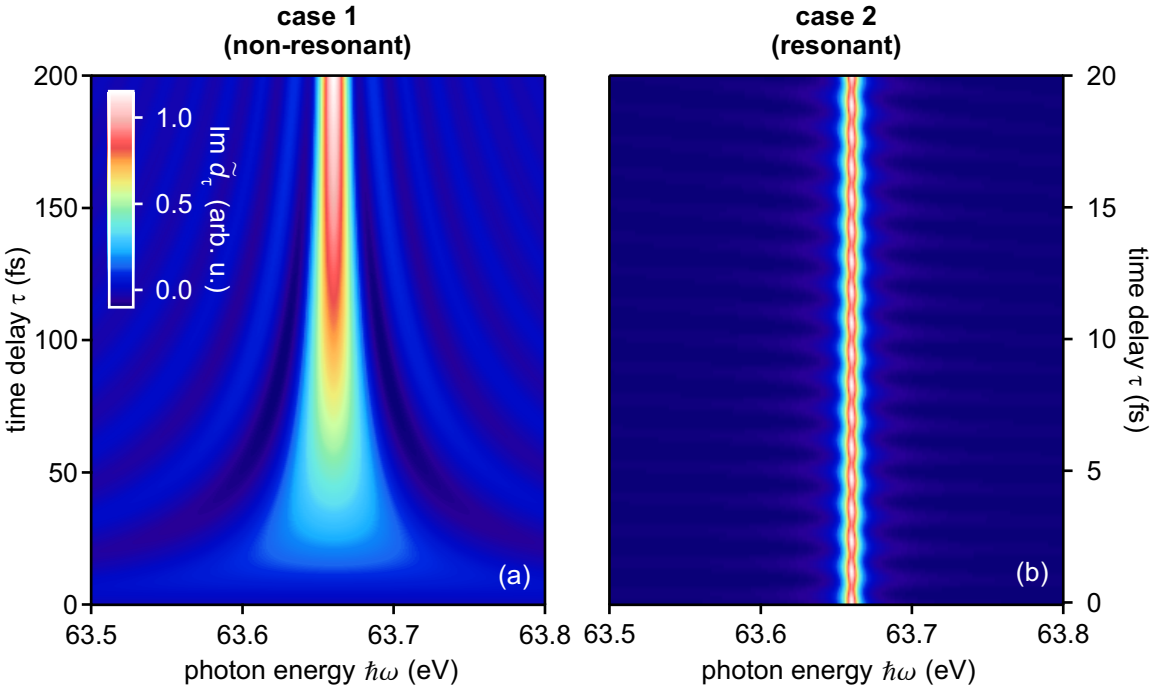

Fig. 4.4: *Time-resolved absorption spectra analytically calculated with the DCM. (a) Simulated strong-field ionization of an excited state (as in Fig. 4.2 (c)) for different time delays between XUV and strong-field pulse as an example of the non-resonant-type interaction. The absorption spectrum is described by Eq. 4.17 with parameters $a_1 = 0$ and $\phi_1 = 0$ to model complete ionization of the state via the NIR pulse. (b) Resonant coupling of excited states (as in Fig. 4.2 (d)) according to Eq.4.18 with $a_2 = 0.1$, $\phi_2 = \pi$, and $\hbar\Delta\omega = 3.5$ eV. The beating structure is a signature of quantum-path interference processes.*

for the general case,

$$\sigma_{\tau,1}(\delta,\tau) \propto \frac{1}{\delta^2+\gamma^2}\left[\gamma + e^{i\delta\tau-\gamma\tau}(\gamma+i\delta)\left(a_1 e^{i\phi_1}-1\right)\right] + \text{c.c.} \tag{4.17}$$

for the non-resonant case, and

$$\sigma_{\tau,2}(\delta,\tau) \propto \frac{1}{\delta^2+\gamma^2}\left[\gamma + a_2 e^{i(\delta+\Delta\omega)\tau-\gamma\tau}(\gamma+i\delta)e^{i\phi_2}\right] + \text{c.c.} \tag{4.18}$$

for the resonant case. Figure 4.4 shows a calculated example spectrum for each case based on Fig. 4.2 (c) and (d). The spectra exhibit characteristic structures that are commonly observed in many recent attosecond transient absorption studies [6, 39, 45, 79, 112–117]. Figure 4.4 (a) shows hyperbolic features along curves of $\delta \times \tau = \text{const.}$, which are accompanied by spectral broadening for decreasing time delay. The spectral broadening can be readily understood since early ionization ($\tau \to 0$) terminates the dipole response after much less than its natural lifetime. Thus, according to the time-energy uncertainty, a fine spectral feature cannot develop and the spectral bandwidth is proportional to $1/\tau$. The abrupt vanishing of the dipole oscillation due to strong-field ionization also causes the hyperbolic structures. The physical mechanism behind is the intrinsic Fourier transform performed by the spectrometer on a decaying signal that stops fast compared

to the natural lifetime. In analogy to that, a numerical Fourier transform performed on a decaying function before the amplitude has declined enough, e.g. due to a limited grid, causes the same effect in the form of an artifact. However, in the case of light–matter interaction that strongly modifies the dipole oscillation amplitude on a time scale faster than the lifetime, such as strong-field ionization does, the *artifact* is real and can be measured as demonstrated in the following chapters.
This strong modification of the absorption spectrum is absent in Fig. 4.4 (b) due to the perturbative nature of the modeled light–matter interaction process. In contrast to Fig. 4.4 (a), Fig. 4.4 (b) exhibits a fast τ-dependent modulation of the optical density due to quantum path interference (see Fig. 4.2 (d)). The apparent rippling structure becomes tilted for increasing τ, which is due to the $\exp[i(\delta+\Delta\omega)\tau]$ term in Eq. 4.18. Physically, the transition frequency towards the coupled state is lower on one side of the spectral line's center frequency and higher on the other side, which causes the rippling period to vary across the spectral line introducing the observed tilt. In principal, the tilting of the rippling has the same origin as the hyperbolic structures - the effect is just frequency shifted by $\Delta\omega$.

In summary, the presented dipole control model is a general framework, which helps to understand resonant and non-resonant time delay–dependent dipole dynamics driven by ultra-short laser pulses. As will be shown in the subsequent chapters, the analytically calculated absorption spectra can be used to extract amplitude (e.g. a_1 and a_2) and phase (e.g. ϕ_1, ϕ_2, and $\Delta\omega$) from measured spectra. This allows for a precise characterization of light–matter interaction processes (Chap. 5) as well as characterization of the intense few-cycle laser pulses that are used to drive such processes (Chap. 6).

Chapter 5

Two-dimensional absorption spectroscopy (2DAS)

The conventional attosecond transient absorption spectroscopy, as introduced in Sec. 3.1, is a very powerful technique as it allows to both access and also to control the ultrafast dynamics of a quantum system via the experimental outcome: a time-, or actually time delay–, resolved spectrum. These features, however, come at the expense of typically fairly complicated-structured spectra containing the signatures of several different processes. Therefore, individual processes can hardly be separated, analyzed and understood. This is especially the case for strong and ultrashort broadband laser pulses where a variety of effects can occur simultaneously.
This raises the question if there is an alternative or even better way to study quantum dynamics than by analyzing the time-resolved absorption spectrum. The answer to this question is the content of this chapter. By performing a Fourier analysis along the time-delay axis a complex-valued two-dimensional spectral representation of the information encoded in the time-resolved absorption spectrum is created (Fig. 5.1). It will be shown by means of an analytic theory based on the dipole control model (DCM) of the preceding chapter that by this procedure different coupling pathways are spectroscopically separated. This allows different pathways of light–matter interaction to be analyzed separately. The two-dimensional representation will in the following be referred to as two-dimensional absorption spectrum (2DAS) and the technique itself as two-dimensional

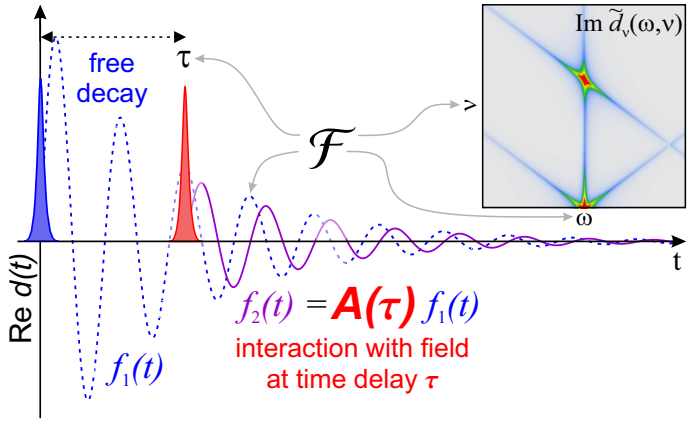

Fig. 5.1: *Schematic of two-dimensional absorption spectroscopy (2DAS). The temporal description of the dipole control model (Eq. 4.9) is transformed into a two-dimensional–spectroscopic representation by performing two Fourier tranforms: along the time axis (done by the spectrometer in the experiment) and the second one along the time-delay axis.*

absorption spectroscopy (also 2DAS). Furthermore, also by means of the DCM, it is possible to extract amplitude and phase modifications imprinted by the laser–atom interaction onto the atomic resonances. This makes 2DAS a powerful complement to the conventional transient absorption spectroscopy.
Besides that, 2DAS can be regarded as one of the first experimental steps towards traditional (four-wave-mixing-type) two-dimensional spectroscopy [118–121] with attosecond pulses in the XUV as theoretically described in Refs. [122, 123]. 2DAS is in principle a two-color (NIR and XUV) nonlinear method (e.g. four-wave-mixing in the case presented in the second section of this chapter), and by choosing the two-dimensional–spectral representation, similar to traditional two-dimensional spectroscopy, couplings between different coherently excited states are revealed. This provides the key to understand the dynamics of transiently coupled—or more general laser-dressed—states.
The chapter is divided as follows: First the analytical framework based on the DCM is developed where the focus is placed on the 2DAS representation of the non-resonant and resonant prototype examples of Chap. 4. Afterwards, the theoretical knowledge is applied to experimental and simulated data of doubly excited states of helium excited by attosecond XUV light and dressed by a few-cycle NIR laser pulse.
Further applications of the method are presented in Sec. 5.3, where a spin–orbit wave packet is created by inner-valence excitation of xenon, and is afterwards exposed to intense NIR light, is studied.
The majority of the content of the first two sections (5.1 and 5.2) of this chapter was published in Ref. [1]. Therefore, the content will adhere closely to the publication.

5.1 Dipole control model for 2DAS

In the following the 2DAS representation of the time delay–resolved spectrum introduced in Sec. 4.2 will be derived, which enables interpretation of experimental data shown in the next section. It will be demonstrated that amplitude and phase information on the laser-induced modification of the excited quantum state can be retrieved from the 2DAS.
The 2DAS is created from the time-resolved absorption spectrum by Fourier transform along the time-delay axis, thus transforming the time delay τ into a frequency ν, which in the following shall be denoted as Fourier frequency. The 2DAS is defined as

$$\tilde{D}_\nu(\delta,\nu) = \int_{-\infty}^{\infty} \mathrm{Im}\left[\tilde{D}_\tau(\delta,\tau)\right] e^{-i\nu\tau}\mathrm{d}\tau \tag{5.1}$$

where $\mathrm{Im}\left[\tilde{D}_\tau(\delta,\tau)\right]$ is directly proportional to the experimentally observable absorption cross section σ. The general expression for the complex time-dependent spectrum $\tilde{D}_\tau(\delta,\tau)$ was derived in the framework of the DCM and is given by Eq. 4.12. The two spectral dimensions $\omega = \omega_\mathrm{r} + \delta$ and ν belong to the frequency ranges of the excitation and interaction/dressing pulse, respectively. Although in the studies presented in this thesis attosecond pulses of XUV light are used for the excitation and femtosecond NIR pulses are used for the interaction, the approach is completely general and not limited to these spectral regions. Since the NIR pulse intensity can be tuned sufficiently high in order to drive nonlinear processes, the range of ν values can extend to multiples of the NIR spectrum. For example a two-NIR-photon process, such as the coupling of two states of the

same parity will contribute to the range of frequencies around twice the NIR frequency. A highly nonlinear process, such as strong-field ionization, will lead to even higher energy components of the ν-spectrum. In order to proceed with the evaluation of the 2DAS, the general form of $\mathrm{Im}\left[\tilde{D}_\tau(\delta,\tau)\right]$ according to Eq. 4.16 is substituted into Eq. 5.1:

$$\tilde{D}_\nu(\delta,\nu) \propto \frac{1}{\delta^2+\gamma^2}\int_{-\infty}^{\infty}\left\{\left[\gamma + e^{i\delta\tau-\gamma\tau}(\gamma+i\delta)\left(A(\tau)-1\right)\right]+\mathrm{c.c}\right\}e^{-i\nu\tau}\mathrm{d}\tau. \tag{5.2}$$

The first summand is constant and yields a Dirac-δ function $\delta_{\mathrm{Dirac}}(\nu)$. In the case of no interaction of the sample with the second laser, i.e. $A(\tau)=1$, the rest of the terms cancels leading to

$$\tilde{D}_\nu(\delta,\nu) \propto \frac{\gamma}{\delta^2+\gamma^2}\,\delta_{\mathrm{Dirac}}(\nu) \qquad \text{no interaction.} \tag{5.3}$$

This is the well-known Lorentzian line shape along the ω axis, confined to the DC limit ($\nu=0$) of the Fourier frequency axis due to the absence of any modulation in the spectrum. Without specifying $A(\tau)$ the rest of the integration can only be performed to a certain extent. By defining $\mathscr{A}(\tau)=A(\tau)-1$ the integration of the τ-dependent part can be cast into the form

$$\int_0^{\infty}\left\{\left[e^{i\delta\tau-\gamma\tau}(\gamma+i\delta)\mathscr{A}(\tau)\right]+\left[e^{-i\delta\tau-\gamma\tau}(\gamma-i\delta)\mathscr{A}(\tau)^*\right]\right\}e^{-i\nu\tau}\mathrm{d}\tau. \tag{5.4}$$

The lower integration limit was set to 0 because $\mathscr{A}=0$ for $\tau<0$ (no effect of the interaction pulse if it appears before the excitation). The exponential factor $\exp(\pm i\delta\tau-\gamma\tau)$ gives rise to a complex line shape (Lorentzian) as a function of ν centered about $\pm\delta$:

$$(\gamma\pm i\delta)\int_0^{\infty}e^{\pm i\delta\tau-\gamma\tau}e^{-i\nu\tau}\mathrm{d}\tau = \frac{\gamma\pm i\delta}{i(\nu\mp\delta)+\gamma} = \mathscr{L}_\delta^{\pm}(\nu). \tag{5.5}$$

Using the convolution (symbol $*$) theorem of Fourier transform, this yields the final and most general expression for the 2DAS:

$$\tilde{D}_\nu(\delta,\nu) \propto \frac{1}{\delta^2+\gamma^2}\left[2\gamma\delta_{\mathrm{Dirac}}(\nu)+\left(\mathscr{L}_\delta^{+}*\tilde{\mathscr{A}}\right)(\nu)+\left(\mathscr{L}_\delta^{-}*\tilde{\mathscr{A}}^*\right)(\nu)\right] \tag{5.6}$$

where $\tilde{\mathscr{A}}$ and $\tilde{\mathscr{A}}^*$ are the Fourier transforms of $\mathscr{A}$ and $\mathscr{A}^*$, respectively.
For the further discussion, it is more helpful to consider the two prototype cases of $A(\tau)$ presented in Chap. 4 instead of working with the most general form. Therefore the product form $A=a_1e^{i\phi_1}$ suitable for non-resonant processes, and the sum form $A=1+a_2e^{i\Delta\omega\tau+i\phi_2}$ describing resonant coupling of states are inserted into Eq. 5.2. The result of the calculations and their physical interpretation are presented in the following subsections.

5.1.1 Non-resonant type of interaction

For the non-resonant interaction, Eq. 5.2 becomes

$$\tilde{D}_{\nu,1}(\delta,\nu) \propto \frac{1}{\delta^2+\gamma^2}\int_{-\infty}^{\infty}\left\{\left[\gamma + e^{i\delta\tau-\gamma\tau}(\gamma+i\delta)\left(a_1e^{i\phi_1}-1\right)\right]+\mathrm{c.c}\right\}e^{-i\nu\tau}\mathrm{d}\tau. \tag{5.7}$$

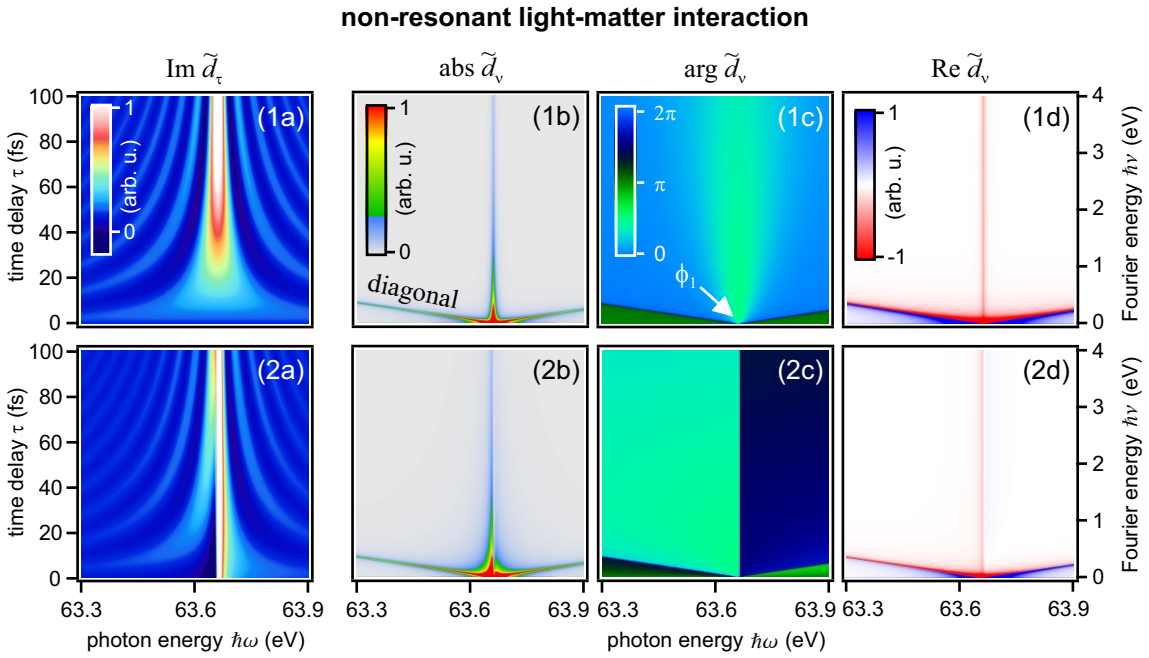

Fig. 5.2: *Analytically calculated time-resolved spectra (a) and corresponding 2DAS (b,c,d) for two examples of non-resonant interaction ($A = a_1 \exp(i\phi_1)$). Row 1 shows complete ionization ($a_1 = 0$, $\phi_1 = 0$) whereas row 2 shows partial ionization ($a_1 = 0.8$) together with a phase shift ($\phi_1 = \pi/4$). The 2DAS is given in terms of magnitude (b), phase (c) and real part (d). The state's resonance frequency is that of the sp_{23+} doubly excited state of helium.*

This integration can be performed analytically giving complete insight into the structure of the two-dimensional spectrum. The result is given by

$$\tilde{D}_{\nu,1}(\delta,\nu) \propto \frac{1}{\delta^2+\gamma^2}\left\{2\,\gamma\,\delta_{\text{Dirac}}(\nu) + \frac{a_1 e^{i\phi_1}-1}{i(\delta-\nu)-\gamma}(\gamma+i\delta) - \frac{a_1 e^{-i\phi_1}-1}{i(\delta+\nu)+\gamma}(\gamma-i\delta)\right\} \tag{5.8}$$

and visualized for two examples in Fig 5.2. The first example shows, as in Chap. 4, the complete ionization of a state ($a_1 = 0$), whereas the second example features partial ionization ($a_1 = 0.8$) combined with a phase shift ($\phi_1 = \pi/4$). Qualitatively the time-delay scans (1a) and (2a) look similar, however, there are two major differences: in (2a), i.e. the incomplete ionization with phase shift, the spectral broadening towards $\tau = 0$ is much less dominant compared to the complete ionization. This is because of the remaining population of the state after the ionization event, which radiates dipole emission leading to a sharp spectral feature. Furthermore, the line shape itself is transformed to an asymmetric Fano-like shape due to the addition of a phase (and is transformed back for $\tau \to \infty$, which exceeds the figure's axis range). In the 2DAS magnitude plots (1b) and (2b) the strong modification of the dipole response is visible as diagonal structures with a slope of 1 that emerge from the resonance position towards both directions. These diagonals are the frequency-space analog to the hyperbolic structures in the time domain. They arise from the two terms

$$\frac{a_1 e^{i\phi_1}-1}{i(\delta-\nu)-\gamma}(\gamma+i\delta) \quad \text{and} \quad -\frac{a_1 e^{-i\phi_1}-1}{i(\delta+\nu)+\gamma}(\gamma-i\delta),$$

which are particular versions of the general formula in Eq. 5.5. They create confined profiles along the lines $\delta \mp \nu = 0$ with a magnitude determined by the absolute value of the complex factor $a_1 e^{\pm i\phi_1} - 1$. The sharp line emerging along the resonance postion ($\delta = 0$ or $\omega = \omega_r$) resembles the bandwidth of the non-resonant process. Since the ionization was modeled as an instantaneous drop in amplitude, the bandwidth is infinite in this case. In reality, the bandwidth is finite as will be shown in Chap. 5.3. The DC part of the 2DAS is dominated by the Dirac-δ function. It resembles the average of all spectra along the time-delay axis. Therefore the DC spectrum is equal to the unperturbed spectrum if the upper integral limit of the Fourier transform is infinite. The phase shift introduced in the second example compared to the first is clearly visible from the different symmetries of the phase distributions in the phase plots (1c) and (2c). In addition to that, the real part contains the information of both amplitude and phase, and is thus a beneficial complement.
Evaluation of Eq. 5.8 on the diagonals further simplifies the description of the 2DAS to

$$\tilde{D}_{\nu,1}(\delta = \pm\nu) \propto -\frac{\left(a_1 e^{\pm i\phi_1} - 1\right)(\gamma \pm i\delta)}{\gamma(\delta^2 + \gamma^2)} \tag{5.9}$$

From the argument of this expression the phase ϕ_1 imprinted by the laser–atom interaction can be retrieved.

5.1.2 Resonant coupling of states

The counter part of Eq. 5.7 for a perturbative treatment of resonantly coupled states reads

$$\tilde{D}_{\nu,1}(\delta,\nu) \propto \frac{1}{\delta^2+\gamma^2} \int_{-\infty}^{\infty} \left\{ \left[\gamma + e^{i\delta\tau - \gamma\tau}(\gamma + i\delta) \left(a_2 e^{i\Delta\omega\tau + i\phi_1} \right) \right] + \text{c.c} \right\} e^{-i\nu\tau} \mathrm{d}\tau, \tag{5.10}$$

and evaluating the Fourier integral yields the closed-form 2DAS:

$$\tilde{D}_{\nu,1}(\delta,\nu) \propto \frac{1}{\delta^2+\gamma^2} \left\{ 2\gamma\delta_{\text{Dirac}}(\nu) + a_2 \left[\frac{e^{i\phi_2}(\gamma + i\delta)}{i(\delta + \Delta\omega - \nu) - \gamma} - \frac{e^{-i\phi_2}(\gamma - i\delta)}{i(\delta + \Delta\omega + \nu) + \gamma} \right] \right\} \tag{5.11}$$

Figure 5.3 illustrates Eq. 5.11 evaluated for two examples that are related to the content of the next section. Both examples feature resonant coupling of the shown state to another coherently populated state displaced by $\Delta\omega$. As it was demonstrated earlier (Fig. 4.4), this coupling amongst the states of a wave packet leads to a fast modulation of the target's optical density as a result of interference. The beat frequency on resonance is given by the level spacing $\Delta\omega$. In the 2DAS magnitude plots (1b) and (2b), this leads to a well-defined peak at $\nu = \Delta\omega$ for $\delta = 0$ (resonance condition), which is accompanied by a diagonal line. In general, Eq. 5.11 gives rise to such diagonal structures along the lines $\delta + \Delta\omega \mp \nu = 0$ similar to the non-resonant case. Multiplication with the prefactor $1/(\delta^2 + \gamma^2)$ produces a pronounced peak at the center of the diagonal. The amplitude of this peak is directly proportional to the coupling strength parameter a_2. This allows for the characterization of a_2 as a function of the laser intensity for instance to analyze the power scaling of light–matter interaction processes. The main difference compared with the non-resonant case is the displacement of the diagonal line by $\Delta\omega$. In addition, this displacement leads to a single diagonal (in the $\nu > 0$ halfspace) as compared with the two diagonals of the

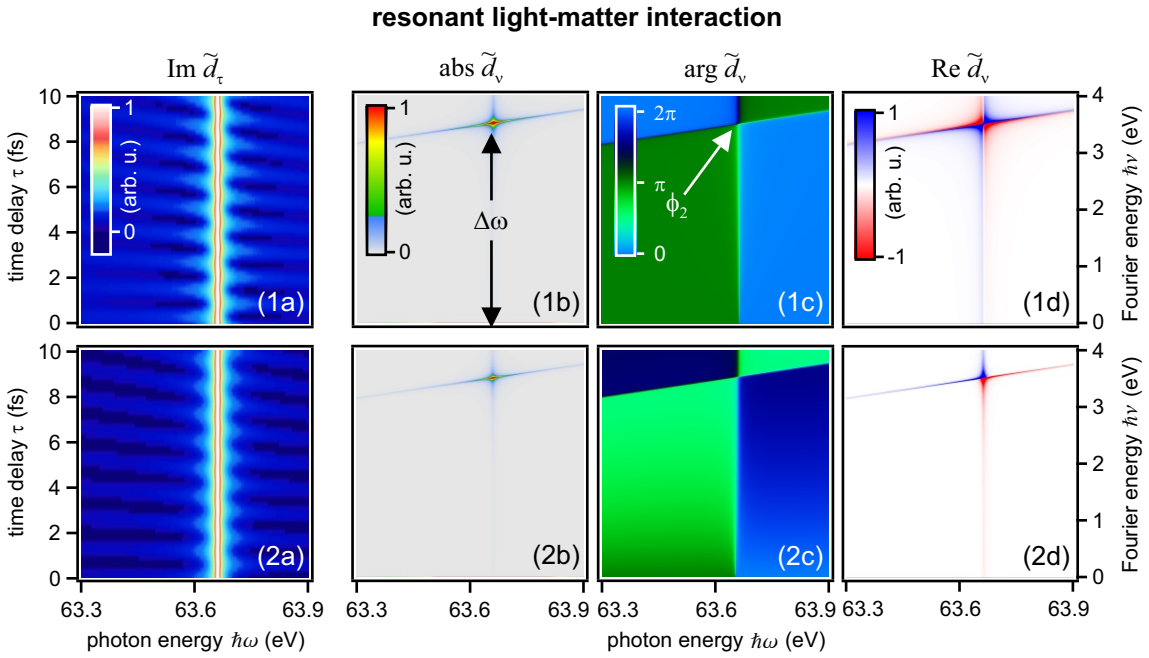

Fig. 5.3: *Analytically calculated time-resolved spectra (a) and corresponding 2DAS (b,c,d) for two examples. Both rows show absorption spectra of a state perturbatively coupled to another coherently excited state ($A = 1 - a_2 \exp(i\Delta\omega\tau + i\phi_2)$). Row 1 depicts the case of stronger coupling ($a_2 = 0.1$) with a phase shift of $\phi_2 = \pi$ whereas row 2 is the case of weaker coupling ($a_2 = 0.05$) and less phase shift ($\phi_2 = \pi/2$). The state's resonance frequency is that of the sp_{23+} doubly excited state of helium and the energy spacing of $\hbar\Delta\omega = 3.51\,eV$ was chosen to match the energy spacing between 2s2p and sp_{23+}.*

non-resonant case. This single line is oriented such that it points towards the resonant coupling partner on the δ (or ω) axis making identification of coupled states easy. This is especially helpful if the coupling partner is dipole forbidden with respect to the ground state and yet coherently excited in the excitation step (e.g. due to a two-photon excitation enabled by residual NIR light in the excitation step because of leakage through the metal filters). In that case, the even-parity coupling partner is hidden in the XUV spectrum but in the 2DAS its presence is revealed due to the diagonal pointing to its energy position. In a recent work [9], the probing of such coupling dynamics between states of opposite parity in inner-valence excited neon has been demonstrated. In general these diagonal structures are the Fourier representation of the tilted rippling structure observed in the time domain ((1a) and (2a)), which were discussed in Sec. 4.2.

Besides the coupling strength a_2, the two examples of Fig. 5.3 only differ in the amount of phase ϕ_2 imprinted on the state by the coupling. As it was shown in the last subsection, the phase difference can effectively be read from the 2DAS phase plots (1c) and (2c) and the real part plot (1d) and (2d). Here, ϕ_2 clearly determines the symmetry observed in the 2d-map. Moreover, the phase can be extracted from the phase plot directly: On the diagonal Eq. 5.11 reduces to

$$\tilde{D}_{\nu,1}(\delta = \pm\nu - \Delta\omega) \propto -\frac{a_2 e^{\pm i\phi_2}(\gamma \pm i\delta)}{\gamma(\delta^2 + \gamma^2)}, \tag{5.12}$$

and on the peak position ($\delta = 0$) of the diagonal the equations further reduces to

$$\tilde{D}_{v,1}(0, \pm\Delta\omega) \propto -\frac{a_2 e^{\pm i\phi_2}}{\gamma^2}. \tag{5.13}$$

In turn, the laser imprinted phase shift is directly given by

$$\phi_2 = \pm\left(\arg\left[\tilde{D}_{v,1}(0, \pm\Delta\omega)\right] - \pi\right). \tag{5.14}$$

With that, the amplitude (a_2) as well as the phase (ϕ_2) of the perturbation of the state introduced by the laser pulse can be retrieved from the 2DAS, which will be demonstrated experimentally in the following section. Although direct extraction of ϕ_2 from the 2DAS is in principle possible, it shall be noted that in practice it can be more helpful to retrieve the phase from the symmetry of the phase or real part plot. This is due to the fact that, as can be seen in Fig. 5.3 and 5.2, the phase varies rapidly in the interesting region. Combined with a limited resolution in experiments and sophisticated simulations this can result in a high uncertainty of the direct phase extraction.
During the last section, emphasis was put on the fact that both states that are coupled are coherently excited. This is important since the spectral finger print of resonant coupling between an initially populated state ($|a\rangle$) and an initially empty state ($|b\rangle$), e.g. a dipole forbidden state in the absence of NIR leakage, is completely different. The characteristic beating as a result of quantum path interference can only occur if a common clock was initially established by coherent excitation. After a time delay τ the second laser mixes the states, which leads to interference, because their phases evolved at different speeds. If however, one of the states, i.e. $|b\rangle$, is initially empty, the dressing laser pulse moves only population towards $|b\rangle$, whose wave function is not sensitive to the phase of the state $|a\rangle$ coefficient, since the coefficient of $|b\rangle$ was zero. State $|a\rangle$ gets primarily depleted, which is a very similar situation as ionization (Perturbatively, depletion is a first-order process, whereas moving population back is a second-order process. Non-perturbatively, if the dressing pulse is strong or long enough, Rabi-cycling may occur.). Therefore, the spectroscopic signature is that of a slow modulation in the time domain or diagonals around the DC limit in the spectral domain.

The previous examples of resonant and non-resonant type light–matter interaction provide the building blocks for many 2DAS spectra. Yet, owing to simplicity for making the examples comprehensive, the aspect of separating different coupling pathways to analyze them separately, which is one of the main advantages of 2DAS compared with time-resolved spectroscopy, fell short up to this point. Hence, before 2DAS will be applied to experimental and simulated data, a last example shall be given in order to demonstrate the power of the method as a complement to purely time-resolved absorption spectroscopy. Figure 5.4 (a) shows a time-delay scan according to an analytic expression in the framework of the DCM. Besides the low frequency hyperbolic structures next to the absorption peak, the spectrum appears rather noisy without much information. However, casting the time-delay scan into the 2DAS representation (Fig. 5.4 (b) and (c)) reveals that the apparent noise pattern is the result of the superposition of five well defined beat frequencies. From the 2DAS magnitude all 5 frequencies and their respective amplitudes are readily obtained. And from the real part of the 2DAS, the phase jump in every beat signal can be

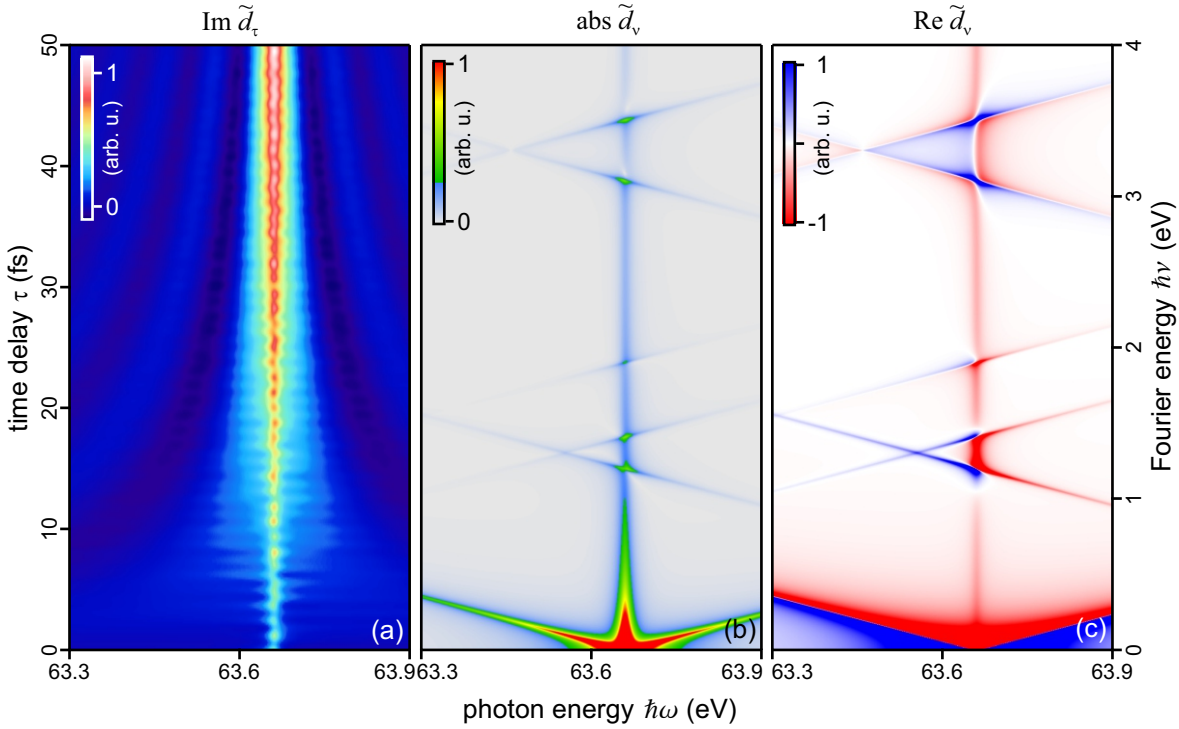

Fig. 5.4: *Analytically calculated time-resolved spectra (a) and corresponding 2DAS magnitude (b) and phase (c). The state undergoes multiple perturbative couplings to neighboring states and a typical non-resonant drop in population due to strong-field ionization.*

retrieved by comparison with patterns of known phase jump: The two lower peaks exhibit the same symmetry as the peak in Fig. 5.3 (2d) with $\phi_2 = \pi/2$, whereas the two upper peaks show the same symmetry as Fig. 5.3 (1d) with $\phi_2 = \pi$. The center peak has a phase of $\phi_2 = \pi/4$ making the real part structure of the peak asymmetric. This shows that the—in total six—different light–matter interaction processes featured in this example can be clearly separated and analyzed in a spectroscopic fashion using 2DAS.

5.2 2DAS of doubly excited states in helium—a proof-of-principle experiment

In the following section, the concept and basic understanding of the 2DAS technique in terms of the DCM, which was developed in the last section, will be applied in a proof of principle to experimental data as well as to a non-perturbative few-level simulation of the experimental quantum system. The focus lies on the doubly-excited states of helium in the energy regime between 60 and 65 eV (see Sec. 2.6). Overview spectra of this region are depicted in Fig. 5.5 (a) and (b). The NIR carrier wavelength is 730 nm (1.7 eV) and the peak intensity of the 7 fs pulses is approximately 2×10^{12} W/cm^2.

In order to get more insight into the physical processes occurring in the experiment and to test the understanding of these processes, a numerical simulation was carried out. The

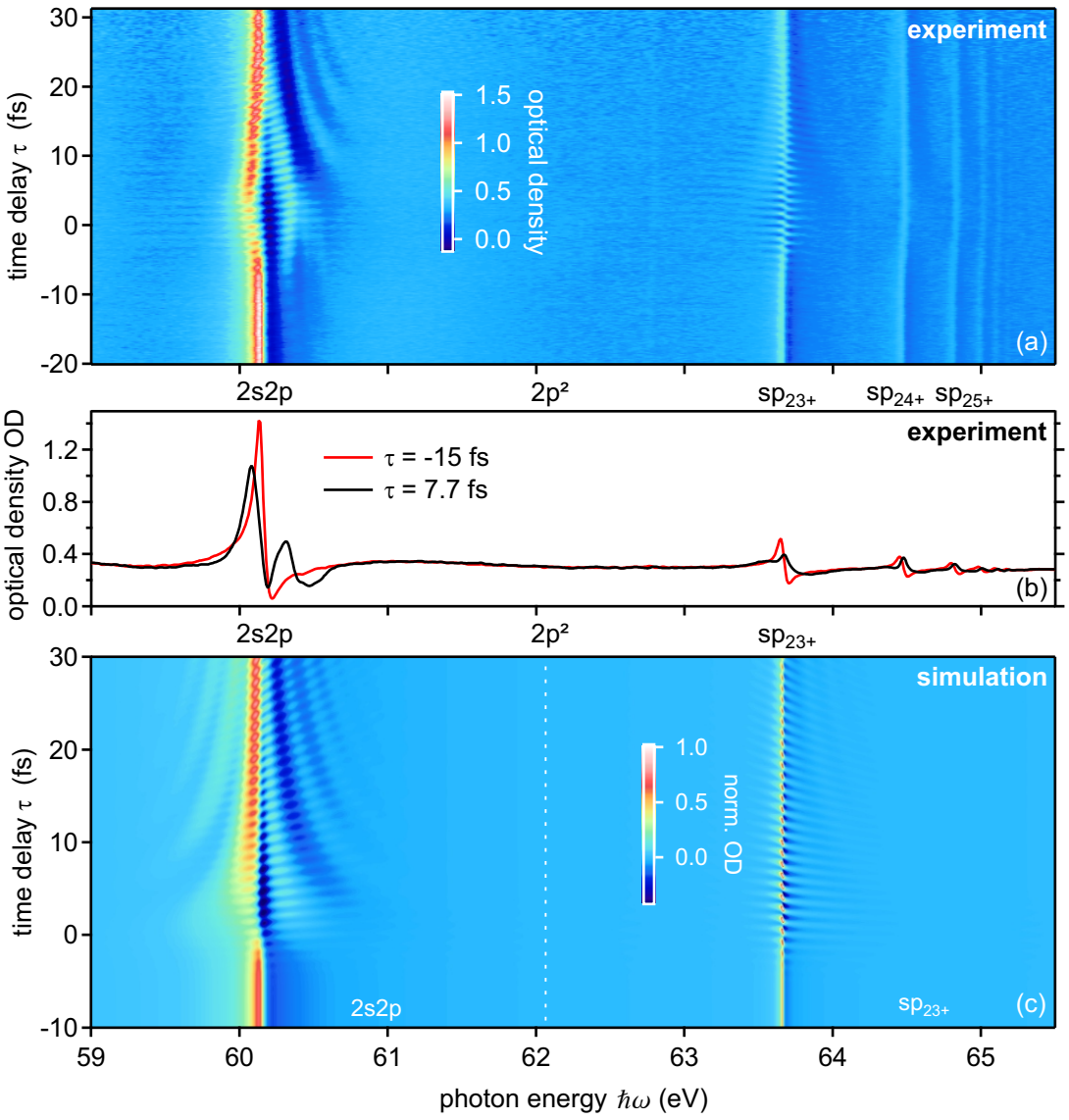

Fig. 5.5: *Overview spectra of the doubly excited manifold of helium between 59 and 65.5 eV. (a) Time-delay scan of 300 steps with a step size of 171 as for an NIR peak intensity of* 2×10^{12} *W/cm*^{2}*. The NIR photon energy is 1.7 eV and its pulse duration is 7 fs. (b) Spectral lineouts of (a) for two different time delays revealing the strong modifications of the system's spectral response upon dressing with a strong NIR laser field. (c) Time-delay scan resulting from a numerical three-level simulation of the 2s2p, 2p*^{2}*, and sp*$_{23+}$ *states dressed by an NIR laser pulse with parameters similar to the experimental conditions.*

heart of the model is a three-level system that consists of the 2s2p state ($|1\rangle$), the $2p^2$ state ($|2\rangle$), and the sp_{23+} state ($|3\rangle$). This three-level system is dressed by a 7 fs FWHM Gaussian laser pulse of 730 nm carrier wavelength. The peak electric field was set to 0.075 atomic units, which corresponds to a peak intensity of 2×10^{12} W/cm^2. The time-dependent Schrödinger equation of this strongly coupled system is given by:

$$i\frac{\partial}{\partial t}\begin{pmatrix}\psi_1(t)\\ \psi_2(t)\\ \psi_3(t)\end{pmatrix} = \begin{pmatrix}E_1+i\gamma_1 & W_{12}(t) & W_{13}(t)\\ W_{21}(t) & E_2+i\gamma_2 & W_{23}(t)\\ W_{31}(t) & W_{32}(t) & E_3+i\gamma_3\end{pmatrix}\begin{pmatrix}\psi_1(t)\\ \psi_2(t)\\ \psi_3(t)\end{pmatrix}. \tag{5.15}$$

The interaction matrix elements W_{ij} are given by the electric field of the dressing NIR laser pulse and the dipole transition matrix element between the respective states:

$$W_{ij} = E_{\mathrm{NIR}}(t)\,\langle i|\,\hat{d}\,|j\rangle = d_{ij}E_{\mathrm{NIR}}(t). \tag{5.16}$$

As both the 2s2p state and the sp_{23+} state are dipole allowed with respect the ground state, they have the same symmetry (P). Hence, the corresponding dipole transition matrix elements and with that the interaction matrix elements vanish:

$$W_{13} = W_{31} = 0. \tag{5.17}$$

Therefore, Eq. 5.15 reduces to

$$i\frac{\partial}{\partial t}\begin{pmatrix}\psi_1(t)\\ \psi_2(t)\\ \psi_3(t)\end{pmatrix} = \begin{pmatrix}E_1+i\gamma_1 & d_{12}E_{\mathrm{NIR}}(t) & 0\\ d_{21}E_{\mathrm{NIR}}(t) & E_2+i\gamma_2 & d_{23}E_{\mathrm{NIR}}(t)\\ 0 & d_{32}E_{\mathrm{NIR}}(t) & E_3+i\gamma_3\end{pmatrix}\begin{pmatrix}\psi_1(t)\\ \psi_2(t)\\ \psi_3(t)\end{pmatrix}, \tag{5.18}$$

which expresses that the coupling between the 2s2p state and the sp_{23+} state is not direct (in the dipole approximation) but mediated by the $2p^2$ state. The time evolution of this system is treated by means of the algorithm described in Sec. 2.2 of the Fundamentals chapter. The only thing missing in order to calculate the time propagation is the initial excitation step. In the experiment the attosecond XUV pulse excites the two dipole allowed states from the $1s^2$ (S^0) ground state ($|0\rangle$). Since the XUV pulse in the experiment is very weak, the excitation step is treated in first-order perturbation theory in the simulation. According to Eq. 2.32, the initially empty states are populated by a 250 as FWHM XUV pulse of 62 eV photon energy:

$$c_j^{(1)}(t) = -\frac{i}{\hbar}d_{0j}\int_0^t e^{i\omega_j t'}E_{\mathrm{XUV}}(t')\mathrm{d}t' \tag{5.19}$$

where the energy of the ground state was set to $E_0 = 0$ and its population to $c_0 = 1$. A discretized version of Eq. 5.19 with built-in decay is used in the actual calculation to modify the excited state population in each time step according to the XUV pulse:

$$\psi_j(k) = \psi_j(k-1)e^{-\gamma_j\Delta t - i\omega_j\Delta t} - i\,\alpha_j E_{\mathrm{XUV}}(k)e^{-\gamma_j\Delta t} \tag{5.20}$$

with the coefficient $\alpha_j = d_{0j}\Delta t/\hbar$. The Fano line shape of the helium doubly excited states, is accounted for by multiplying the dipole moment with the corresponding Fano phase factors (Eq. 4.6) with values taken from [83]. The final time-resolved absorption

E_0	0 eV	γ_0	0 meV		
E_1	60.15 eV	γ_1	37 meV	$d_{12} = d_{21}$	2.2 a.u.
E_2	62.06 eV	γ_2	6.0 meV	$d_{23} = d_{32}$	0.8 a.u.
E_3	63.66 eV	γ_3	8.2 meV	$d_{31} = d_{13}$	0 a.u.
d_{01}^{rel}	1	d_{02}^{rel}	0	d_{03}^{rel}	0.4
q_1	-2.74	q_3	-2.58		
E_{NIR}	0.0075 a.u.	I_{NIR}	2×10^{12} W/cm^2		
T_{NIR}	7 fs	T_{XUV}	250 as		
$\hbar\omega_{\text{NIR}}$	1.7 eV	$\hbar\omega_{XUV}$	62 eV		
Δt	20 as	$\Delta\tau$	100 as		

Table 5.1: *Summary of important parameters in the three-level simulation. The parameters have the following meanings: E_j and γ_j are the state energies and decay rates [81–83]. d_{ij} are the dipole transition matrix elements [87, 89, 124]. d_{0j}^{rel} are the relative dipole moments with respect to the ground state. q_j are the Fano-q-parameters of the doubly excited states [83]. E_{NIR} and I_{NIR} are the dressing laser peak field strength and peak intensity, respectively. T_{NIR} and T_{XUV} are the durations of the femtosecond NIR and attosecond XUV pulses, respectively, and ω_{NIR} and ω_{XUV} are the respective carrier frequencies. Finally, Δt is the time-step size of the propagation and $\Delta\tau$ is the time delay–step size of the time-delay scan.*

spectrum is shown in Fig. 5.5 (c). All important parameters used in this simulation are given in Tab. 5.1.

Figures 5.5 (a) and (c) exhibit the typical structures as they were explained by the DCM in Chap. 4. The 2s2p and sp_{23+} states exhibit a fast modulation indicating a resonant coupling. Furthermore, especially the 2s2p line shows hyperbolic structures, which is due to a strong modification of the state population, as well as a splitting of the line around the region of temporal overlap of XUV and NIR pulse. This splitting is the so-called Autler-Townes splitting, as a result of strong resonant coupling between the 2s2p and the spectroscopically dark 2p^2 state [125]. The energy splitting is basically the frequency representation of the well-known Rabi-oscillation that drives population between the coupled states. The time-delay dependence of this effect was theoretically investigated for a similar system by Wu *et al.* [126]. Although the detuning between the 2p^2 state and the 2s2p is 210 meV whereas the detuning between the 2p^2 and the sp_{23+} is only 100 meV, the coupling between the former states is apparently stronger. This is because the dipole transition matrix element d_{12} is almost a factor of 3 larger compared with the matrix element d_{23} of the other transition.

A fourth effect that is visible in the overview time-delay scan of the experimental data is the continuous modification of the resonance line shape among the highly excited states of sp_{24+} and above. Starting from an asymmetric Fano line shape the effect of the dressing NIR laser causes the line to become symmetric. This effect will be exploited in Chap. 6 in order to perform a precise *in situ* characterization of the applied few-cycle NIR

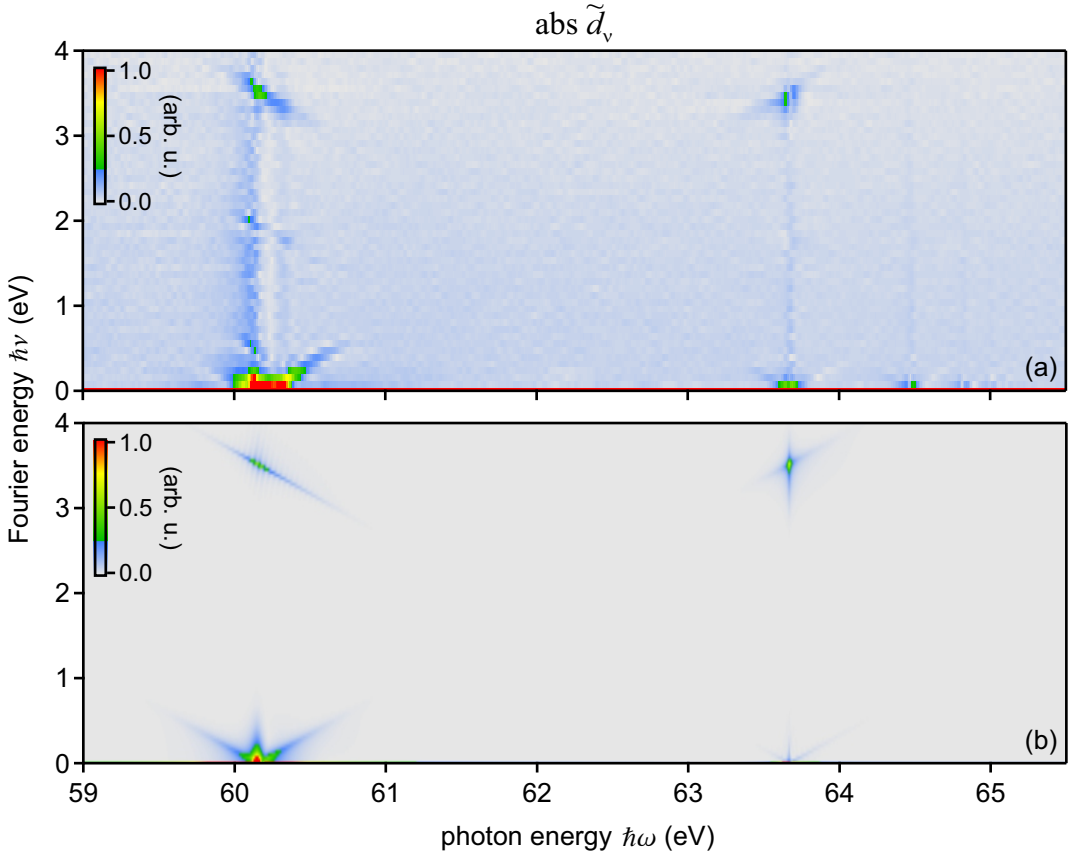

Fig. 5.6: *Two-dimensional spectral representation of Fig. 5.5 (a) and (c) in the Fourier energy range between 0 (DC) and 4 eV. The diagonal structures at Fourier energy $\hbar\nu \approx 3.5$ eV indicate two-photon coupling between the 2s2p and the sp_{23+} via the intermediate $2p^2$ state. This intermediate state is weakly populated in the excitation step of the experiment, which gives rise to the beat frequency of 1.9 eV due to coupling with the 2s2p state.*

pulses. Figure 5.5 (b) reveals explicitly the changes between the unperturbed (red line, $\tau = -15$ fs) and a strongly perturbed (black line, $\tau = 7.7$ fs) situation. The modification of the line shape of the highly excited states is clearly visible as well as the Autler-Townes splitting of the 2s2p line. The non-zero background absorption in between the resonances is due to the fact that these states lie energetically high above the first ionization threshold of helium. This means, they are embedded in a continuum of relatively constant optical density.

The time delay–dependent representation of Fig. 5.5 (a) and (c) are now complemented by the 2DAS representation of Fig. 5.6 (a) and (b). According to the time delay–step size of 171 as, the maximum of the ν-spectral range in the experiment yields 12.1 eV. The resolution $\delta\nu$ along the ν-axis is determined by the time-delay range (51 fs in the experiment shown) and reads 80 meV. The corresponding parameters for the simulated data are 20.7 eV for the maximum ν and 34 meV for the resolution.

By means of the 2DAS, the beat frequencies with which the 2s2p and sp_{23+} states are

modulated are directly revealed. The fast modulation in the experiment corresponds to a beating at 3.5 ± 0.1 eV equivalent to a period of only 1.2 fs. This matches the level spacing of the 2s2p and the sp_{23+} states, which is 3.51 eV according to the synchrotron data of Tab. 2.2, which closely resembles the beat frequency of 3.52 ± 0.04 eV obtained from the simulated 2DAS. Hence, the beating is due to a resonant two-NIR-photon coupling between those states. The $2p^2$ state at 62.04 eV serves as a resonant intermediate state, which both of the visible states couple to (see Fig. 4.2 (d)). This two-photon coupling process will be the main topic of a more detailed discussion in the next subsection. In addition to the fast beating – a so-called 2ω modulation referring to twice the laser frequency – the experimental 2DAS reveals also a weak 1ω modulation across the 2s2p state. This peak located at a Fourier frequency of $\hbar\nu = 2.0 \pm 0.1$ eV is the signature of a wave packet beating between the 2s2p and the spectroscopically dark sp^2 state whose energy difference is 1.91 eV. As discussed previously, the quantum path interference leading to the beating structure only occurs if both coupled states are coherently excited. Therefore, the 1ω beating indicates an NIR leakage, which leads to population of the $2p^2$ state via two-photon absorption (XUV+NIR) in the initial excitation step. Since, the NIR leakage was not taken into account in the three-level simulation, the 1ω-modulation is absent in the corresponding 2DAS. A 1ω modulation of the sp_{23+} is not observed in the experimental data. The reason for this is most probably the dipole matrix element between sp_{23+} and $2p^2$ being only one third of the dipole matrix element between 2s2p and $2p^2$. This combined with the generally lower absorption cross-section of the sp_{23+} state compared to the 2s2p might cause the 1ω feature not to rise above the noise level. Figure 5.6 (a) also shows that the highly excited states do not undergo resonant transitions to other states, which is important for the considerations in Chap. 6. All states shown exhibit peaks close to the DC limit, indicating slow variations of the absorption behavior. For the 2s2p state, a clear asymmetry of the diagonals is visible from the 2DAS, which corresponds to the asymmetry of the hyperbolic structures in the time-delay scan: they occur primarily on the right-hand-side of the absorption line. This cannot be explained by the prototype structure of non-resonant processes in the frame work of the DCM ($A = a_1 \exp(i\phi_1)$) nor by the numerical three-level simulation.

For the following investigation, the sp_{23+} doubly excited state shall serve as the state of interest and its resonant two-photon–mediated coupling to the 2s2p state is analyzed in detail by means of 2DAS.

5.2.1 Wave-packet beating on the sp_{23+} state in detail

The sp_{23+} doubly excited state of helium was chosen to demonstrate the 2DAS method for several reasons. First of all, the helium atom itself provides rich two-electron physics, while being at the same time the simplest few-body system one could think of. Second, the sp_{23+} state is subject to ultrafast population dynamics on the 1 fs time scale visible as the beating structure of the absorption signal (a detailed view of the time dependent spectrum as well as spectral lineouts of Fig. 5.5 is given in Fig. 5.7). Nevertheless, the underlying physics can mostly be understood in terms of a simple 3-level system (+ ground state) dressed by a strong NIR laser pulse, which will be numerically simulated

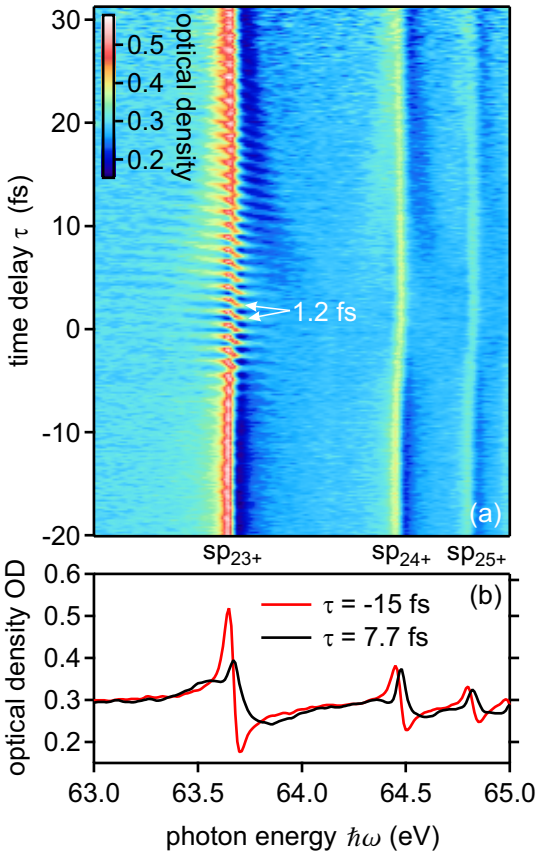

Fig. 5.7: *Detailed view of the time delay–dependent spectrum (a) and lineouts (b) of the sp_{23+} state and the neighboring sp_{24+} and sp_{25+} states. The data is identical to that in Fig. 5.5. The 1.2 fs (3.5 eV) wave packet beating that starts around the temporal pulse overlap of XUV and NIR is clearly resolved. The appearance of faint hyperbolic structures indicate the coupling to the initially unpopulated $2p^2$ state. The transform of the line shape of the higher lying states is also revealed. The intially asymmetric Fano line (q-parameter ≈ -2.6 [83]) is tranformed to a highly symmetric Lorentzian line shape (q-parameter $\gg 1$) in the vicinity of the pulse overlap. For greater time delays the effect gets weaker since the dressing laser then only affects a small residual part of the decaying state amplitude / dipole moment.*

and compared to the experimental data. And third, for the experimental conditions in the frame of this thesis, the sp_{23+} state (as well as the higher lying states) is ideal for comparison with the dipole control model. This is because the lifetime of this autoionizing state is > 80 fs, which is considerably longer than the 7 fs NIR pulses used rendering the Dirac-δ approximation of the pulse durations made in the DCM applicable.

Both the experimental and the three-level simulation data will be compared to an analytic DCM calculation for the resonant-interaction-type control parameter:

$$A(\tau) = 1 + a_2 e^{i\Delta\omega\tau + i\phi_2}. \tag{5.21}$$

By doing so, it shall be tested whether the quantum dynamics introduced by the strong NIR dressing laser can be described in terms of the analytic theory. As input parameters, the literature value $\hbar\Delta\omega = 3.51$ eV and a phase shift of $\phi_2 = \pi$ are chosen. The ν-resolution was chosen to be similar to the three-level case.

The results of a close-up look at the beat signal at ≈ 3.5 eV in the 2DAS representation depicted in Fig. 5.8. Using 2DAS, the information about the resonant coupling process leading to quantum interference is spectroscopically separated from other interaction pathways, which allows for a specific analysis. The peak in the magnitude plot reveals the beat frequency $\Delta\omega$ and thus the location of the coupling partner. As partly shown in the previous section, the results are

$$\Delta\omega_{\mathrm{sim}} = 3.52 \pm 0.04\,\mathrm{eV} \qquad \Delta\omega_{\mathrm{ex}} = 3.5 \pm 0.1\,\mathrm{eV} \qquad \Delta\omega_{\mathrm{DCM}} = 3.51 \pm 0.02\,\mathrm{eV} \tag{5.22}$$

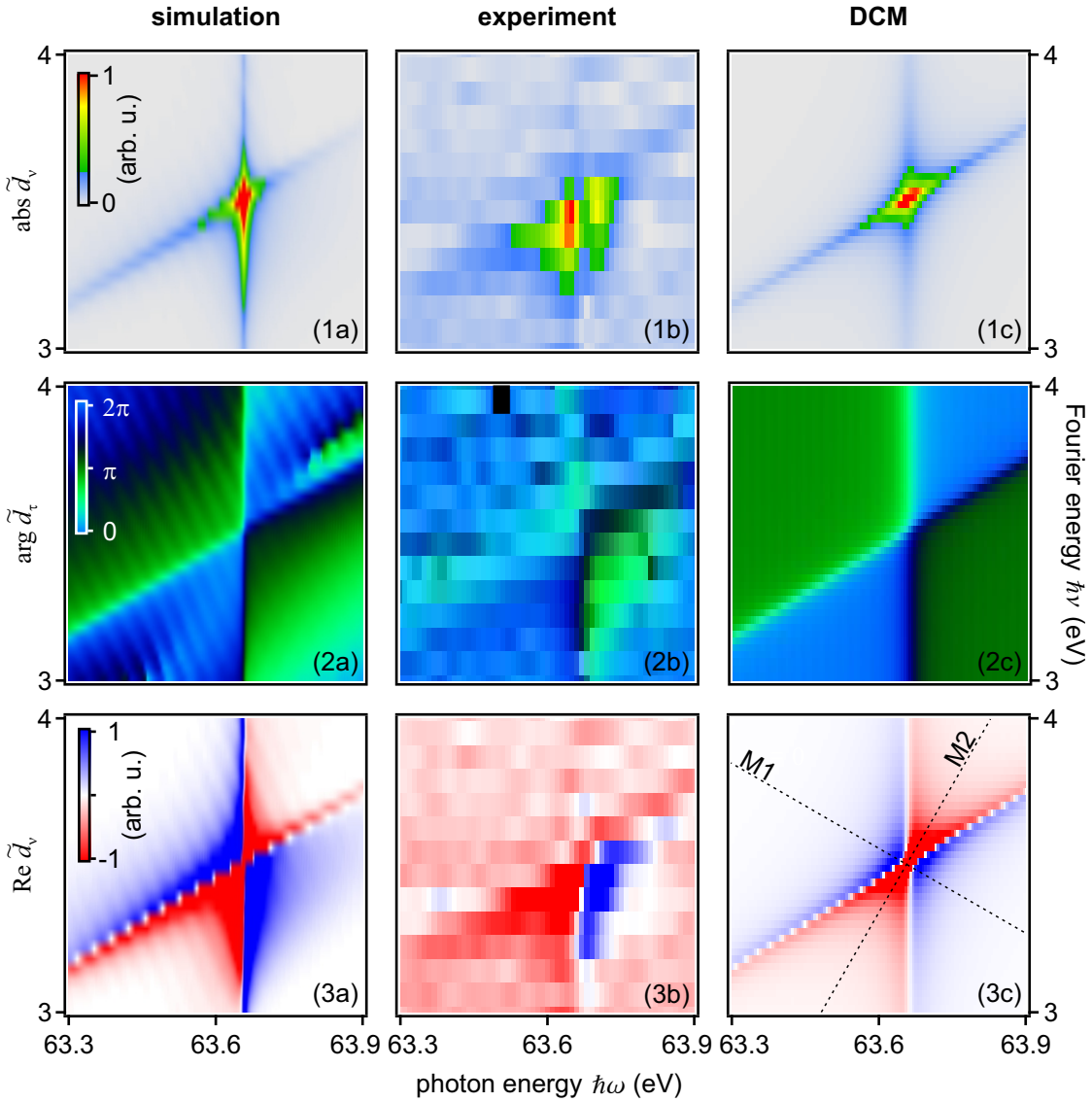

Fig. 5.8: *Detailed 2DAS representation of the beat signal on the sp_{23+} state corresponding to the quantum interference with the 2s2p state via two NIR photons and the $2p^2$ intermediate state. Rows 1, 2, and 3 show the magnitude, phase, and real part of the 2DAS, respectively. Columns a, b, and c designate the three-level simulation, experimental, and analytic DCM data. The respective color scales are normalized. The dashed lines in figure (3c) indicate the mirror axes M1 and M2 of the pattern.*

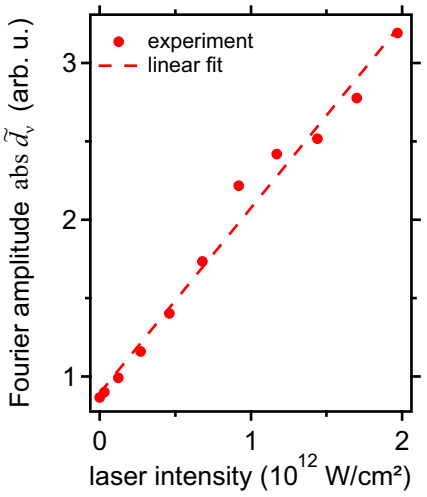

Fig. 5.9: *Integrated amplitude of the 2DAS magnitude peak that corresponds to the coupling of the 2s2p to the sp_{23+} state (Fig. 5.8 (1b)) plotted versus the NIR laser peak intensity. The dots correspond to the experimental data points whereas the dashed line resembles a linear fit of the data points, which corresponds to the theoretically expected behavior. The data points do not emerge from the origin due to finite background noise in the 2DAS.*

Compared to the reference value of $\Delta\omega_{\mathrm{ref}} = 3.51\,\mathrm{eV}$ [83] the deviation of these values is about 0.3% at most. The resolution values corresponding to the numerical and analytical calculation could be increased directly by an increased number of time-delay steps. In the experiments with the current setup this is only in principle possible. While the delay range of the piezo stage (Hera, Physical Instruments) driving the split-mirror unit exceeds 400 fs, driving a large time-delay range, e.g. more than 50 fs, is accompanied by a lateral shift of the beams (details in [87]). Thus, the two beams, NIR and XUV, are not imaged properly onto the same spot in the experimental cell. This problem could be solved by implementation of a tilt motion of the split-mirror to compensate for the lateral displacement of the foci.

Regarding the structure of the three 2DAS peaks, it is found to be similar but not identical. However, each peak exhibits a diagonal structure pointing towards the 2s2p state at $\nu = 0$. In general, the experimental peak in figure (1b) appears broader in both spectral directions compared to the simulated peaks. This is most likely because of the resolution of the XUV spectrometer (horizontal direction) and of the ν-axis (vertical direction).

Next, the laser intensity dependence of the coupling strength shall be studied. In order to do so, the integrated amplitude of the experimental 2DAS magnitude peak (Fig. 5.8 (1b)) is plotted versus the NIR laser intensity the target was exposed to. The result is summarized in Fig. 5.9. The figure shows that the amplitude of the 2DAS peak grows approximately linear with increasing laser intensity for moderate intensities. This observed linear relation is in agreement with the result obtained from perturbation theory. The dipole coupling term in the Hamiltonian is given by $W = -d\,E_{\mathrm{NIR}}$. Thus, the fraction $\Delta\psi_{12}$ of the wave function going from the 2s2p to the intermediate $2p^2$ state is proportional to $d_{12}\,E_{\mathrm{NIR}}$:

$$\Delta\psi_{12} \propto d_{12}\,E_{\mathrm{NIR}}. \tag{5.23}$$

Similar, the part coming from the $2p^2$ that is transferred to the final sp_{23+} state is proportional to $d_{23}\,E_{\mathrm{NIR}}$:

$$\Delta\psi_{23} \propto d_{23}\,E_{\mathrm{NIR}}. \tag{5.24}$$

Therefore, the part $\Delta\psi_{13}$ that undergoes the transition from the 2s2p to the sp_{23+} state is determined by

$$\Delta\psi_{13} \propto d_{12} E_{\mathrm{NIR}} \times d_{23} E_{\mathrm{NIR}} \propto d_{12} d_{23} I_{\mathrm{NIR}}. \tag{5.25}$$

In the context of the DCM, $\Delta\psi$ is identified with the parameter a_2. Hence, a linear dependence of a_2 on the laser intensity is understood and confirmed by the experimental data. The linear function has an offset with respect to the origin (0,0) due experimental noise leading to a background signal in the 2DAS. Nevertheless, even for low laser intensities the Fourier feature separates from the background, allowing for the detection of weak beat signals that could hardly be seen directly in the time-resolved representation.

The phase of the 2DAS depicted in Fig. 5.8 column 2 as well as the real part in column 3 are used to retrieve the phase jump ϕ_2 of the portion added to the sp_{23} wave function by resonant coupling to the 2s2p state. Besides the amplitude a_2 and the beat frequency $\Delta\omega$, ϕ_2 is the third degree of freedom for characterization of the light–matter interaction process within the limit of the DCM description of resonant coupling. By going to the resonance position (according to Eq. 5.22), the phase ϕ_2 can directly be obtained from the phase map via Eq. 5.14. Doing so yields

$$\phi_{2,\mathrm{sim}} = -3.04 \qquad \phi_{2,\mathrm{exp}} = -3.33 \qquad \phi_{2,\mathrm{DCM}} = -3.33 \tag{5.26}$$

These values are all relatively close to $-\pi \approx -3.14$ with a correction of $+0.1$ (4% deviation) for the three-level simulation and -0.19 (6% deviation) for the experimental data. The value of the DCM also deviates by 6% from $-\pi$, which is due to the decreased resolution. For a ν-resolution of 3 meV, the value of $-\pi$ is obtained with only 1% deviation. Intuitively, a value of $\phi_2 = -\pi$ is just what one would expect for this type of transition. Similar to classical mechanics where a pendulum driven resonantly by a periodic force exhibits a phase shift of $-\pi/2$ with respect to the driving motion, in quantum mechanics, a resonant transition between two states is accompanied by a phase shift of $-\pi/2$. This can be seen from Eq. 2.36: The part added to the wave function coefficient

$$-\lambda \frac{i}{\hbar} c_1^{(0)} e^{i\Delta\omega\tau} W_{21} \tag{5.27}$$

contains the phase factor $-i = \exp(-i\pi/2)$, which represents a constant phase shift of the coherently added part by $-\pi/2$ with respect to the existing part of the wave function (in addition to the τ-dependent phase shift). Since the experimental situation is a resonant two-photon process, the part of the 2s2p population that is moved to the sp_{23+} state acquires the phase shift of $-\pi/2$ twice: once in the transition from 2s2p to the intermediate $2p^2$ state, and once on the transition from the $2p^2$ to the sp_{23+} final state. Thus, the results of the direct phase retrieval are in good agreement with the theoretical considerations, which verifies the introduced method and its applicability to study ultrafast process of light–matter interaction.

As discussed in Sec. 5.1, the phase varies rapidly in the vicinity of the resonance peak. Therefore, directly reading the phase value from the phase map introduces high uncertainties, although the absolute value is determined accurately in the demonstrated cases.

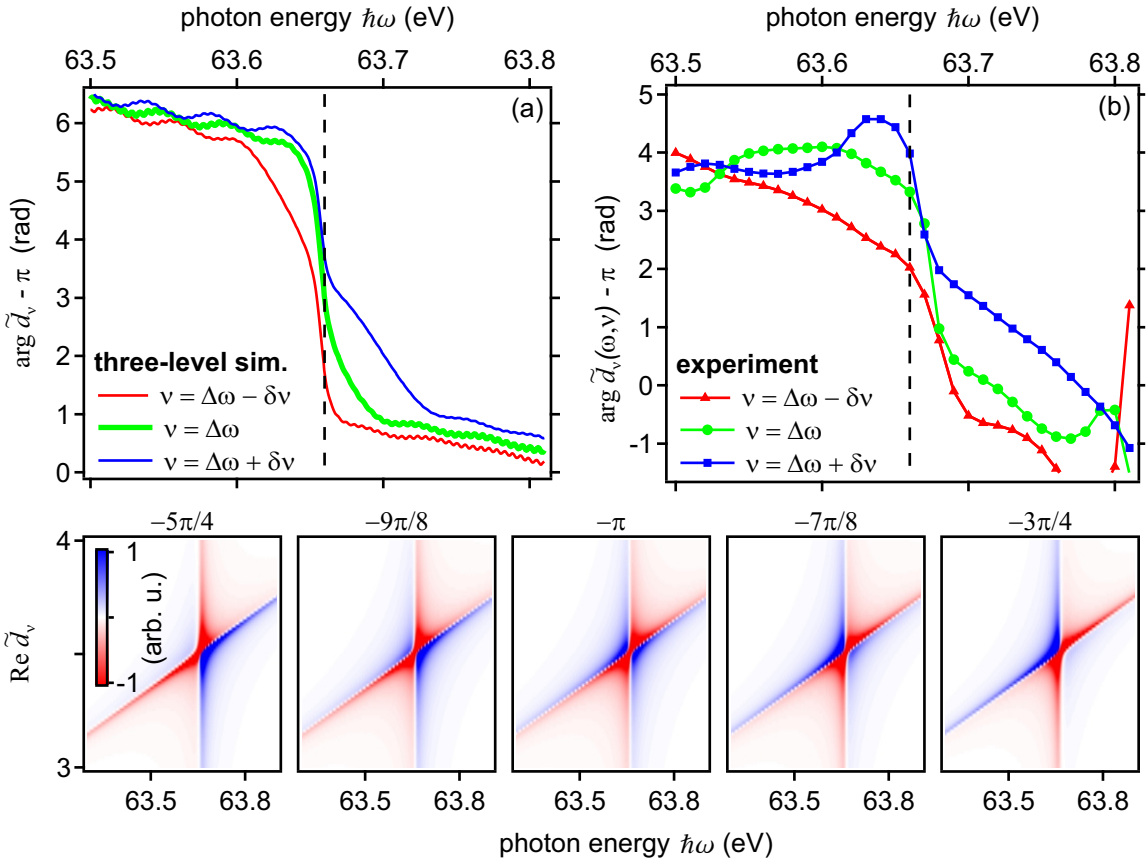

Fig. 5.10: *Lineouts of Fig. 5.8 (2a) and (2b) showing the 2DAS phase as a function of the photon energy for three different ν values around the resonance position obtained from the 2DAS magnitude in Fig. 5.8 (1a) and (1b). (a) shows the three-level simulation data and (b) shows the experimental data. The simulation data is drawn in solid lines because of the high resolution. The green curves correspond to the actual peak position along the ν-axis while the red and blue curves are displaced by $+$ and $-$ one ν-resolution unit $\delta\nu$, respectively. The dashed line indicates the resonance photon energy. (c) Comparison of the 2DAS real part patterns for five neighboring phase shifts ϕ_2 calculated by means of the DCM.*

Figure 5.10 shows the 2DAS phase in the vicinity of the 2DAS magnitude peak positions in Fig. 5.8 (1a) and (1b). The figure clearly indicates the rapid change of the phase around the resonance position. While the resolution in the photon energy dimension is sufficient to maintain a variation of the phase at the data points next to resonance of about ± 0.2 for the simulation and ± 0.5 for the experiment, the Fourier energy resolution puts more severe constraints to the uncertainty of the direct retrieval of ϕ_2. The phase at the photon energy resonance position $\omega = \omega_r$ on the curves displaced by $\pm\delta\nu$ differs by approximately $+0.7\,/\,-1.3$ from the resonance value in both simulation and experiment. Hence, despite that reading the phase at the resonance position yields values in good agreement with the theory, a second—more robust—method for phase retrieval is provided.

As demonstrated in Figs. 5.3 and 5.4 of the preceding section, the symmetry of the phase and real part pattern of the 2DAS is sensitive to ϕ_2. Figure 5.8 allows to compare the symmetry of the three-level simulation (2a, 3a) and the experimental data (2b, 3b) to that

of the analytic DCM calculation (2c, 3c) with given $\phi_2 = -\pi$ as input parameter. Both the real part and the phase map exhibit similar symmetry for all three cases. The three-level simulation and the DCM calculation agree qualitatively: the line perpendicular to the diagonal (M1) and the line bisecting the diagonal and the vertical (M2) as shown in Fig. 5.8 (3c) form mirror planes. The same pattern with minor deviations can be observed in Fig. 5.8 (3a). In contrast, a different phase shift leads to a different pattern as demonstrated in Fig. 5.10 (c). From this figure, it is obvious that a phase difference of $\pi/4 \approx 0.8$ can easily be resolved, whereas the changes in the pattern according to a phase difference of $\pi/8 \approx 0.4$ are more subtle. This finding indicates that the phase jump ϕ_2 recovered from the three-level simulation is approximately the same as for the DCM calculation, i.e. $\phi_2 = -\pi$, with an uncertainty of about $\pi/8$.
In the case of the experimental data, the agreement with the other two data sets is acceptable. In the lower right region of the map, the agreement is good. The real part makes a transition from positive (blue) to negative (red) values as the resonance photon energy is crossed. The red hourglass shaped region is also prominent in the lower left part. A transition to positive values indicated by a color change from red via white to blue, as observed in the simulations, is faint but visible. In the upper part of the graph, as also shown in the magnitude plot Fig. 5.8 (1b), the amplitude of the experimental 2DAS signal decreases quickly for ν-values above the resonance position. Thus the pattern cannot be directly compared to the simulated ones in that region. In the lower region, the broken symmetry with respect to the M2 mirror plane makes the pattern resemble the $\phi_2 = -9\pi/8 \approx -3.53$ pattern of Fig. 5.10 (c) rather than the perfectly symmetric $\phi_2 = -\pi = -3.14$ pattern. This is in agreement with the directly retrieved value $\phi_{2,\mathrm{exp}} = -3.33$ being in between these two values. Also here the uncertainty is estimated to be $\pi/8$.

In general, the retrieved phases agree well with the theoretically expected value within the uncertainty limits. There are two main points that could lead to the found deviations. First, the theoretical value was estimated by a simple consideration, not taking into account the slight detuning of the laser carrier frequency with respect to the transition energies. Second, the phase ϕ_2 and its appearance in the 2DAS where derived in the perturbative limit of the DCM. The relatively intense laser field of 2×10^{12} W/cm^2 starts to introduce non-perturbative effects, e.g. Autler-Townes splitting as seen in Fig. 5.5, so that the perturbative treatment could introduce an error. Nevertheless, this proof-of-principle experiment and calculation demonstrate that 2DAS is capable of extracting phase and amplitude information on ultrafast light–matter interaction processes.

5.3 2DAS of a spin–orbit wave packet in inner-valence–excited xenon

In this section the concept of 2DAS is applied in a second study in order to observe the signatures of a spin–orbit wave packet that is created by inner-valence excitation of xenon by XUV light and probed by strong-field ionization caused by intense NIR laser pulses.

First, the level structure of xenon is outlined and the creation of the wave packet by means of XUV light is discussed. The main focus lies on the observation of this wave packet, which is possible via strong-field ionization as shall be discussed using a simplified analytic and a numeric calculation. Finally the experimental data is analyzed by means of 2DAS.

5.3.1 Creation of a spin–orbit wave packet

The electronic ground-state configuration of xenon is $[\mathrm{Kr}]4\mathrm{d}^{10}5\mathrm{s}^2 5\mathrm{p}^6$. The first four ionization energies of xenon are (Ref. [80])

$$I_\mathrm{P}^1 = 12.1\,\mathrm{eV} \qquad I_\mathrm{P}^2 = 21.0\,\mathrm{eV}$$
$$I_\mathrm{P}^3 = 31.1\,\mathrm{eV} \qquad I_\mathrm{P}^4 = 42.2\,\mathrm{eV},$$

which means that at photon energies around 66 eV the system is highly excited. There are two Rydberg series in this energy regime, which both arise from excitation of one 4d-shell electron into np states with $n \geq 6$ (the lower p shells are completely filled). The electron configuration $[\mathrm{Kr}]4\mathrm{d}^9 5\mathrm{s}^2 5\mathrm{p}^6$ has D-symmetry character so that the orbital angular momentum $l = 2$ and the spin of the electron $s = 1/2$ that is not compensated for by the other 8 electrons—one could also speak of a hole—give rise to spin–orbit coupling. The two possible configurations, which can by accessed by XUV light, are [127]:

$$[\mathrm{Kr}]4\mathrm{d}^9 5\mathrm{s}^2 5\mathrm{p}^6 \left(^2D_{3/2}\right) n\mathrm{p} \qquad \text{and} \qquad [\mathrm{Kr}]4\mathrm{d}^9 5\mathrm{s}^2 5\mathrm{p}^6 \left(^2D_{5/2}\right) n\mathrm{p}.$$

The excited electron in the np shell ($l = 1$) has a total angular momentum of either $j = 1/2$ in the $\mathrm{D}_{3/2}$ configuration or $j = 3/2$ in the $\mathrm{D}_{5/2}$ configuration of the inner shells, so that in total, the dipole selection rule $\Delta l = 1$ for absorption of a photon is fulfilled. An overview absorption spectrum is depicted in Fig. 5.11 where the states up to $n = 8$ are labeled for each Rydberg series. Owing to the heavy xenon atom, the splitting of the two $n = 6$ states, which the focus is put on in the following, is relatively strong and amounts to 1.93 eV [127]. As both states are coherently populated by the XUV light, they are expected to form a coherent quantum-mechanical wave packet. The beat frequency is given by the energy splitting and is equivalent to a period of 2.1 fs. Due to the highly non-equilibrium nature of these states, their lifetime is only about 5 fs and thus comparable or even shorter than the few-cycle NIR pulses used in these experiments (7 fs FWHM duration). Hence, more care needs to be taken when comparing the experimental data to theory that assumes Dirac-δ light pulses.

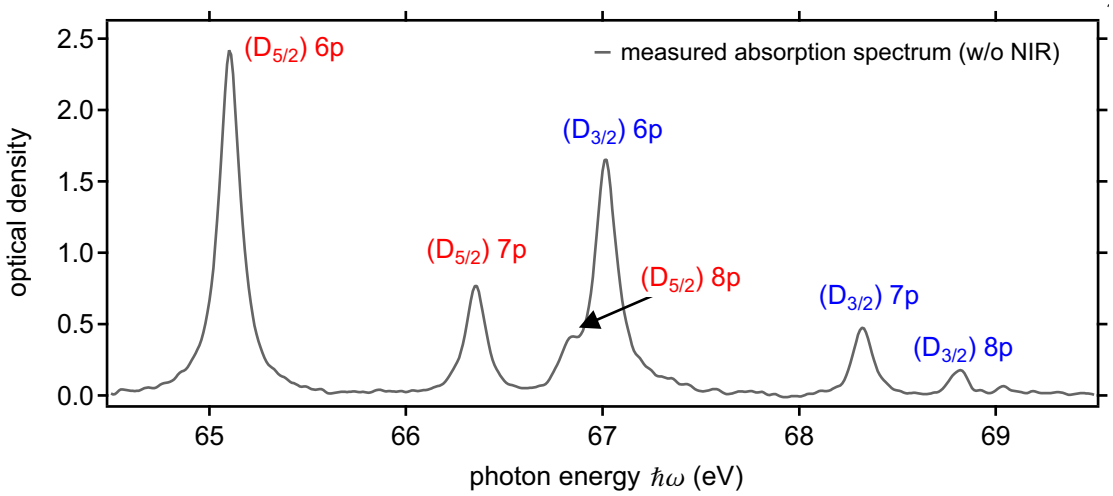

Fig. 5.11: *Overview spectra of the 4d-shell-excited xenon levels around 67 eV. There are two spin-orbit-split Rydberg series: $D_{3/2}$ sub-symmetry (blue) and $D_{5/2}$ sub-symmetry (red).*

Compared with the situation of the preceding section on doubly excited helium, the problem of detecting a signature of the wave packet is different in the case of 4d-excited xenon. In the case of helium, the transfer of population from one state to the other via resonant two-photon coupling, leads to a periodic modulation of the optical density as a result of quantum path interference as the signature of the wave packet (see Sec. 5.2). In xenon, since the spacing of the two states is only 1.92 eV, it is not possible to transfer population from one state to the other via a two-photon transition (a one-photon transition is dipole forbidden), as this would require sufficient intensity at 1290 nm, which greatly exceeds the achievable bandwidth reaching approximately 950 nm on the long-wavelength side. Thus, a different mechanism is needed in order to probe the wave packet. The idea proposed here is to use the effect of strong-field ionization of the excited 6p electron to generate a signature of the wave packet. This will be the topic of the following sections.

5.3.2 Observation of the wave packet via strong-field ionization

Since conventional two-photon coupling of the $\left(D_{5/2}\right)6p$ and the $\left(D_{3/2}\right)6p$ state is experimentally not possible with the existing setup, an alternative approach is investigated experimentally and theoretically. It is known from ADK theory (see Sec. 2.1.3) that in a strong laser field the tunneling probability depends on the magnetic quantum number m_l—or in other words—on the alignment of the orbital with respect to the laser polarization axis. The excited electron has an angular momentum quantum number of $l = 1$, so that the ratio between the probability for tunneling out of the $m_l = 0$ orbital to that for tunneling out of the $m_l = 1$ orbital is according to Eq. 2.16 given by

$$\frac{w_{\mathrm{i},m_l=0}}{w_{\mathrm{i},m_l=1}} = 2\frac{(2I_\mathrm{P})^{3/2}}{|E(t)|}. \tag{5.28}$$

To give a rough estimate, this value is approximately 10 at the peak of the laser pulse (intensity 10^{13} W/cm^2, $I_\mathrm{P} = 2.5$ eV). Therefore, after the ionization event, the population

in the $m = 0$ state is almost negligible compared with the population remaining in the $|m_l| = 1$ state. This means that strong-field ionization is strongly selective concerning the magnetic quantum numbers of the uncoupled l states. In the total angular momentum basis, which is the Eigensystem of the excited xenon atom because spin–orbit coupling is present, the states are labeled by the total angular momentum j and its magnetic quantum number m_j. Nevertheless, the $\left|j,m_j\right\rangle$ Eigenstates of the system can be decomposed into linear combinations of the $|l,m_l\rangle$ states. These $|l,m_l\rangle$ states of the uncoupled basis enter in both the $\left(\mathrm{D}_{5/2}\right)$6p and the $\left(\mathrm{D}_{3/2}\right)$6p Eigenstates. Now, by means of strong-field ionization, both states of the proposed wave packet are basically projected onto the same $|m_l| = 1$ state. This leads to quantum interference, which can be detected by virtue of the absorption signal. The whole process is illustrated by an analytic quantum-mechanical model assuming Dirac-δ pulses.

Analytic explanation

In order to demonstrate the quantum path interference that leads to a beat signal in the absorption spectrum as a fingerprint of the spin–orbit wave packet, a simple analytical model is developed. The focus is placed on the excited 6p electron, which can be removed from the atom via strong-field ionization by the NIR pulse. The total angular momentum can be $j = 3/2$ or $j = 1/2$ as explained before. The magnetic quantum numbers, thus, are restricted $m_j = \pm 3/2, \pm 1/2$ and $m_j = \pm 1/2$, respectively. The $m_j = \pm 3/2$ does not couple to the other states since it is solely represented by the state of $m_l = \pm 1$ and $m_s = \pm 1/2$. Therefore, these states are not considered in the calculation. In the following the states are labeled as

$$\begin{aligned} \text{spin-orbit-coupled basis:} \quad & \left|j,m_j\right\rangle_j \\ \text{uncoupled basis:} \quad & |m_l,m_s\rangle_l\,. \end{aligned}$$

According to this definition

$$\left|\frac{3}{2},\pm\frac{3}{2}\right\rangle_j = \left|\pm 1,\pm\frac{1}{2}\right\rangle_l \tag{5.29}$$

The other states in the two bases are related via the Clebsch–Gordan coefficients:

$$\left|\frac{3}{2},\frac{1}{2}\right\rangle_j = \frac{1}{\sqrt{3}}\left|1,-\frac{1}{2}\right\rangle_l + \frac{\sqrt{2}}{\sqrt{3}}\left|0,\frac{1}{2}\right\rangle_l \tag{5.30}$$

$$\left|\frac{1}{2},\frac{1}{2}\right\rangle_j = \frac{\sqrt{2}}{\sqrt{3}}\left|1,-\frac{1}{2}\right\rangle_l - \frac{1}{\sqrt{3}}\left|0,\frac{1}{2}\right\rangle_l \tag{5.31}$$

$$\left|1,-\frac{1}{2}\right\rangle_l = \frac{1}{\sqrt{3}}\left|\frac{3}{2},\frac{1}{2}\right\rangle_j + \frac{\sqrt{2}}{\sqrt{3}}\left|\frac{1}{2},\frac{1}{2}\right\rangle_j \tag{5.32}$$

$$\left|0,\frac{1}{2}\right\rangle_l = \frac{\sqrt{2}}{\sqrt{3}}\left|\frac{3}{2},\frac{1}{2}\right\rangle_j - \frac{1}{\sqrt{3}}\left|\frac{1}{2},\frac{1}{2}\right\rangle_j \tag{5.33}$$

The negative m_j involve the $m_l = -1$ state, and thus, do not couple to the positive m_j states. Apart from that the calculations for negative m_j are completely analogous, which

is why only the positive m_j-values are considered in the following. In conclusion, the considerations are restricted to the $\left|\frac{3}{2},\frac{1}{2}\right\rangle_j$ and the $\left|\frac{1}{2},\frac{1}{2}\right\rangle_j$ state.
In the excitation step at $t=0$, the wave packet is created by means of the XUV pulse, which is treated as a Dirac-δ function. Thereby, the wave function can be written as the coherent superposition of the two considered Eigenstates:

$$|\psi(t=0)\rangle = a\left|\frac{3}{2},\frac{1}{2}\right\rangle_j + b\left|\frac{1}{2},\frac{1}{2}\right\rangle_j \tag{5.34}$$

where a and b are the coefficients, which can be obtained from the absorption cross-section [127]. The field-free time evolution of this wave packet is obtained by multiplication of the states with their respective phase term:

$$|\psi(t)\rangle = a\left|\frac{3}{2},\frac{1}{2}\right\rangle_j e^{-i\omega_{3/2}t} + b\left|\frac{1}{2},\frac{1}{2}\right\rangle_j e^{-i\omega_{1/2}t} \tag{5.35}$$

where $\hbar\omega_{3/2} = 65.11\,\text{eV}$ is the energy of the $\left|\frac{3}{2},\frac{1}{2}\right\rangle_j$ state and $\hbar\omega_{1/2} = 67.04\,\text{eV}$ is the energy of the $\left|\frac{1}{2},\frac{1}{2}\right\rangle_j$ state. By means of Eqs. 5.30 and 5.31, the wave function is equivalently represented in the l,m_l basis:

$$|\psi(t)\rangle = a\left[\frac{1}{\sqrt{3}}\left|1,-\frac{1}{2}\right\rangle_l + \frac{\sqrt{2}}{\sqrt{3}}\left|0,\frac{1}{2}\right\rangle_l\right]e^{-i\omega_{3/2}t} + b\left[\frac{\sqrt{2}}{\sqrt{3}}\left|1,-\frac{1}{2}\right\rangle_l - \frac{1}{\sqrt{3}}\left|0,\frac{1}{2}\right\rangle_l\right]e^{-i\omega_{1/2}t}. \tag{5.36}$$

Reordering of the terms yields:

$$|\psi(t)\rangle = \left[\frac{a}{\sqrt{3}}e^{i\Delta\omega t} + \frac{b\sqrt{2}}{\sqrt{3}}\right]e^{-i\omega_{1/2}t}\left|1,-\frac{1}{2}\right\rangle_l + \left[\frac{a\sqrt{2}}{\sqrt{3}}e^{i\Delta\omega t} - \frac{b}{\sqrt{3}}\right]e^{-i\omega_{1/2}t}\left|0,\frac{1}{2}\right\rangle_l \tag{5.37}$$

where $\Delta\omega = \omega_{1/2} - \omega_{3/2}$ is the difference frequency of the states. Equation 5.37 implies that the population in the l,m_l basis states is not constant but oscillates in time, which is because they are not Eigenstates of the excited xenon atom. The oscillation period is given by $2\pi/\Delta\omega$.
To keep the description simple, the strong-field ionization by the NIR pulse is approximated as an instantaneous event where all population of the $\left|0,\frac{1}{2}\right\rangle_l$ is removed and the $\left|1,-\frac{1}{2}\right\rangle_l$ state is not affected. The main differences of this simplified treatment compared with reality are that in the experiment the ionization occurs periodically at every crest of the NIR electric field, and that the ionization is not complete—just the ionization rate of the $\left|1,-\frac{1}{2}\right\rangle_l$ and the $\left|0,\frac{1}{2}\right\rangle_l$ state differ significantly. This has important consequences on the success of probing the wave packet as will be discussed later. Nevertheless, the main mechanism is already captured by this crude approximation.
The ionization takes place at time $t=\tau$ after the excitation, so that directly afterwards the wave function reads:

$$|\psi(t=\tau)\rangle = \left[\frac{a}{\sqrt{3}}e^{i\Delta\omega\tau} + \frac{b\sqrt{2}}{\sqrt{3}}\right]e^{-i\omega_{1/2}\tau}\left|1,-\frac{1}{2}\right\rangle_l \tag{5.38}$$

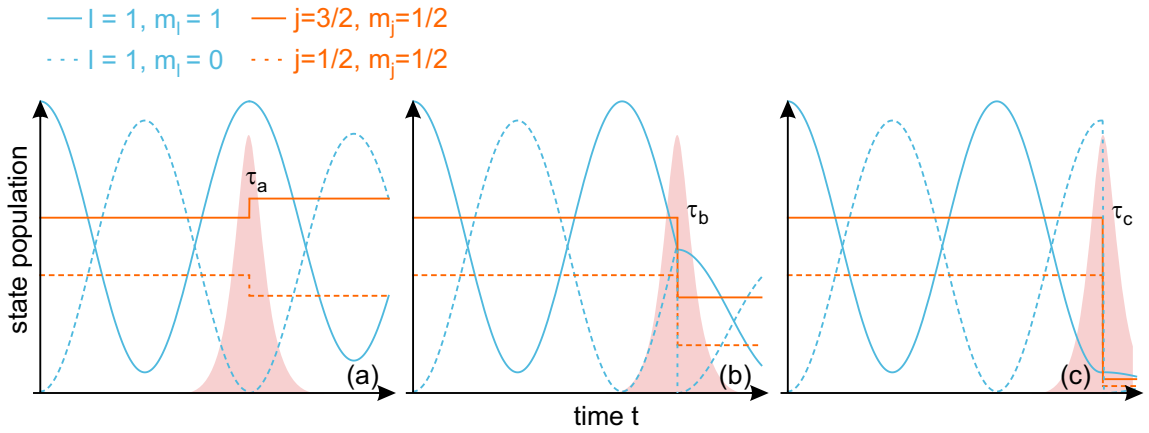

Fig. 5.12: *Population dynamics in the two bases (l,m_l) (blue) and (j,m_j) (orange), where the excitation event takes place at the origin of the graph and the ionization event occurs at the respective time delay τ_a, τ_b, and τ_c. The effect of the ionization on the remaining population depends on the time delay and is periodic.*

This defines how much population has survived the ionization event: If most of the population was in $\left|0,\frac{1}{2}\right\rangle_l$ at time τ, almost no population would remain bound since $\left|0,\frac{1}{2}\right\rangle_l$ is completely depopulated. On the other hand, if most of the population was in $\left|1,-\frac{1}{2}\right\rangle_l$, the ionization would barely affect the system since $\left|0,\frac{1}{2}\right\rangle_l$ is only weakly ionized. Equation 5.38 forms the starting point of again a field free propagation period. Since, $\left|1,-\frac{1}{2}\right\rangle_l$ is not an Eigenstate, the temporal evolution is of $|\psi(t>\tau)\rangle$ is obtained by going back to the j,m_j representation via Eqs. 5.32

$$|\psi(t=\tau)\rangle = \left[\frac{a}{\sqrt{3}}e^{i\Delta\omega\tau}+\frac{b\sqrt{2}}{\sqrt{3}}\right]e^{-i\omega_{1/2}\tau}\left[\frac{1}{\sqrt{3}}\left|\frac{3}{2},\frac{1}{2}\right\rangle_j+\frac{\sqrt{2}}{\sqrt{3}}\left|\frac{1}{2},\frac{1}{2}\right\rangle_j\right] \tag{5.39}$$

and incorporating the phase evolution:

$$|\psi(t>\tau)\rangle = \left[\frac{a}{\sqrt{3}}e^{i\Delta\omega\tau}+\frac{b\sqrt{2}}{\sqrt{3}}\right]e^{-i\omega_{1/2}\tau}\left[\frac{1}{\sqrt{3}}e^{-i\omega_{3/2}(t-\tau)}\left|\frac{3}{2},\frac{1}{2}\right\rangle_j+\frac{\sqrt{2}}{\sqrt{3}}e^{-i\omega_{1/2}(t-\tau)}\left|\frac{1}{2},\frac{1}{2}\right\rangle_j\right] \tag{5.40}$$

After algebraic modifications the wave function becomes

$$|\psi(t>\tau)\rangle = \frac{\sqrt{2}}{3}\left\{\left[\frac{a}{\sqrt{2}}e^{i\Delta\omega\tau}+b\right]e^{-i\omega_{3/2}t}\left|\frac{3}{2},\frac{1}{2}\right\rangle_j+\left[a+\sqrt{2}e^{-i\Delta\omega\tau}b\right]e^{-i\omega_{1/2}t}\left|\frac{1}{2},\frac{1}{2}\right\rangle_j\right\} \tag{5.41}$$

The temporal evolution of the individual state populations is shown exemplarily in Fig. 5.12 for three different time delays τ_a - τ_c between excitation by the XUV and ionization by the NIR pulse. The initial population in the Eigenstates is distributed as 2/5 on the $\left|\frac{1}{2},\frac{1}{2}\right\rangle_j$ and 3/5 on the $\left|\frac{3}{2},\frac{1}{2}\right\rangle_j$ state. This distribution is stationary, while the population of in the two – $\left|1,-\frac{1}{2}\right\rangle_l$ and $\left|0,\frac{1}{2}\right\rangle_l$ – states oscillates back and forth (Eq. 5.37). At the ionization event, the whole wave function is projected onto the $\left|1,-\frac{1}{2}\right\rangle_l$

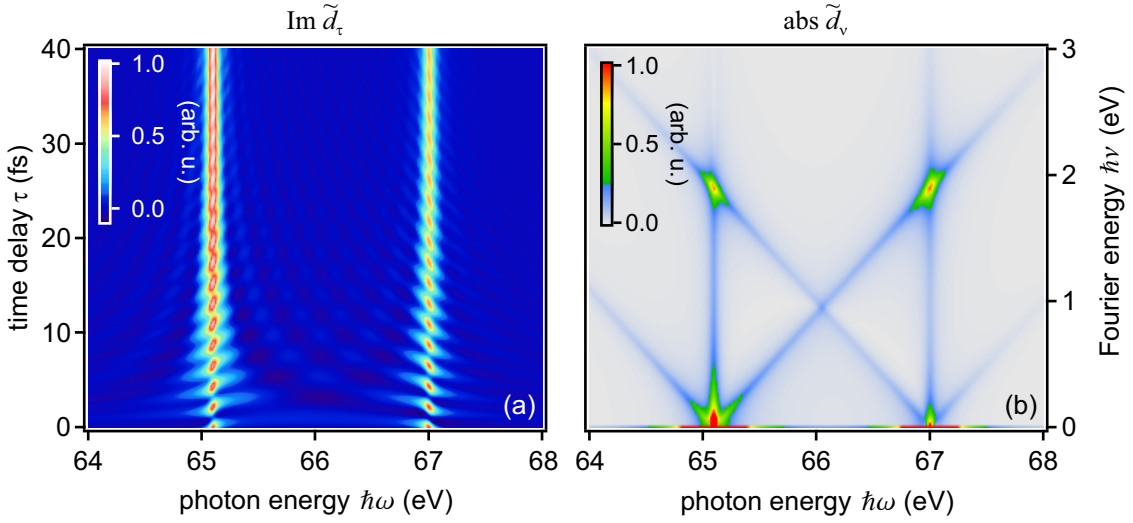

Fig. 5.13: *Time resolved absorption spectrum (a) and 2DAS (b) of the spin-orbit wave packet in inner-valence-excited xenon according to the analytical theory presented.*

state because of complete ionization of the $\left|0,\frac{1}{2}\right\rangle_l$ state. In Fig. 5.12 (a), this occurs when the population in $\left|0,\frac{1}{2}\right\rangle_l$ is minimized leading to basically only a redistribution of the population in the coupled basis (the relation 3/5 to 2/5 becomes 2/3 to 1/3). Compared with (a), Figs. (b) and (c) exhibit a stronger manipulation of the population. In Fig. (c), the population is almost completely removed from the states because the ionization occurs just when almost all population resides in the preferably ionized $\left|0,\frac{1}{2}\right\rangle_l$ state. The whole process is periodic in τ, which gives rise to a characteristic beat signal in the time delay–resolved absorption spectrum. The absorption spectrum can be obtained from the wave function, directly by calculating the imaginary part of the spectrum of the dipole expectation value $d(t) = \langle\psi(t)|\hat{d}|\psi(t)\rangle$. Figure 5.13 shows the resulting time-delay scan (a) and the corresponding 2DAS (b). The initial population was chosen to be the same as in Fig. 5.12. The beating is clearly visible in the time-delay scan and manifests itself as the two characteristic 2DAS peaks at 1.92 eV Fourier energy. Since the population, and thus the absorption cross-section, of the two states is strongly modified during the strong-field ionization event, also diagonals above the DC limit arise.

As stated previously, in the experiment with few-cycle NIR laser pulses, incomplete strong-field ionization occurs at every crest of the laser pulse electric field. For the experiments done within the frame of this thesis, the pulse duration is approximately 7 fs (FWHM), corresponding to six half-cycles, and the photon energy is 1.7 eV. This corresponds to an ionization period of 1.2 fs. Thus, the multiple probing steps of the spin–orbit wave packet are not in phase with the wave packet's beat. The consequence of this is that the contributions from the different half-cycles do not add up coherently, so that the strength of modulation is strongly decreased compared with the analytic case of a single ionization event. For shorter pulses in the single-cycle regime or a resonant photon energy ($\hbar\omega = 1/2\Delta\omega \approx 0.96\,\text{eV}$), the loss of coherence can be reduced significantly. To simulate this effect, a non-perturbative two-level simulation was performed. In each time step, the basis is changed from (j,m_j) to (l,m_l) where the ionization is treated via the

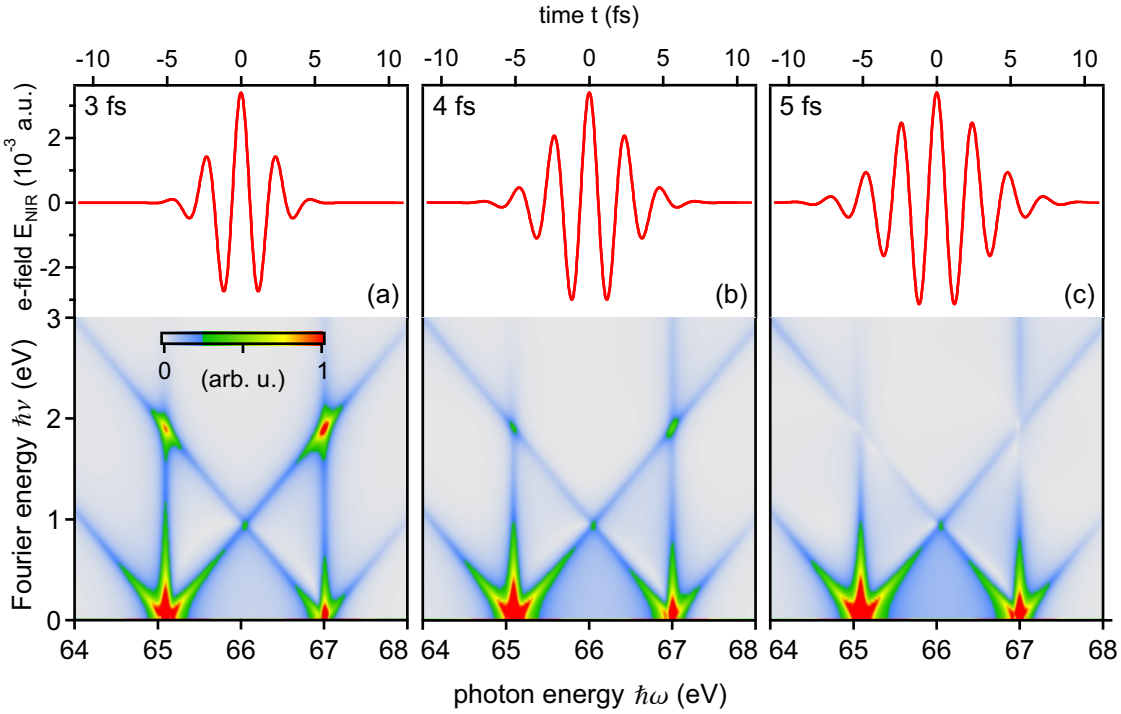

Fig. 5.14: *Loss of wave packet signature due to finite laser pulse duration at non-resonant wavelength. Simulated 2DAS spectra and corresponding wave forms of the NIR laser pulse used to simulate strong-field ionization by means of ADK theory. (a) In the single-cycle regime (3 fs FWHM) the dominant half-cycle almost exclusively leads to ionization, which preserves the coherence in the final state. (b) Considerable reduction of the wave packet signal in the 2DAS at 4 fs FWHM duration. (c) Almost complete loss of information about the spin-orbit wave packet for a 5 fs pulse.*

ADK formula (Eq. 2.16) with the respective m_l-values of the two states. Afterwards, the basis transformation is reversed and the system is propagated in the (j, m_j) basis assuming no further effects of the NIR laser except ionization. The resulting 2DAS are plotted in Fig. 5.14 for three different laser pulse durations in the one- to two-cycle regime at 730 nm carrier wavelength. As expected intuitively, the signature 2DAS peak at $\hbar\Delta\omega = 1.92\,\mathrm{eV}$ vanishes rapidly for increasing laser pulse duration. In order to obtain a clear signature of the wave-packet beating, the simulations suggest an FWHM pulse duration on the order of 4 fs, which corresponds to 1.5 optical cycles. This makes the experimental observation of this wave packet challenging since generating and maintaining such short pulse durations is a sophisticated task.

These considerations are in agreement with a recent study by Pabst and Wörner where the coherence of the $5p_{1/2}^{-1}$ and $5p_{3/2}^{-1}$ hole states in xenon prepared by strong-field ionization was theoretically investigated [128]. The authors demonstrate that for laser wavelengths ω_c that are not resonant with the multiples of twice the wave packet wavelength ($\lambda_{wp} = 2\pi c/\Delta\omega$) the coherence of the created wave packet is reduced significantly if the laser pulse exceeds the 1.5 cycle regime. The effect is especially strong if the laser period

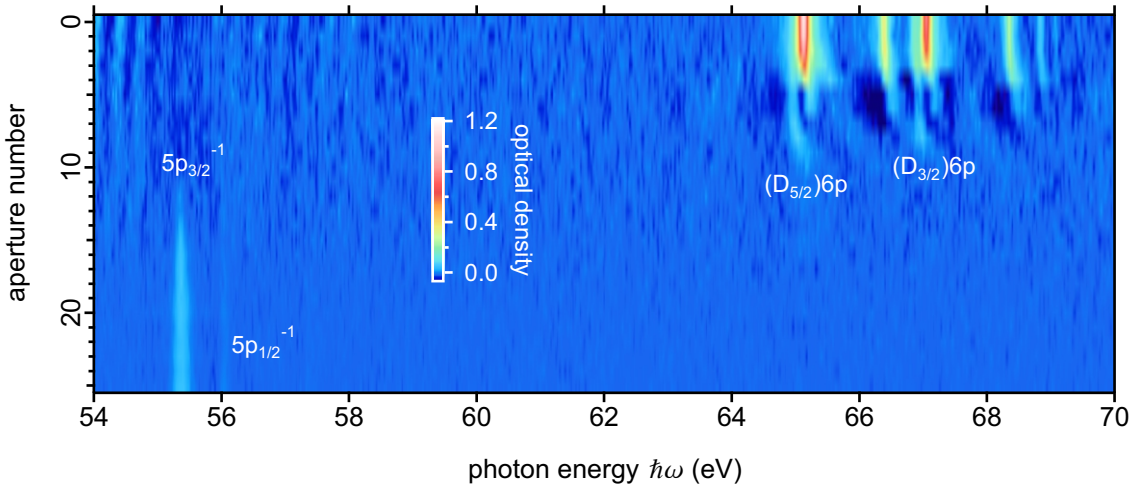

Fig. 5.15: *Absorption spectrum as a function of the aperture opening to demonstrate the strong-field ionization capability of the NIR pulses. For aperture position 0, the effect of the NIR is negligible. The inner-shell-excited series above 65 eV starts to vanish quickly due to strong-field ionization. Around position 10 the signatures are completely gone. Instead absorption lines of strong-field generated xenon cation states arise, which proves the applicable intensities to be sufficient for strong-field ionization.*

is close to the wave-packet period, which is the case for the system considered here:

$$\begin{aligned} 1\times\lambda_{\mathrm{wp}} \quad &< \lambda_{\mathrm{c}} \ll \quad 2\times\lambda_{\mathrm{wp}} \\ 645\,\mathrm{nm} \quad &< 730\,\mathrm{nm} \ll \quad 1290\,\mathrm{nm} \end{aligned}$$

In the following, despite the discouraging theoretical predictions, a first experimental attempt in order to observe the wave-packet dynamics in xenon with a laser pulse duration of approximately 7 fs FWHM is presented and discussed with the knowledge of the preceding section.

Experimental indications

The two prerequisites for the observation of the wave-packet signal are excitation of the inner-shell–excited states by XUV light, and strong-field ionization of the excited xenon states by the NIR pulse. The former is demonstrated by Fig. 5.11. Thus, only the possibility and signatures of strong-field ionization need to be investigated first. Figure 5.15 shows a stationary spectrum at 7 fs time delay between XUV and NIR pulse for varying NIR intensity labeled by the aperture number (increasing number corresponds to wider aperture). From this figure, it becomes obvious that the NIR laser can be operated at sufficient intensities to completely extinguish the signatures of the $\left(\mathrm{D}_{5/2}\right)n\mathrm{p}$ and $\left(\mathrm{D}_{3/2}\right)n\mathrm{p}$ series. The aperture opening in the depicted scan is varied coarsely to provide a high intensity range. For the actual experiment, the region around position 4 is studied precisely. At higher intensity, the signal vanishes so that observation of the wave-packet beating is not possible. Interestingly, for high intensities, i.e. starting around position 10, strong-field ionization of ground state xenon begins, which is revealed by the absorption lines between 55 and 56 eV. These lines correspond to XUV absorption by the strong-field

generated cation states:

$$[\mathrm{Kr}]4\mathrm{d}^{10}5\mathrm{s}^2 5\mathrm{p}^6\ \mathrm{S}_0 \xrightarrow{\mathrm{NIR}} [\mathrm{Kr}]4\mathrm{d}^{10}5\mathrm{s}^2 5\mathrm{p}^5\ \mathrm{P}_{3/2} \xrightarrow{\mathrm{XUV}} [\mathrm{Kr}]4\mathrm{d}^{9}5\mathrm{s}^2 5\mathrm{p}^6\ \mathrm{D}_{5/2}$$
$$[\mathrm{Kr}]4\mathrm{d}^{10}5\mathrm{s}^2 5\mathrm{p}^6\ \mathrm{S}_0 \xrightarrow{\mathrm{NIR}} [\mathrm{Kr}]4\mathrm{d}^{10}5\mathrm{s}^2 5\mathrm{p}^5\ \mathrm{P}_{1/2} \xrightarrow{\mathrm{XUV}} [\mathrm{Kr}]4\mathrm{d}^{9}5\mathrm{s}^2 5\mathrm{p}^6\ \mathrm{D}_{3/2}.$$

These are the states studied in Ref. [128] and experimentally observed by means of XUV transient absorption spectroscopy in Ref. [38]. The appearance of these states in the absorption spectrum demonstrates that the laser pulses can even strong-field ionize neutral xenon with an ionization potential of 12.1 eV.

In order to investigate the possible spin–orbit wave-packet signature, a fine scan of the laser-pulse intensity around the onset of strong-field ionization is performed, and for each intensity, a time delay–resolved spectrum is recorded. Since the beat signal of the spin–orbit wave packet is supposed to be very faint, the 2DAS method is applied in order to extract the information from the time-resolved spectrum where a multitude of frequency components contributes to the spectral pattern (see Fig. 5.4 as a demonstration). Figure 5.16 features the time delay–resolved as well as the 2DAS representation of three sets of experimental data of the intensity scan. The NIR intensity is increasing from the top to the bottom figures. The two strong absorption lines at 65.1 and 67.0 eV correspond to the transitions from the ground state to the $\left(\mathrm{D}_{5/2}\right)6\mathrm{p}$ and to $\left(\mathrm{D}_{3/2}\right)6\mathrm{p}$ states, respectively, as shown in the stationary overview spectrum in Fig. 5.11. While the overall decrease of the optical density of these absorption lines is relatively weak in (a), it becomes increasingly significant with growing NIR intensity. The lowest optical density, which corresponds to the strongest depletion of the state population, is observed around the temporal overlap $\tau \approx 0$ of the XUV and NIR pulse. As visible in all time-delay scans, the optical density exhibits a relatively strong modulation for positive delays. The 2DAS representation reveals that the frequency components of this modulation peak at 1.4 and 1.7 eV. The origin of this signal is the interference with spectroscopically dark states of S- and D-symmetry that are initially populated due to leakage of the NIR light through the metal foil in the filter unit as it was also the case for the helium target (see Sec. 5.2). In this case, the effect is unwanted because it obscures the signature of the spin–orbit wave packet. However, in the 2DAS representation the beat frequency of the wave packet (1.92 eV) should be distinguishable from the two features at 1.4 and 1.7 eV. Note that the 2DAS color range has to be capped because the signal around the DC limit is much more pronounced than the features corresponding to finite beat frequencies (ratio $\approx 100:1$). Going from Fig. 5.16 (b) to (f) the position of the peak at 1.7 eV seems to move (the dashed lines show the final peak position) while the 1.4 eV signal remains constant. At the highest intensity, the 2DAS magnitude peaks at 1.85 eV (resolution 0.07 eV), which is close to the expected beat frequency of 1.92 eV of the spin–orbit wave packet. Up to now, it is not understood if the peak position moves due to the increasing intensity, or if a new effect, e.g. the spin–orbit wave- packet beating, in combination with a reduction of the original peak's magnitude is responsible for the apparent shift. Figure 5.17 allows for a closer look at the evolution of the Fourier spectrum as it shows lineouts along the resonance photon energy of the $\left(\mathrm{D}_{5/2}\right)6\mathrm{p}$ line in the 2DAS. The figure shows that the original peak at 1.7 eV develops a shoulder at 1.85 eV with increasing intensity. This is accompanied by a decreasing magnitude at

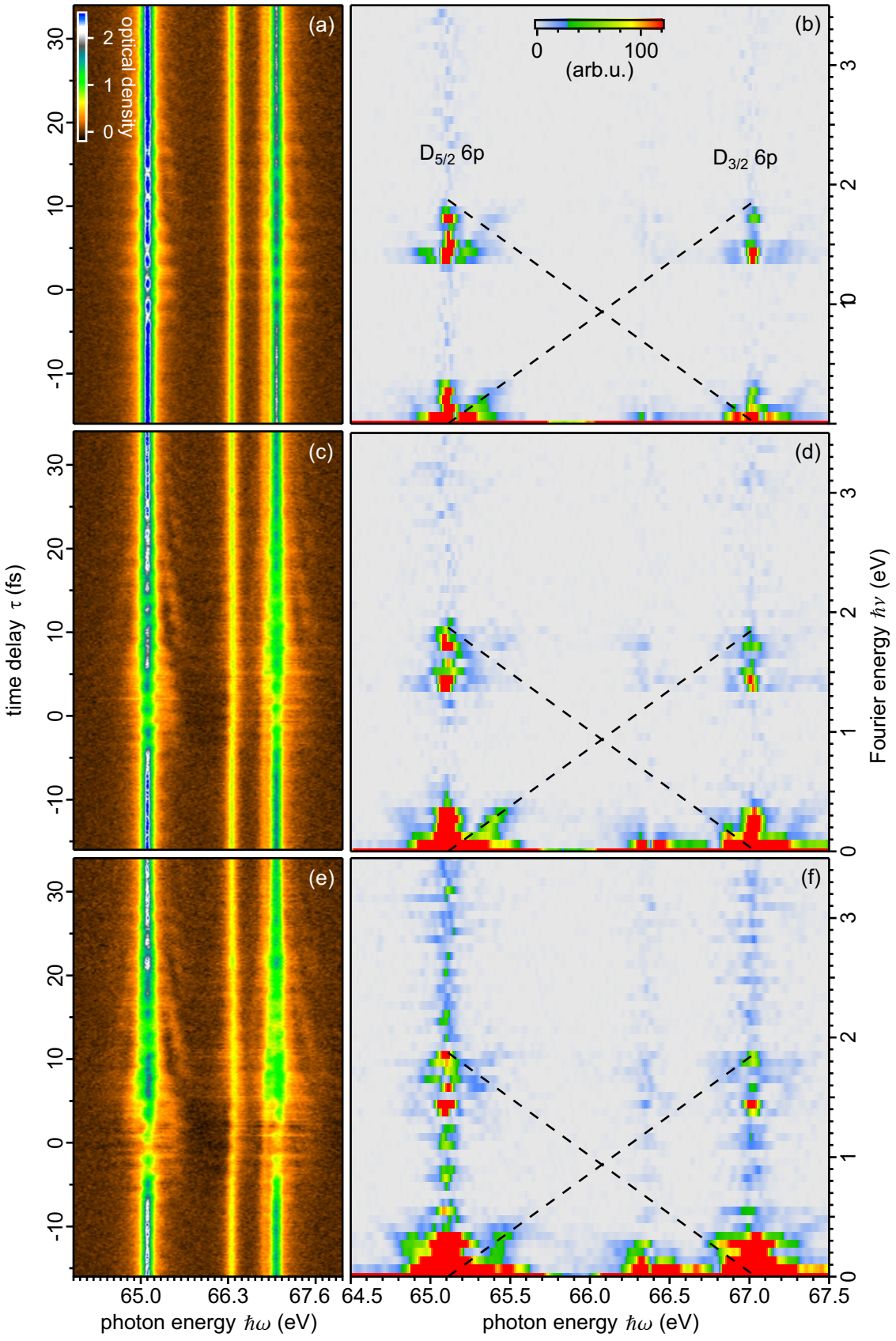

Fig. 5.16: *Time-delay scans (left column) and 2DAS magnitude (right column) of inner-valence excited xenon for three different NIR intensities (increasing from top to bottom row). For details please see main text.*

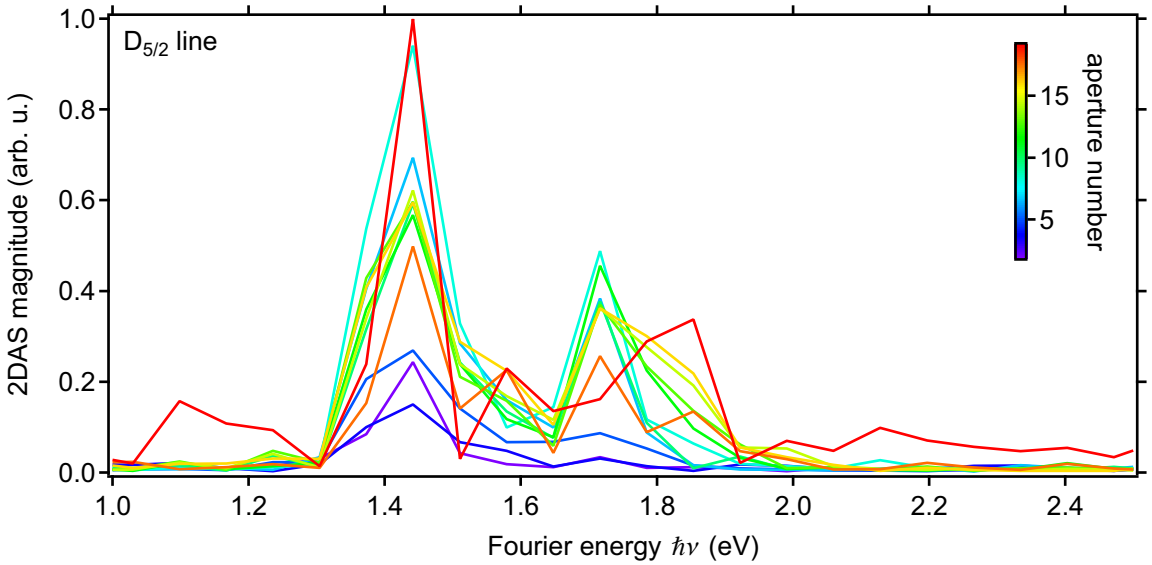

Fig. 5.17: *Lineouts of the 2DAS representation along the ν-axis at the position of the $(D_{5/2})6p$ line revealing the different frequency components that contribute to the final absorption spectrum. Each lineout corresponds to a different NIR intensity as encoded by the color bar (blue corresponds to low – red corresponds to high intensity)*

1.7 eV until at the highest NIR intensity, i.e. the solid red line (taken from Fig. 5.16 (f)), the former shoulder at 1.85 eV dominates. Apart from this, the final-intensity data exhibit considerably more noise than the other data and additional structures below 1.4 eV. Unfortunately, the intensity scan had to be aborted (for a sudden drop in laser power) after this intensity, so that the further evolution of the peak structure at even higher intensities remains unknown. Thus, a final conclusion about the origin of the apparent peak shift and the observation of the spin–orbit wave-packet signature cannot be made at this point. Further measurements, which should make use of shorter laser pulses in the 1.5 cycle regime, and a broader intensity scan are necessary to unambiguously prove the wave packet's existence and to study its properties in a strong-field environment.

Nevertheless, the concept of 2DAS was again demonstrated to be a helpful complement to the time delay–resolved representation of experimental data. The ability to spectroscopically separate different coupling channels by means of their Fourier energy is a key to study weak modulations of the spectrum that are otherwise obscured by other effects.

Chapter 6

In situ characterization of few-cycle strong-field laser pulses

In the field of ultrafast light–matter interaction with strong laser fields, the characterization of the laser pulses used to drive the (nonlinear) quantum dynamics is a crucial step in order to draw quantitative conclusions from measurement results.
There are various well-established ways to characterize the temporal structure of ultrashort laser pulses. The most prominent examples are the already mentioned SPIDER [102] and FROG [103] techniques as well as their numerous derivatives, e.g. spatially encoded arrangement (SEA) SPIDER [129] or interferometric (I) FROG [130]. Other pulse characterization techniques include the d-scan [101], self-referencing spectral interferometry (SRSI) [131], or the multiphoton intrapulse interference phase scan (MIIPS) method [132]. While these methods are powerful in a sense that they can be used to retrieve the spectral phase, and thus completely characterize the temporal structure of the pulse, they are not *in situ* methods. The main advantage of an *in situ* technique would be that the pulse is characterized directly inside the spectroscopy target under realistic conditions. Furthermore, the pulse intensity is not accessible by the aforementioned techniques, and for strong-field pulses the used medium (usually a nonlinear crystal) might even evaporate.
These facts create the urge for other techniques to be implemented in ultrafast and strong-field experiments. For the photoelectron community, the attosecond streaking technique [90–92] provides a powerful *in situ* method. Its principle is outlined in Sec. 3.3.1. It allows both to study quantum-dynamics on the electronic time scale as well as it provides a powerful pulse characterization technique that has become a standard over the last decade. The streaking method is able to temporally resolve the oscillation of the electric field itself, and thus allows to completely characterize the wave form of ultrashort laser pulses down to the single- or sub-cycle regime [67]. Furthermore, by implementation of reconstruction algorithms such as FROG CRAB [105] or phase retrieval by omega oscillation filtering (PROOF) [133] the attosecond pulse used in the streaking scheme can be characterized. Attosecond streaking also in principle allows to determine the absolute value of the electric field strength or the intensity of the femtosecond pulses from the measured kinetic energy shift of the photoelectrons.
These features come at the expense of relatively high requirements on the experimental

setup. First, the wave form of the NIR laser pulses has to be stabilized with low noise, which is achieved by CEP stabilization of the femtosecond oscillator and amplifier. If the CEP fluctuates from shot to shot, the measured photoelectron signal gets averaged over different field strengths and directions. This causes loss of the information on the field itself. Second, isolated attosecond pulses have to be produced. Otherwise the electric field of several half-cycles contributes to the photoelectron spectrum.
Conceptually, one of the major drawbacks of attosecond streaking and in general all photoelectron techniques is the necessity for liberating an electron from the studied target atom or molecule. Therefore, and as described previously in Sec. 3.1 ATAS has become an important complement that intrinsically provides access to bound-state quantum dynamics. Unlike the attosecond streaking technique, until very recently ATAS has lacked the possibility for *in situ* characterization of the femtosecond NIR laser pulses that drive and control the electron dynamics. The precise knowledge of the laser pulse shape and peak intensity—or in general of its instantaneous intensity distribution—enhances the scope of ATAS concerning quantitative measurements and the control of quantum dynamics. Together with an improved comparability between experimental and theoretical studies, where pulse duration and intensity are crucial input parameters, this enables a more detailed analysis and understanding of bound-state dynamics in strong and short laser fields.

The following chapter is dedicated to demonstrate a new scheme for ATAS combining the measurement of time-resolved quantum dynamics with the characterization of the few-cycle driving laser pulse in one single experiment. First the main idea behind the pulse characterization scheme is introduced and elaborated in terms of the dipole control model (DCM). Afterwards the method is validated by comparison with a numerical calculation before it is applied experimentally.

Most of this chapter's content is based on [2] and will adhere to this publication.

6.1 Few-cycle pulse characterization scheme

The presented pulse characterization method is based on extracting the time delay–dependent phase shift [1, 6, 7, 26, 42] imprinted on a resonance, which is excited by attosecond XUV light and dressed by the few-cycle–NIR laser pulse that is to be characterized. From this transient phase shift, the time-dependent intensity distribution is obtained. Since the signature of the NIR laser pulse interacting with the XUV-excited spectroscopy target is analyzed, the pulse characteristics are determined *in situ*, i.e. directly where the physics of quantum dynamics experiments studied with ATAS happens.

6.1.1 Principle

The physical mechanism behind the phase shift is the ponderomotive shift (see Sec. 2.5) of the energy of highly excited states, in which the electron is close to free. In general, bound states dressed by laser light are subject to the AC Stark effect. Here, a coupling of several states makes a theoretical treatment of a realistic scenario, e.g. using strong laser fields, complicated. However, in the vicinity of the continuum threshold, i.e. for high principal quantum numbers, the presence of a high density of states causes the Stark effect to eventually become the ponderomotive effect. This means that the Stark shift converges against the ponderomotive potential U_P. In the time domain, the electron's energy shift corresponds to an accelerated evolution of the wave functions phase for the duration of the laser pulse. In general the phase acquired in the presence of a time-dependent frequency is given by

$$\phi(t) = -i \int_{-\infty}^{t} \omega(t')\mathrm{d}t'. \tag{6.1}$$

In the case of an electron excited by an attosecond XUV pulse (treated as a Dirac-δ function) at time $t = 0$ to a close-to-free state (resonance frequency ω_r) that is dressed by an NIR pulse (ponderomotive potential U_P) Eq. 6.1 becomes

$$\phi(t) = -i \left[\omega_\mathrm{r} t + \frac{1}{\hbar} \int_0^t U_\mathrm{P}(t' - \tau)\mathrm{d}t' \right]. \tag{6.2}$$

The poderomotive potential U_P of the laser is (like the laser intensity) centered about the time τ, which corresponds to the time delay between excitation pulse (XUV) and interaction (NIR). Note that throughout these considerations the excitation pulse will be regarded as an XUV pulse and the interaction or dressing pulse will be regarded as an NIR pulse. However, there is no general restriction to these spectral regions as the presented concept is completely general. It is only the context of the recent ATAS studies, which makes it convenient to assign these spectral regions to the two pulses.

The phase evolution of the state according to Eq. 6.2 is illustrated in Fig. 6.1 (a). The presence of the laser pulse ponderomotive potential causes the electron to accumulate an additional phase of

$$\phi_\mathrm{P}(t, \tau) = -\frac{i}{\hbar} \int_0^t U_\mathrm{P}(t' - \tau)\mathrm{d}t'. \tag{6.3}$$

For the pulse characterization scheme the situation gets especially interesting in the vicinity of the pulse overlap, which is depicted in Fig. 6.1 (b). Here, the total phase accumulated

$$\Delta\phi_\mathrm{P}(\tau) = -\frac{i}{\hbar} \int_0^\infty U_\mathrm{P}(t' - \tau)\mathrm{d}t' \tag{6.4}$$

strongly depends on the time delay of the two pulses. In contrast, for time delays considerably longer than the pulse duration, as shown in Fig. 6.1 (a), $\Delta\phi_\mathrm{P}$ becomes stationary. In this way, by scanning the NIR pulse over the XUV pulse—similar to the attosecond streaking technique—the pulse shape is mapped onto the additional phase of the loosely bound electron. The early NIR pulse in Fig. 6.1 (b) arriving at time τ_l after the XUV pulse, which starts the "phase clock", only acts with slightly more than half of its duration on the electron. Thus, the imprinted phase is considerably smaller

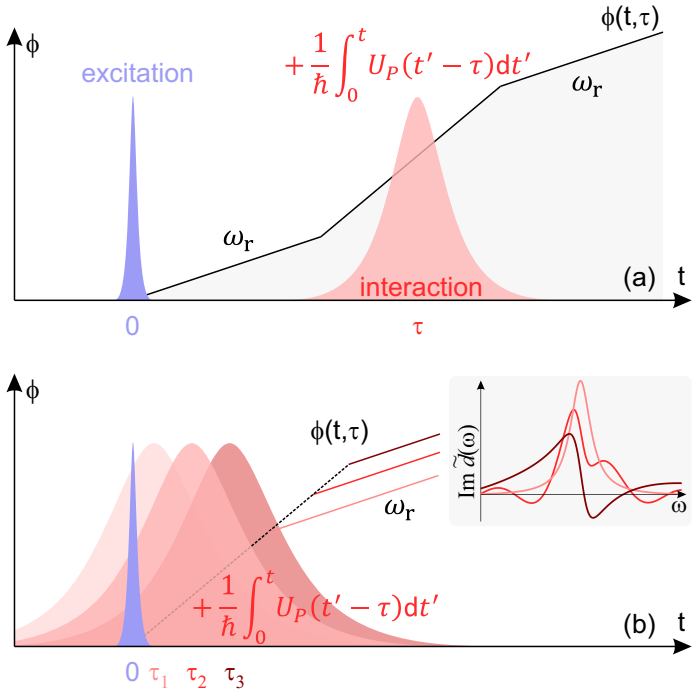

Fig. 6.1: *Illustration of the phase evolution of a laser-dressed resonance in general (a) and its application for pulse characterization (b). The presence of the laser pulse's ponderomotive potential causes the wave functions phase to evolve faster. In the vicinity of the pulse overlap the additional phase acquired by the electron explicitly depends on the timing of the NIR pulse. Thus, the temporal profile of the laser pulse is mapped onto the electron's phase, and thereby also on the spectral response, which can be measured in ATAS and analyzed be means of the DCM.*

compared with the phase that the late pulse arriving at τ_3 adds to the electron's phase evolution. The acquisition of an additional phase by the electron can be interpreted as a perturbed decay. This perturbation of the dipole decay in the time domain is associated with a modification of the absorption spectrum in the frequency domain as indicated in the figure. The remaining question is "How to extract the laser imprinted additional phase from the (measured) absorption spectrum?". The answer is given by the DCM. From Chap. 4, the effect of a given phase jump introduced at a given time delay τ on the spectral response of the system is known analytically (Eq. 4.17). The only task is now to cast the ponderomotive dressing of the electron by the NIR into the DCM, by finding a suitable expression for the dipole control parameter A. Then the analytic frame work of the DCM can be utilized in order to extract the phase information from the recorded spectra. This will be the content of the next section.

Once the laser imprinted phase $\Delta\phi_P(\tau)$ has been recovered from the absorption spectrum, the laser pulse can be characterized. The derivative of $\Delta\phi_P(\tau)$ with respect to the time delay directly yields the laser's instantaneous ponderomotive potential:

$$i\hbar\frac{d\Delta\phi_P}{d\tau} = U_P(\tau). \tag{6.5}$$

Of course, the absolute value of U_P depends on the validity of the assumption that the electron experiences the full ponderomotive potential rather than the ordinary Stark shift, which will be a subject of the next sections. From U_P the laser intensity can be calculated directly via Eq. 2.52 if the laser center wavelength is known, which usually is the case. With that, the pulse envelope is characterized completely. In principle, it should be possible to resolve also the cycle structure of the pulse intensity using this method. However, this would require—as in streaking—a CEP stable source, which is at the moment not available experimentally in the current laboratory.

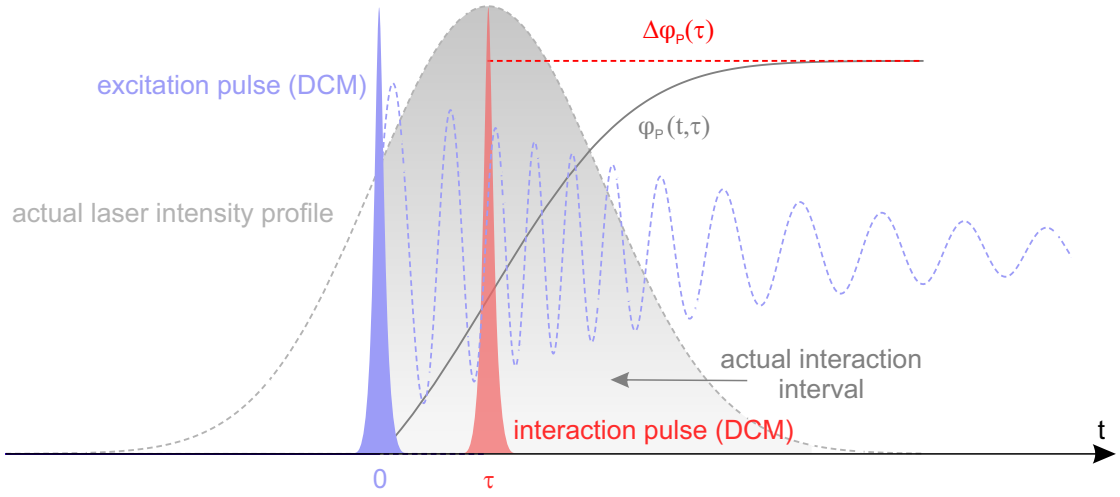

Fig. 6.2: *Dipole control model representation of the ponderomotive dressing of a highly excited state. The continuous evolution of the laser imprinted phase $\phi_P(t,\tau)$ is condensed to a phase jump $\Delta\phi_P(\tau)$ of the same amount as the total accumulated phase.*

6.1.2 Implementation using the dipole control model

In this section, the ponderomotive effect of an ultrashort dressing laser pulse will be expressed in terms of the DCM in order to allow for practical implementation of the pulse characterization scheme. At first glance, it might be confusing that in spite of the fact that the DCM treats all optical pulses as Dirac-δ functions the finite duration of the NIR pulse is going to be characterized using this model. However, the finite duration of the NIR pulse will enter in the form of the dipole control parameter A. As the ponderomotive effect is a non-resonant type of light–matter interaction, A should have the form

$$A(\tau) = a_1(\tau)e^{i\phi_1(\tau)} \tag{6.6}$$

where the time-delay dependence of amplitude a_1 and phase ϕ_1 is explicitly indicated. Furthermore, if the laser intensity is not too high, a depletion of the state can be neglected, such that a constant amplitude $a_1 = 1$ can be assumed:

$$A(\tau) = e^{i\phi_1(\tau)} \tag{6.7}$$

In order to cast the continuous action of the dressing laser into the impulsive DCM, a phase jump is introduced: the actually continuous phase accumulation caused by the NIR laser is condensed to an infinitesimally short instant in time (at $t = \tau$). The size of the phase jump is given by the total amount of laser-induced phase that the electron acquires:

$$A(\tau) = e^{i\Delta\phi_P(\tau)} = \exp\left[\frac{i}{\hbar}\int_0^\infty U_P(t'-\tau)\mathrm{d}t'\right] \tag{6.8}$$

Figure 6.2 illustrates this situation. Since the laser pulse maps its shape onto the electrons' phase via Eq. 6.4, the laser pulse is temporally resolved by scanning τ although it is treated

as a Dirac-δ function. Equation 6.8 contains no explicit time dependence so that the complex spectrum $\tilde{D}_\tau(\delta,\tau)$ is directly obtained in analogy to Eq. 4.14:

$$\tilde{D}_\tau(\delta,\tau) \propto \frac{-e^{i\phi_0}}{\delta - i\gamma} \times \begin{cases} 1 - e^{-i\delta\tau-\gamma\tau}\left[1 - e^{i\Delta\phi_\mathrm{P}(\tau)}\right] & \tau > 0 \\ e^{i\Delta\phi_\mathrm{P}(\tau)} & \tau < 0 \end{cases} \tag{6.9}$$

The Fano phase ϕ_0 accounts for the unperturbed line shape. The case of $\tau < 0$ does not appear in Eq. 4.14 but has to be introduced to describe the finite duration of the NIR pulse. It arises naturally by setting all instances of τ to zero except for $\Delta\phi_\mathrm{P}(\tau)$. The interpretation of this term is straight-forward: The electron is not affected by the dressing laser until $t = 0$. Hence, for all $\tau < 0$ the effect of the laser is treated to occur at $t = 0$, whereas via $\Delta\phi_\mathrm{P}(\tau)$ it is taken into account how much of the laser pulse the electron actually experiences. For laser pulses much shorter than the lifetime of the state, which is usually larger than 200 fs for the highly excited states of interest, this treatment causes no severe mistake since the action of the laser is anyhow confined very closely around $t = 0$ for $\tau < 0$. In this case, it was shown in [26] that the effect of the laser can be regarded purely as an additional initial phase, which is exactly what is written in Eq. 6.9.
In the following the imaginary part of Eq. 6.9, i.e. the absorption spectrum, will be used to retrieve the laser-imprinted phase from simulated and experimental data by fitting the analytic expression to given spectra.

6.2 Validation of the method

Before the *in situ* method is applied to experimental data, the retrieval mechanism shall be validated. Therefore, absorption spectra of an atomic resonance that is ponderomotively dressed by a few-cycle NIR pulse with known properties are numerically calculated. The pulse characteristics obtained by applying the characterization method to the spectra are then compared to the input pulse parameters. The main aim is to test whether the treatment of the phase acquisition as an instantaneous phase jump imposes severe limitations on the pulse retrieval.

The excitation step from the ground state to the highly excited state is performed perturbatively according to Eq. 5.19 where a 150 as XUV pulse is used. The ponderomotive effect of the dressing NIR laser pulse is treated according to Eq. 6.3 as a continuous shift of the states energy and phase. For comparability to the experimental situation, the simulation parameters of the state, i.e. resonance energy and decay rate, are chosen to match the sp_{24+} doubly excited state of helium (see Tab. 2.2). The simulation was carried out for Gaussian laser pulses of three different FWHM of intensity durations: 3.54 fs, 4.95 fs, and 7.07 fs (corresponding to FWHM of the electric field of 5 fs, 7 fs, and 10 fs, respectively). The peak ponderomotive potential of all three pulses is 350 meV. At a photon energy of 1.7 eV this corresponds to a peak intensity of 6.9×10^{12} W/cm^2. To retrieve the laser-imprinted phase from the calculated spectra the imaginary part of Eq. 6.9 plus an offset is fitted to the individual spectra of the time-delay scan. First, the fit is performed for negative time delay where the impact of the NIR pulse on the

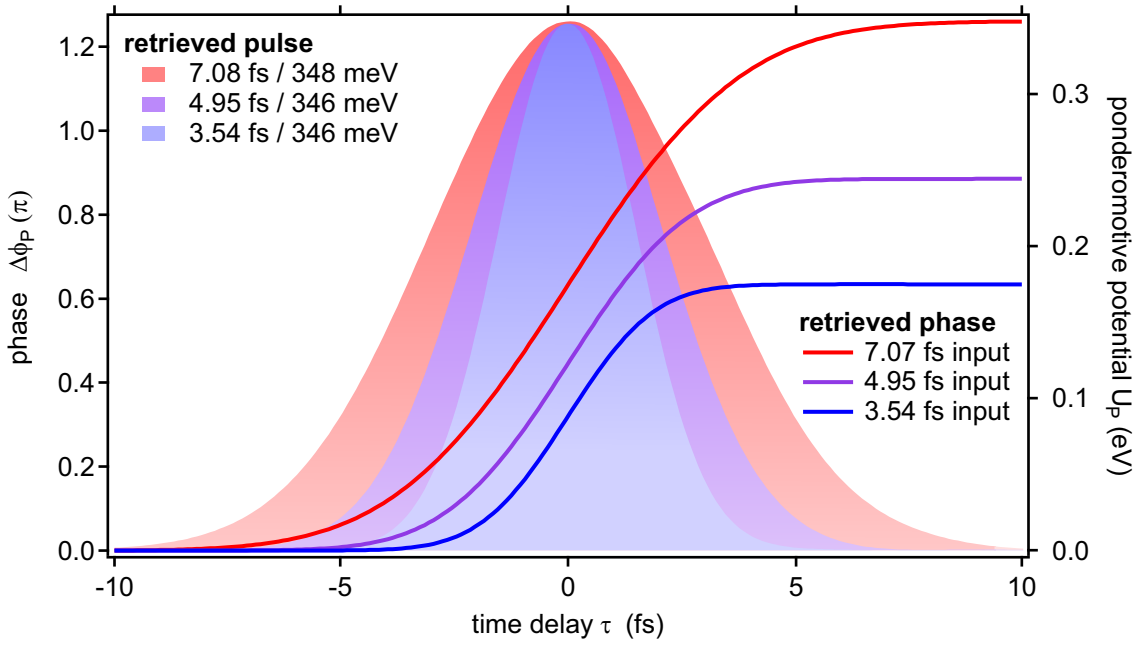

Fig. 6.3: *Validation of the DCM based phase retrieval for pulse characterization. The red, purple, and blue data sets correspond to input pulses of 7.07 fs, 4.95 fs, and 3.54 fs, respectively. For each of the pulses, the input peak ponderomotive potential is 350 meV. The lines correspond to the phase (left axis) retrieved by fitting the DCM spectrum of Eq. 6.9 to the simulated absorption spectra and the shaded areas correspond to the pulse profiles (right axis) obtained by derivation of the phase.*

absorption spectrum is negligible. In that case the laser imprinted phase vanishes, so that the initial phase ϕ_0 and the resonance frequency can be determined. These values are kept fixed throughout the following fits. Keeping the resonance frequency fixed is important because the variation of ω_r has a similar effect on the spectrum as a variation of the phase (both terms enter the exponent of Eq. 6.9). The time delay τ also enters the fitting as a fixed parameter taking the value of the current time delay-setting, which the fit is performed on.

Figure 6.3 shows the results of the phase retrieval and the pulse profiles obtained from the derivative of the retrieved phase with respect to τ. The pulse durations are obtained by fitting a Gaussian profile to the retrieved pulse. The deviation from the input values is below 0.2% in all three cases. Also the peak ponderomotive potential agrees within 0.6% with the input value of 350 meV. This demonstrates that the retrieval algorithm based on the DCM is able to perform a pulse characterization directly from transient absorption spectra with high accuracy and precision.

In addition to this validity check, a second – more demanding – test is carried out. In order to make the scenario more realistic, the spectra are now convolved with a 20 meV standard deviation Gaussian filter function, which simulates the finite resolution of the XUV spectrometer. Furthermore, instead of a Gaussian input pulse a less trivial input pulse that exhibits a post pulse is now used. The results of the pulse characterization are summarized in Fig. 6.4. Figures (a) and (b) show the convolved simulated absorption spectrum and its fit with the analytic DCM spectrum. As the figures reveal, except for details on the left side of the main absorption line, the DCM model approaches the

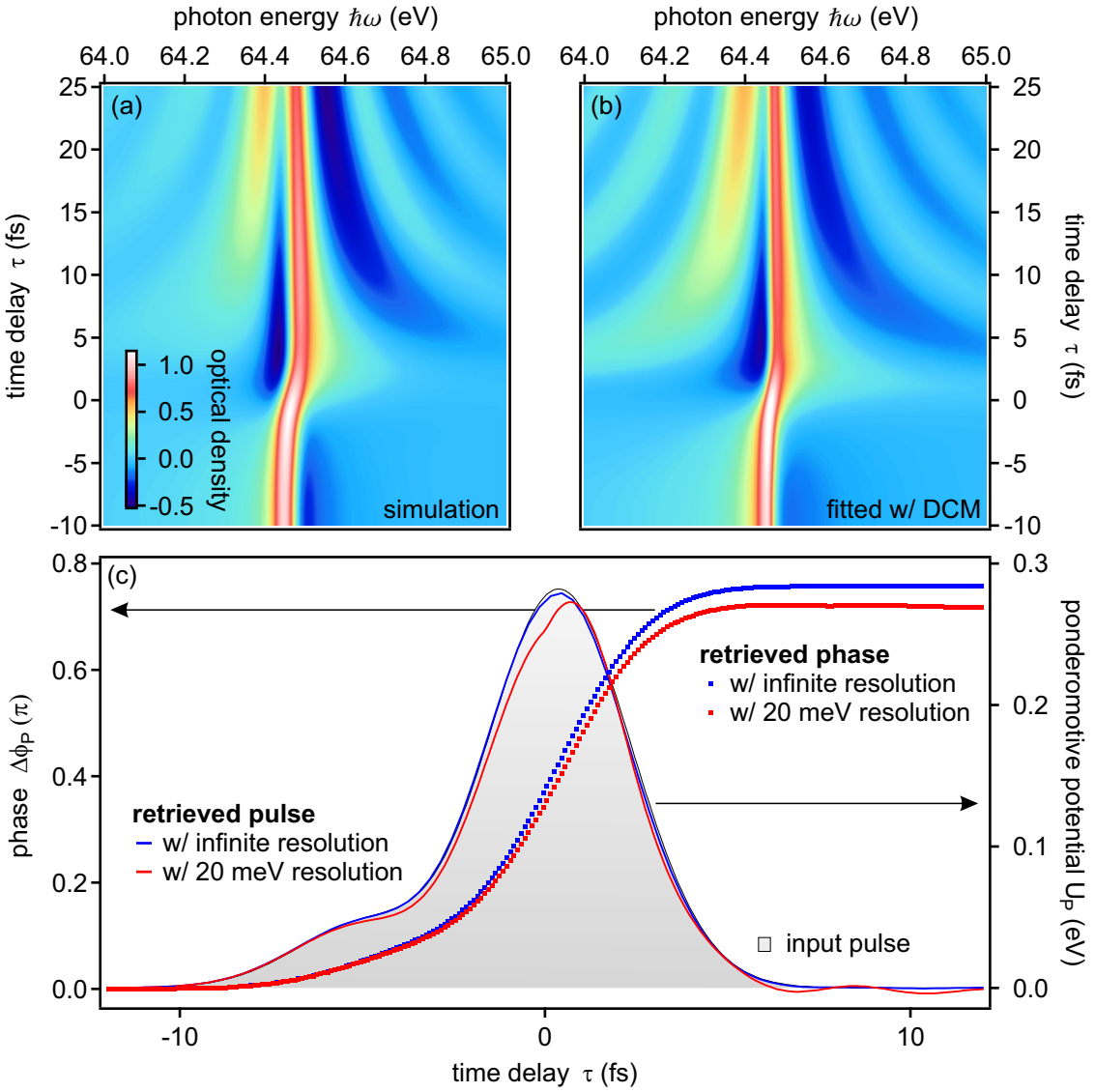

Fig. 6.4: *Validity check of the in situ method. (a) Simulated transient absorption spectrum of a ponderomotively dressed state. The absorption line is convolved with a 20 meV Gaussian filter function to simulate the spectrometer resolution. The line evolves starting from its natural shape at $\tau = -10$ fs. At $\tau \approx -1$ fs, the laser has imprinted enough additional phase so that the line shape is transformed to a symmetric Lorentzian-like profile. For positive time delays, the profile is converted further to an inverted Fano-profile, and hyperbolic structures start to emerge. For $\tau \to \infty$, the line shape will again turn into the natural one because the laser dressing acts on an exponentially decreasing part of the wave function. (b) spectrum of (a) fitted with the DCM spectrum of Eq. 6.9 in order to retrieve the laser-imprinted phase. The agreement is generally good, except for the fact that the DCM produces a spectrum that is more symmetric around the resonance frequency compared with the simulated spectrum. (c) Retrieved phase (dotted curves) and pulse profile (solid lines) compared to the input pulse (shaded area). The blue curves correspond to the unconvolved spectra, whereas the red curves correspond to the convolved spectra.*

simulated data very well. This is inspite of the fact that the convolution with the Gaussian function modifies the absorption line shape. Figure 6.4 (c) shows the phase obtained from the fit procedure and the retrieved pulse shape compared to the input pulse (gray shaded area). The red curves correspond to the spectra convolved with the 20 meV Gaussian spectrometer resolution function as shown in figures (a) and (b), whereas the blue curves correspond to unconvolved spectra, i.e. infinite spectrometer resolution. The overall pulse shape for the unconvolved spectra is in excellent agreement with the input pulse. The peak ponderomotive potential is underestimated by $\approx 1\%$. For the convolved spectra, the pulse shape exhibits noticeable deviations from the input pulse on the trailing edge of the pulse near the peak position, while the majority of the pulse shape agrees well with the input pulse. The reconstructed peak intensity is about 3.3% below the input value. The FWHM durations of retrieved pulse and input pulse agree on a sub-% level. Therefore, even with a finite resolution altering the line shape the DCM based retrieval method proves applicable to experimental data. However, as these tests reveal, the quality of the retrieval can be directly improved by using a higher resolution spectrometer.
In principle, if the spectrometer response function is known, the fit can be performed with the convolved DCM spectrum, which should compensate for the effect of the line shape modification. Doing so in the presented case where the spectrometer response is known exactly, eliminates the noticeable distortions of the pulse peak. Yet, the peak intensity remains approximately the same, i.e. 3% below the input peak intensity. Thus, a high spectrometer resolution is still the most favorable way to obtain accurate pulse properties.

As a final check, the dependence of the pulse retrieval on the XUV pulse duration is tested. The outcome of this test is that by going from a 150 as short excitation to an XUV pulse duration of 2000 as, which covers most experimental situations, the retrieved pulse duration (7 fs input) deviates by about 1.8%, which is usually below the time delay–scanning resolution in the experiment ($\Delta\tau = 170$ as corresponds to 2.5% at 7 fs pulse duration). The retrieved intensity for the 2000 as XUV pulse also is reduced by only 0.4%. In addition to that, a short train of attosecond pulses was also used to calculate spectra and perform the pulse retrieval. The train consists of three pulses: one center pulse of 150 as duration and two satellites displaced by an NIR half cycle. The satellites have a relative peak electric field of 1/4 with respect to the center pulse and the same duration. In this case, the retrieved pulse duration is 3.6% longer compared with the pulse duration retrieved with a 150 as XUV pulse. The peak intensity is underestimated by 2.0%.
These low systematic errors of the method for extended XUV pulse durations can be accounted for by incorporating them into the measurement result.

6.3 Application of the method

After introduction and validation of the pulse characterization scheme, it is now applied to experimental data. The pulse characterization is performed on a subset of the states shown in the overview spectra of Fig. 5.5, i.e. the sp_{2n+} Rydberg series of helium. Figure 6.5 shows a detailed absorption spectrum of the highest lying states, whereas

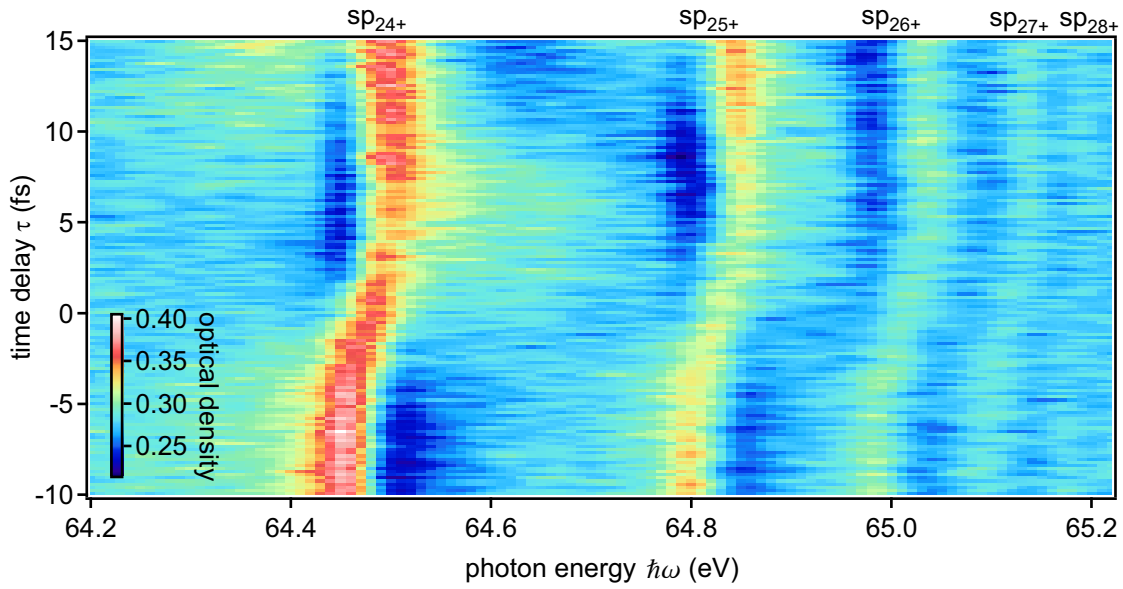

Fig. 6.5: *Overview of the highly excited states of the sp_{2n+} manifold starting from $n = 4$. The "twist" of the line shape is clearly visible from the time delay scan.*

a detailed view on the sp_{23+} state is given by Fig. 5.7. The Rydberg series is quickly converging to the $2s^1/2p^1$ ionization threshold of helium at 65.40 eV, so that for $n > 8$ or $E > 65.2$ eV no individual states can be resolved. For the highest lying states, the spectrometer resolution and the signal-to-noise ratio is too low to perform a reliable analysis, by means of fitting an analytic line shape to the experimental data. Thus, the analysis is focused on the sp_{23+}, sp_{24+}, sp_{25+}, and sp_{26+} states. All of these states are strongly affected by the NIR laser pulses due to their vicinity to the continuum. On the other hand, except for the sp_{23+} state, the 2DAS representation in Fig. 5.6 reveals no indications of resonant couplings among the highly excited states. Thus, the perturbation can be treated as purely non-resonant.

As demonstrated numerically in Fig. 6.4, the line shape changes significantly as the NIR dressing laser pulse is scanned over the XUV excitation pulse. This effect is due to the time delay–dependent amount of phase imprinted on the resonances. Now, by applying Eq. 6.9 in order to fit the experimental data, the additional phase acquired due to the ponderomotive dressing is extracted from the time-resolved spectrum. The fitting procedure is almost identical to the one for the simulated data described above. The only differences are that, first, a region of the spectrum around each resonance is selected for the fit to act on only one absorption line. And second, the spectrum is binned along the τ-axis in order to improve the signal-to-noise ratio. The bin size amounts to 16 time-delay steps, which corresponds to approximately one laser cycle. For the sp_{23+}, which exhibits a beating structure due to quantum interference with the 2s2p state (see Sec. 5.2), most of the rippling is averaged out because of the binning. The binned time delay scans are shown in Fig. 6.6 for the sp_{24+} (a) and the sp_{25+} (b) state. For the depicted intensity (approximately 6.4×10^{12} W/cm^2 as will be shown later), the line shape is transformed to a symmetric Lorentz-type profile at about $\tau \approx -2$ fs. The lifetime of the discussed states is between 80 fs for the sp_{23+} and more than 0.6 ps for the sp_{26+} state, which renders the

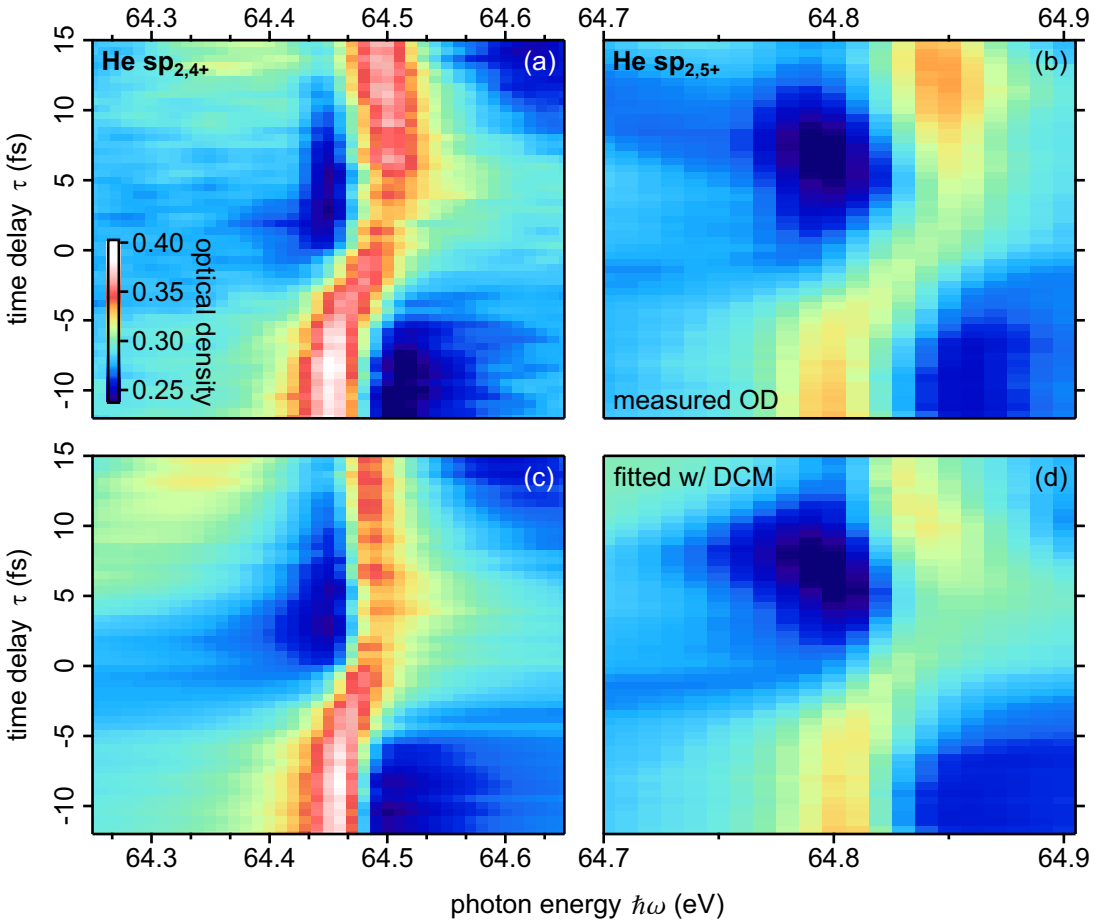

Fig. 6.6: *Binned experimental time-delay scans fitted with the analytic DCM spectrum to reconstruct the laser-imprinted phase. (a) and (b) show experimental time-resolved spectra of the sp_{24+} and sp_{25+} states, respectively. (c) and (d) show the corresponding fits with the imaginary part of Eq. 6.9 as fitting function. The fitting procedure is described in the main text.*

DCM approach applicable in the case of dressing laser pulses that extend only over a few optical cycles. The fitted spectra are shown in Fig. 6.6 (c) and (d). Similar to the simulated data, the fit results agree well with the experimental data, which demonstrates that the delay-dependent line shapes of transiently perturbed dipole decay can be analytically described in the frame of the DCM. The phase $\Delta\phi_P$ retrieved by the fit for each time-delay position is shown in Fig. 6.7. The general shape of the phase curves is as expected from the theoretical investigations of the previous section. There is a significant tendency that phase shift acquired up to a given time delay grows with the principal quantum number of the state. This growth occurs in a convergent fashion: the difference between succeeding states becomes smaller with increasing quantum number, which means that the phase curves approach each other. The difference between the phase maximum of the sp_{25+} and the sp_{26+} state is already less than 5%. This suggests that the highest lying states are close to the ponderomotive limit of free electrons—or in other words—the AC Stark shift that these states experience is close to the ponderomotive potential, which is the limit of the AC Stark shift for continuum electrons. In contrast, for the more strongly bound states,

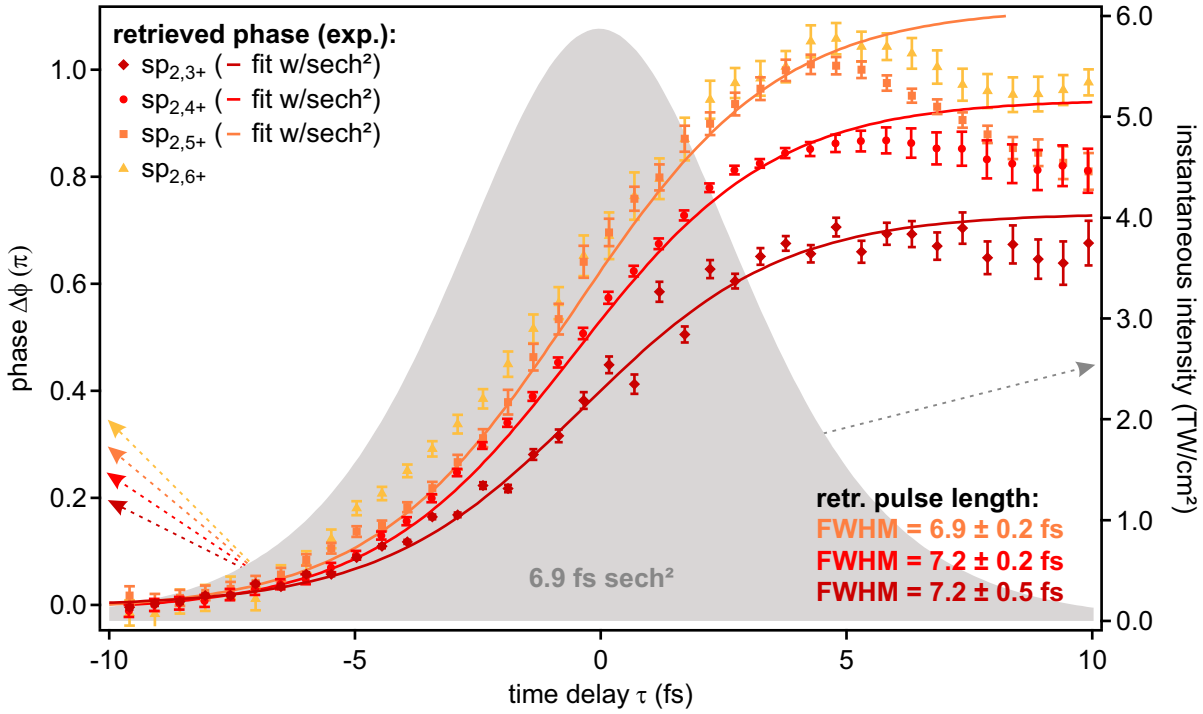

Fig. 6.7: *Phase retrieval and pulse reconstruction from experimental data. The scatter plots show the phase retrieved from the experimental absorption spectra while solid lines are the corresponding fit curves. The fitting function is an integrated sech^2 profile. The shaded area marks the pulse profile obtained from derivation of the phase profile of the sp$_{25+}$ state.*

e.g. the sp$_{23+}$ state, the phase shift clearly differs from the ponderomotive behavior. This is in agreement with the intuitive picture that the deeply bound states are less sensitive to the presence of the NIR laser pulse, whereas the weakly bound states are more affected by the electric field. By means of the phase retrieval, this finding can be quantified. The laser-imprinted phase can be regarded as the action the electron accumulates due to the presence of the laser. In the presented case, the action that the electron in the sp$_{26+}$ state experiences is about 60% higher compared with the sp$_{23+}$ state. If the temporal evolution of the action or the phase is equal in both states, which is approximately the case, this transfers to a difference in the energy shift of also 60%.

The absolute value of the phase maximum is approximately π in the case of the sp$_{25+}$ state. All states have in common that the phase maximum is reached after a delay of $\tau \approx 5$ fs. For larger time delays, and especially for the highly excited states, the retrieved phase starts to decline for yet unknown reasons. This behavior is not directly understandable within the DCM nor the numerical simulations presented in the last section. Intuitively one would assume the phase to be a monotonic function of the time delay, since it is the integrated energy shift, which is not expected to switch its sign during the course of the pulse (at least for the highest states where the ponderomotive effect dominates, which causes always a positive energy shift). In principle there are two approaches to explain this decline: either the phase really declines or the phase decline is not real and the phase retrieval algorithm introduces an error. A possible explanation for the first approach is the displacement of the beam caused by the motion of the split mirror introducing the time delay as described in Sec. 5.2.1. The foci are displaced by about 1 µm

per femtosecond time delay. Making a rough approximation where the beam is treated as a Gaussian (FWHM of d) as well as the pulse profile (FWHM of T), the pulse energy e corresponding to a peak intensity of I_0 is given by:

$$e = \left(\frac{\pi}{\mathrm{Log}\,2}\right)^{3/2} I_0\, d^2\, T \tag{6.10}$$

Plugging in the values of I_0 and T obtained later, assuming these values are obtained at the center of the beam, and assuming a pulse energy of 0.1 mJ leads to an FWHM spot size of about 160 µm. Under these assumptions, a displacement of the beam by 20 µm, which corresponds to 20 fs in time delay, would still lead to an intensity of 99% of the peak value. Thus, the observed behavior could only be explained if the XUV beam is completely displaced already at $\tau = 0$, which is rather unlikely, because the inner mirror was aligned carefully with respect to the outer mirror initially and was not modified since then. The second approach to explain the declining phase could be the close proximity of the highly excited resonances, which causes a slight delay-dependent overlap of the lines due the limited resolving power of the XUV spectrometer. This idea is supported by the growing error bars, which indicate that the fitting algorithm begins to struggle at larger τ. As it was the case concerning the simulation with the convolved absorption line, also in this case the method would directly benefit from a higher spectrometer resolution. Another possibility is the sub-ps pedestal, which usually accompanies femtosecond pulses from amplified lasers, and which can affect the atomic line shape. Such an additional field with a duration on the order of the state lifetime is currently not considered in the reconstruction method, which is based on the DCM, and thus assumes laser pulses much shorter than the lifetime of the studied states. As a result of this not completely understood phase decline, the data range used for the laser pulse measurement will be restricted to $\tau < 5$ fs.

The three lines that exhibit the strongest absorption signal and that are spectroscopically resolved best are the sp_{23+}, sp_{24+}, and sp_{25+} lines. The phase curves $\Delta\phi(\tau)$ can be reliably fitted with an integrated pulse profile P:

$$\Delta\phi_{\mathrm{fit}} = \int_{-\infty}^{\tau} P(\tau)\mathrm{d}\tau. \tag{6.11}$$

The highest lying state, i.e. sp_{26+}, agrees well with the sp_{25+} for most parts of the phase evolution. However, around $\tau = -4$ fs the phase exhibits a shoulder, which is not common among the other states. Fitting the sp_{26+} curve with a single pulse profile is not appropriate in respect of the shoulder, so that the information gained from this state is treated separately.
The fit with $\Delta\phi_{\mathrm{fit}}$ converges better if a sech^2 profile is used instead of the standard Gaussian. Figure 6.7 shows the fit results as solid lines. The FWHM pulse durations obtained from the fit are given by

$$T_{25+} = 6.9 \pm 0.2\,\mathrm{fs} \qquad T_{24+} = 7.2 \pm 0.2\,\mathrm{fs} \qquad T_{23+} = 7.2 \pm 0.5\,\mathrm{fs},$$

$$\overline{T}_{\mathrm{NIR}} = 7.1\,\mathrm{fs}$$

which corresponds to three optical cycles ($\overline{T}_{\mathrm{NIR}}$ is the mean value). The good agreement of all three values proves the reliability of the method, and shows that the determination of the pulse duration is relatively insensitive to the choice of the state or to the proximity to the ponderomotive limit. As visible from the Fig. 6.7, the data points according to the sp_{23+} state oscillate about the fit curve. This is a result of the residual beat signal that survived the cycle-averaging due to the binning. Hence, despite the strong resonant modulation of the sp_{23+} absorption line, the method is able to determine the underlying non-resonant phase shift well enough, to allow for a precise characterization of the driving laser pulse.
Concerning the determination of the absolute intensity of the femtosecond laser pulse, the choice of the state is not arbitrary. Only for the highest excited states the relation

$$\hbar\frac{\mathrm{d}\Delta\phi}{\mathrm{d}\tau} = \Delta E(\tau) \approx U_{\mathrm{P}}(\tau) \tag{6.12}$$

holds, where $\Delta E(\tau)$ is the general AC Stark shift of the state energy. Taking the derivative of the fitted phase curves with respect to τ yields the instantaneous AC Stark shift for the three states. The peak values reached at the laser pulse maximum read:

$$\Delta E_{25+}^{\max} = 0.28\,\mathrm{eV} \qquad \Delta E_{24+}^{\max} = 0.24\,\mathrm{eV} \qquad \Delta E_{23+}^{\max} = 0.18\,\mathrm{eV}.$$

These values exhibit the same tendency as expected from the comparison of the individual phase maxima. Based on the overall good agreement of the phase evolution of the sp_{25+} and the sp_{26+} state, the peak energy shift of the latter can be estimated by taking the value of the sp_{25+} state ($\Delta E_{25+}^{\max} = 0.28\,\mathrm{eV}$) and correcting it for the 5% higher phase maximum of the sp_{26+}. This yields

$$\Delta E_{26+}^{\max} = 0.29\,\mathrm{eV} \approx U_{\mathrm{P}}^{\max}. \tag{6.13}$$

As this energy shift is supposed to be very close to the ponderomotive potential of the dressing NIR laser, it can be used to determine the intensity, which the target was exposed to in the present study. Using Eq. 2.52 with a laser carrier wavelength of 730 nm, the peak intensity reads $I = 5.9 \times 10^{12}\,\mathrm{W/cm^2}$. The reconstructed instantaneous intensity for the whole pulse is shown as the grey area in Fig. 6.7. Assuming a situation of a short train of attosecond pulses as done in the validity check of the method slightly changes the values of the measurement result to $\overline{T}_{\mathrm{NIR}} = 6.9\,\mathrm{fs}$ and $I = 6.0 \times 10^{12}\,\mathrm{W/cm^2}$.

This technique based on the DCM and the corresponding experiment demonstrate—up to now—the first characterization of a strong-field few-cycle laser pulse performed by means of attosecond transient absorption spectroscopy. The instantaneous intensity, and thus also the duration and the peak intensity, of the laser pulse are determined *in situ*. This means, the pulse characterization takes place at the location where the investigated sample interacts with the intersecting NIR and XUV pulses or—in other words—where the physics of quantum dynamics experiments with short and strong laser fields happens. This combines quantum dynamics measurement and pulse characterization in one single experiment, which allows for direct data analysis and comparison between experiment and theory.
Finally, the limits of the method as well as its potential in the future is discussed.

6.3.1 Current limits—future outlook

In the future, CEP-stabilized NIR pulses will be used, which should enable characterization of the cycle structure of the laser pulse intensity. As both the attosecond pulse duration as well as the time delay–step size can in todays experiments be shorter than 100 as, the characterization of laser pulses shorter than one optical cycle (≈ 2.4 fs) should be feasible. Also a live implementation of the method is in principle possible, which would allow for direct dispersion optimization of the NIR pulses to match the experimental needs. To give an example: A delay range of -5 to $+5$ fs with 11 data points should be sufficient to characterize a few-cycle pulse roughly. Such a measurement can be performed in approximately 1 second (100 ms per integration time per delay step) if the pulse-to-pulse stability and the XUV flux are sufficiently high. The phase retrieval algorithm for 11 spectra is faster than the recording of the spectra (and can run in parallel), so that the pulse duration can be updated at least every 1.5 seconds, which is convenient for online optimization of the pulses.
Up to now, the sensitivity of the method is limited to about 5×10^{11} W/cm^2, which is mainly because of measurement noise due to pulse-to-pulse fluctuations. These fluctuations are imposed by the laser system itself and by air fluctuations along the beam path. Inside the hollow-core fiber and the HHG gas cell, initial fluctuations get amplified due to nonlinear effects (mainly self-phase modulation and harmonic generation). Thus, a stable laboratory environment and a laser system with low shot-to-shot fluctuations of the pulse parameters, e.g. a regenerative amplifier, would contribute to the sensitivity of the method. As mentioned before, an increased resolution of the XUV spectrometer would also enhance the pulse characterization technique in basically two points. First, the line shape becomes less affected by the spectrometer resolution, which improves the fit of the recorded spectra with the analytic spectrum. Second, the reduced width causes the lines to be better separated. Thus, overlapping of the absorption lines becomes less of an issue, and more highly excited states can be resolved, which allows for even more precise determination of the pulse. Instead of going further to the ponderomotive limit, the accuracy of the method could also be improved by theoretical calculations of the laser-induced Stark shift, which can be compared to the experimentally obtained energy shift in order to retrieve the laser intensity.

Chapter 7

Conclusion

The main topic of this thesis is the impulsive control of quantum dynamics in highly excited atoms by means of NIR laser pulses spanning only a few optical cycles. The range of proposed, observed and utilized processes of light–matter interaction within this thesis involves resonant coupling of states, non-resonant strong-field ionization introducing a quasi-coupling of states, and the transient shift of state energies caused by the non-resonant ponderomotive effect. The link between the physics of these light-induced quantum dynamics and the experimental outcome is established by means of an analytic framework—the dipole control model (DCM). Based on this model, two improvements to the promising technique of attosecond transient absorption spectroscopy (ATAS) are proposed and experimentally demonstrated. First, the (traditional) time delay–resolved representation of spectroscopic data is complemented by a two-dimensional–spectral representation, which allows for a deeper insight into individual processes of laser–atom interaction. And secondly, an *in situ* method for characterization of few-cycle strong-field laser pulses from transient absorption spectra is implemented.

The dipole control model is initially formulated in the time domain. Both light pulses—the attosecond XUV and the time delayed femtosecond NIR—are treated as infinitesimally short Dirac-δ functions. This allows to analytically describe the dipole response of an isolated state, which is the central quantity of the model, triggered by the XUV pulse and later perturbed by the NIR pulse. The interaction of the NIR pulse with the atom is condensed to a single complex parameter—the dipole control parameter $A(\tau)$. Two different general forms of $A(\tau)$ could be found that describe either resonant or non-resonant processes. One of the strengths of this model is that the transition to the frequency domain can be performed fully analytically yielding the optical density as a function of photon energy and time delay. This allows to directly trace the impact of the light–matter interaction from the time domain to the experimentally accessible spectral domain, which helps to extract quantum dynamics from measured spectra.
The key assumption of the model is that both pulse durations are short compared to the lifetimes of the investigated state. The time delay between excitation and interaction, however, is completely arbitrary. A notable special case occurs for time delays that are negligible compared to the state lifetime. Here, the intensely studied Fano phase formalism arises, which has allowed to describe the transformation of spectroscopic line shapes

from Lorentz to (the general asymmetric) Fano and *vice versa* in terms of an NIR-induced phase jump close to the temporal overlap [7, 26, 88]. In contrast, the full DCM allows for the complete dynamics of the interaction to be described. This involves spectroscopic line shapes beyond Fano (including Lorentzian for $q \gg 1$), which can be generated and understood. Hence, the insight into light–matter interaction that is granted by ATAS is improved even further.
Besides being introduced theoretically, the DCM is applied to develop two independent methods that help to improve the ATAS technique, and thus further support the understanding and control of ultrafast electron dynamics.

As the number of simultaneously occurring effects of laser–atom interaction involving strong and ultrashort laser pulses can be numerous, time delay–dependent absorption spectra tend to be complicated to be read and understood. Therefore, the concept for an alternative representation of the experimental data is investigated in this thesis. By taking the Fourier transform along the time-delay axis, the data is cast into a two-dimensional–spectral representation. This technique and the respective spectral map are named two-dimensional absorption spectroscopy/spectrum (2DAS). The starting point for developing the concept and interpreting the 2DAS data are time delay–dependent absorption spectra calculated by means of the DCM. Fourier transform again yields an analytic expression for the 2DAS, which allows to interpret the signatures that different types of light–matter interaction imprint on the 2DAS. The main advantage of 2DAS compared with the time delay–resolved representation is that different interaction pathways are spectroscopically separated according to the frequency at which they modulate the spectrum, whereas in the traditional representation, all pathways interfere giving rise to a strongly modulated spectrum. Therefore, even faint modulations of the spectrum, which otherwise could be overlooked or interpreted as noise, can be detected as they are separated from the rest. Moreover, since the 2DAS is a complex-valued map, also phase information can be extracted and attributed to the individual interaction process.
After the basic structure of the 2DAS is understood with the help of the DCM, the technique is applied in order to investigate the ultrafast dynamics of quantum wave packets in two systems. In both cases the wave packet is triggered by the coherent excitation of states via the XUV pulse. However, the probing of the wave packet via the NIR pulse involves very different physics.
In the first case, the XUV pulse lifts both electrons of the helium atom into so-called doubly excited states. The NIR pulse transiently couples two of these states via an intermediate dipole-forbidden state by means of a resonant–two-photon transition. The different eigenfrequencies of the two states give rise to an ultrafast modulation of the optical density, as a result of quantum interference. In the 2DAS, this signature oscillation across the time-delay scan corresponds to a single peak structure. Reading the phase and laser-intensity dependence of the peak magnitude gives additional insight into the response of the system with respect to the NIR pulse. The results match the theoretical predictions, which validates the method.
In the second study, a 4d-shell electron of xenon is lifted to the np ($n \geq 6$) shell by the XUV pulse. These excited states are affected by the spin–orbit interaction leading to two final-state manifolds with an energy separation of 1.92 eV for the lowest states ($n = 6$). The coherently excited wave packet of the $\left(\mathrm{D}_{5/2}\right)6\mathrm{p}$ and the $\left(\mathrm{D}_{3/2}\right)6\mathrm{p}$ state

correspondingly has an expected beating period of 2.1 fs. However, a direct probing of the wave packet, as done in the helium case via two-photon coupling, is not possible with the available bandwidth of the NIR. Thus, an alternative process to probe the wave packet by means of strong-field ionization of the excited electron is proposed. Here, the selectivity of the ionization rate with respect to the magnetic quantum number m_l in the (l, m_l)-basis is used to effectively project both wave-packet states onto the same (l, m_l) state. As in the case of direct coupling, this should result in a beating of the state populations, which can be detected by absorption spectroscopy. However, for the given pulse parameters of the current experimental setup, the beat signal is expected to be very weak because the probing of the wave packet is not resonant with respect to its frequency. This results in a loss of coherence and measurable signal for pulses longer than 1.5 optical cycles. Nevertheless, first experiments show indications of the existence and successful probing of the wave packet but further experiments are necessary in order to unambiguously prove this.

The second method that is demonstrated within this thesis allows to characterize the few-cycle strong-field laser pulses, which are used to drive (nonlinear) quantum dynamics in ATAS experiments, directly inside the spectroscopy target. Up to this point, ATAS was lacking such an *in situ* measurement of laser pulse properties, which was one of the major drawbacks compared to attosecond streaking. Here, the transiently applied ponderomotive shift of loosely bound–XUV-ecited states is used to imprint a phase onto the dipole response. This phase represents the integrated ponderomotive potential of the NIR pulse. Similar to attosecond streaking, as the XUV pulse is scanned over the NIR pulse, the bound of integration is moved so that the NIR pulse profile is temporally resolved with sub-fs precision. The amount of phase imprinted on the resonance is encoded in the absorption spectrum. With the help of the DCM formalism the laser imprinted phase, and thereby its intensity distribution, is directly retrieved from the measured line shape. This *in situ* characterization of laser pulses, will enhance the scope of ATAS towards quantitative measurement and precise control of quantum dynamics on electronic time scales. In addition, as the laser pulse properties are an important degree of freedom in theoretical calculations, knowledge of these properties will increase the comparability of experiments and theory.

Bibliography

[1] A. Blättermann, C. Ott, A. Kaldun, T. Ding, and T. Pfeifer.
Two-dimensional spectral interpretation of time-dependent absorption near laser-coupled resonances.
J. Phys. B: At. Mol. Opt. Phys. (2014).

[2] A. Blättermann, C. Ott, A. Kaldun, T. Ding, V. Stooß, M. Laux, M. Rebholz, and T. Pfeifer.
In situ characterization of few-cycle laser pulses in transient absorption spectroscopy.
Opt. Lett. **40**, 3464–3467 (Aug 2015).
URL `http://ol.osa.org/abstract.cfm?URI=ol-40-15-3464`.

[3] C.-T. Chiang, A. Blättermann, M. Huth, J. Kirschner, and W. Widdra.
High-order harmonic generation at 4MHz as a light source for time-of-flight photoemission spectroscopy.
Appl. Phys. Lett. **101**, 071116 (2012).

[4] C.-T. Chiang, A. Blättermann, M. Huth, J. Kirschner, and W. Widdra.
Oscillator-based High-order Harmonic Generation at 4MHz for Applications in Time-of-Flight Photoemission Spectroscopy.
In *EPJ Web of Conferences*, volume 41, p. 01019. EDP Sciences (2013).

[5] A. Blättermann, C.-T. Chiang, and W. Widdra.
Atomic line emission and high-order harmonic generation in argon driven by 4-MHz sub-μJ laser pulses.
Phys. Rev. A **89**, 043404 (Apr 2014).
URL `http://link.aps.org/doi/10.1103/PhysRevA.89.043404`.

[6] C. Ott, A. Kaldun, L. Argenti, P. Raith, K. Meyer, M. Laux, Y. Zhang, A. BlÃd'ttermann, S. Hagstotz, T. Ding, and et al.
Reconstruction and control of a time-dependent two-electron wave packet.
Nature **516**, 374–378 (Dec 2014).
URL `http://dx.doi.org/10.1038/nature14026`.

[7] A. Kaldun, C. Ott, A. Blättermann, M. Laux, K. Meyer, T. Ding, A. Fischer, and T. Pfeifer.
Extracting Phase and Amplitude Modifications of Laser-Coupled Fano Resonances.
Phys. Rev. Lett. **112**, 103001 (2014).

[8] V. Stooß, A. Kaldun, C. Ott, A. Blättermann, T. Ding, and T. Pfeifer.
Inversion symmetry breaking of atomic bound states in strong and short laser fields.
arXiv:1506.01182 (2015).

[9] T. Ding, C. Ott, A. Kaldun, A. Blättermann, K. Meyer, V. Stooß, M. Rebholz, P. Birk, M. Hartmann, A. Brown, H. V. D. Hart, and T. Pfeifer.
Time-resolved four-wave-mixing spectroscopy for inner-valence transitions.
arXiv: 1510.08698 (2015).

[10] R. Hildner, D. Brinks, J. B. Nieder, R. J. Cogdell, and N. F. van Hulst.
Quantum coherent energy transfer over varying pathways in single light-harvesting complexes.
Science **340**, 1448–1451 (2013).

[11] M. Malumbres and M. Barbacid.
Milestones in cell division: to cycle or not to cycle: a critical decision in cancer.
Nature Reviews Cancer **1**, 222–231 (2001).

[12] S. M. Falke, C. A. Rozzi, D. Brida, M. Maiuri, M. Amato, E. Sommer, A. De Sio, A. Rubio, G. Cerullo, E. Molinari, and C. Lienau.
Coherent ultrafast charge transfer in an organic photovoltaic blend.
Science **344**, 1001–1005 (2014).

[13] M. Dell'Angela, T. Anniyev, M. Beye, R. Coffee, A. Föhlisch, J. Gladh, T. Katayama, S. Kaya, O. Krupin, J. LaRue, et al.
Real-time observation of surface bond breaking with an X-ray laser.
Science **339**, 1302–1305 (2013).

[14] M. Schultze, E. M. Bothschafter, A. Sommer, S. Holzner, W. Schweinberger, M. Fiess, M. Hofstetter, R. Kienberger, V. Apalkov, V. S. Yakovlev, et al.
Controlling dielectrics with the electric field of light.
Nature **493**, 75–78 (2013).

[15] A. DeMaria, D. Stetser, and H. Heynau.
Self Mode-locking of Lasers with saturable absorbers.
Applied Physics Letters **8**, 174–176 (1966).

[16] L. Dahlström.
Passive mode-locking and Q-switching of high power lasers by means of the optical Kerr effect.
Optics Communications **5**, 157–162 (1972).

[17] A. Baltuška, T. Udem, M. Uiberacker, M. Hentschel, E. Goulielmakis, C. Gohle, R. Holzwarth, V. S. Yakovlev, A. Scrinzi, T. W. Hänsch, and F. Krausz.
Attosecond control of electronic processes by intense light fields.
Nature **421**, 611–615 (2003).

[18] A. L. Cavalieri, E. Goulielmakis, B. Horvath, W. Helml, M. Schultze, M. Fiess, V. Pervak, L. Veisz, V. S. Yakovlev, M. Uiberacker, A. Apolonski, F. Krausz, and R. Kienberger.
Intense 1.5-cycle near infrared laser waveforms and their use for the generation of ultra-broadband soft-x-ray harmonic continua.
New J. Phys. **9** (2007).

[19] E. Goulielmakis, M. Schultze, M. Hofstetter, V. S. Yakovlev, J. Gagnon, M. Uiberacker, A. L. Aquila, E. M. Gullikson, D. T. Attwood, R. Kienberger, F. Krausz, and U. Kleineberg.
Single-cycle nonlinear optics.
Science **320**, 1614–1617 (2008).

[20] A. McPherson, G. Gibson, H. Jara, U. Johann, T. S. Luk, I. A. McIntyre, K. Boyer, and C. K. Rhodes.
Studies of multiphoton production of vacuum-ultraviolet radiation in the rare gases.
J. Opt. Soc. Am. B **4**, 595–601 (Jun 1987).
URL `http://dx.doi.org/10.1364/JOSAB.4.000595`.

[21] P. M. Paul, E. S. Toma, P. Breger, G. Mullot, F. Auge, P. Balcou, H. G. Muller, and P. Agostini.
Observation of a train of attosecond pulses from high harmonic generation.
Science **292**, 1689–1692 (2001).

[22] M. Hentschel, R. Kienberger, C. Spielmann, G. A. Reider, N. Milosevic, T. Brabec, P. Corkum, U. Heinzmann, M. Drescher, and F. Krausz.
Attosecond metrology.
Nature **414**, 509–513 (2001).

[23] K. Zhao, Q. Zhang, M. Chini, Y. Wu, X. Wang, and Z. Chang.
Tailoring a 67 attosecond pulse through advantageous phase-mismatch.
Opt. Lett. **37**, 3891–3893 (Sep 2012).
URL `http://ol.osa.org/abstract.cfm?URI=ol-37-18-3891`.

[24] M. Drescher, M. Hentschel, R. Kienberger, M. Uiberacker, V. Yakovlev, A. Scrinzi, T. Westerwalbesloh, U. Kleineberg, U. Heinzmann, and F. Krausz.
Time-resolved atomic inner-shell spectroscopy.
Nature **419**, 803–807 (2002).

[25] M. Schultze, M. Fiess, N. Karpowicz, J. Gagnon, M. Korbman, M. Hofstetter, S. Neppl, A. L. Cavalieri, Y. Komninos, T. Mercouris, C. A. Nicolaides, R. Pazourek, S. Nagele, J. Feist, J. Burgdorfer, A. M. Azzeer, R. Ernstorfer, R. Kienberger, U. Kleineberg, E. Goulielmakis, F. Krausz, and V. S. Yakovlev.
Delay in Photoemission.
Science **328**, 1658–1662 (2010).

[26] C. Ott, A. Kaldun, P. Raith, K. Meyer, M. Laux, J. Evers, C. H. Keitel, C. H. Greene, and T. Pfeifer.
Lorentz Meets Fano in Spectral Line Shapes: A Universal Phase and Its Laser Control.
Science **340**, 716–720 (2013).

[27] M. F. Kling, C. Siedschlag, A. J. Verhoef, J. I. Khan, M. Schultze, T. Uphues, Y. Ni, M. Uiberacker, M. Drescher, F. Krausz, and M. J. J. Vrakking.
Control of electron localization in molecular dissociation.
Science **312**, 246–248 (2006).

[28] F. Kelkensberg, C. Lefebvre, W. Siu, O. Ghafur, T. T. Nguyen-Dang, O. Atabek, A. Keller, V. Serov, P. Johnsson, M. Swoboda, T. Remetter, A. L'Huillier, S. Zherebtsov, G. Sansone, E. Benedetti, F. Ferrari, M. Nisoli, F. Lépine, M. F. Kling, and M. J. J. Vrakking.
Molecular Dissociative Ionization and Wave-Packet Dynamics Studied Using Two-Color XUV and IR Pump-Probe Spectroscopy.
Phys. Rev. Lett. **103**, 123005 (2009).

[29] A. L. Cavalieri, N. Müller, T. Uphues, V. S. Yakovlev, A. Baltuška, B. Horvath, B. Schmidt, L. Blümel, R. Holzwarth, S. Hendel, M. Drescher, U. Kleineberg, P. M. Echenique, R. Kienberger, F. Krausz, and U. Heinzmann.
Attosecond spectroscopy in condensed matter.
Nature **449**, 1029–1032 (2007).

[30] S. Neppl, R. Ernstorfer, E. M. Bothschafter, A. Cavalieri, D. Menzel, J. Barth, F. Krausz, R. Kienberger, and P. Feulner.
Attosecond time-resolved photoemission from core and valence states of magnesium.
Physical review letters **109**, 087401 (2012).

[31] A. Schiffrin, T. Paasch-Colberg, N. Karpowicz, V. Apalkov, D. Gerster, S. Mühlbrandt, M. Korbman, J. Reichert, M. Schultze, S. Holzner, et al.
Optical-field-induced current in dielectrics.
Nature **493**, 70–74 (2013).

[32] J. Itatani, J. Levesque, D. Zeidler, H. Niikura, H. Pepin, J. C. Kieffer, P. B. Corkum, and D. M. Villeneuve.
Tomographic imaging of molecular orbitals.
Nature **432**, 867–871 (2004).

[33] A. Shiner, B. Schmidt, C. Trallero-Herrero, H. Wörner, S. Patchkovskii, P. Corkum, J. Kieffer, F. Légaré, and D. Villeneuve.
Probing collective multi-electron dynamics in xenon with high-harmonic spectroscopy.
Nature Physics **7**, 464–467 (2011).

[34] T. T. Luu, M. Garg, S. Y. Kruchinin, A. Moulet, M. T. Hassan, and E. Goulielmakis.
Extreme ultraviolet high-harmonic spectroscopy of solids.
Nature **521**, 498âĂŞ502 (May 2015).
URL `http://dx.doi.org/10.1038/nature14456`.

[35] P. Kraus, O. Tolstikhin, D. Baykusheva, A. Rupenyan, J. Schneider, C. Bisgaard, T. Morishita, F. Jensen, L. Madsen, and H. Wörner.
Observation of laser-induced electronic structure in oriented polyatomic molecules.

Nature communications **6** (2015).

[36] P. Eckle, M. Smolarski, P. Schlup, J. Biegert, A. Staudte, M. Schöffler, H. G. Muller, R. Dörner, and U. Keller.
Attosecond angular streaking.
Nat. Physics **4**, 565–570 (2008).

[37] P. Eckle, A. Pfeiffer, C. Cirelli, A. Staudte, R. Dörner, H. Muller, M. Büttiker, and U. Keller.
Attosecond ionization and tunneling delay time measurements in helium.
science **322**, 1525–1529 (2008).

[38] Z. H. Loh, M. Khalil, R. E. Correa, R. Santra, C. Buth, and S. R. Leone.
Quantum state-resolved probing of strong-field-ionized xenon atoms using femtosecond high-order harmonic transient absorption spectroscopy.
Phys. Rev. Lett. **98**, 143601 (2007).

[39] H. Wang, M. Chini, S. Chen, C.-H. Zhang, F. He, Y. Cheng, Y. Wu, U. Thumm, and Z. Chang.
Attosecond Time-Resolved Autoionization of Argon.
Phys. Rev. Lett. **105**, 143002 (2010).

[40] E. Goulielmakis, Z. H. Loh, A. Wirth, R. Santra, N. Rohringer, V. S. Yakovlev, S. Zherebtsov, T. Pfeifer, A. M. Azzeer, M. F. Kling, S. R. Leone, and F. Krausz.
Real-time observation of valence electron motion.
Nature **466**, 739–7U7 (2010).

[41] M. Holler, F. Schapper, L. Gallmann, and U. Keller.
Attosecond Electron Wave-Packet Interference Observed by Transient Absorption.
Phys. Rev. Lett. **106**, 123601 (2011).

[42] C. Lin and W.-C. Chu.
Controlling atomic line shapes.
Science **340**, 694–695 (2013).

[43] R. Santra, V. S. Yakovlev, T. Pfeifer, and Z.-H. Loh.
Theory of attosecond transient absorption spectroscopy of strong-field-generated ions.
Physical Review A **83**, 033405 (2011).

[44] M. B. Gaarde, C. Buth, J. L. Tate, and K. J. Schafer.
Transient absorption and reshaping of ultrafast XUV light by laser-dressed helium.
Physical Review A **83**, 013419 (2011).

[45] S. Chen, M. J. Bell, A. R. Beck, H. Mashiko, M. Wu, A. N. Pfeiffer, M. B. Gaarde, D. M. Neumark, S. R. Leone, and K. J. Schafer.
Light-induced states in attosecond transient absorption spectra of laser-dressed helium.
Phys. Rev. A **86**, 063408 (Dec 2012).
URL `http://link.aps.org/doi/10.1103/PhysRevA.86.063408`.

[46] J.-C. Diels and W. Rudolph.
Ultrashort Laser Pulse Phenomena.
Second Edition. Academic Press (2006).

[47] B. E. A. Saleh and M. C. Teich.
Fundamentals of Photonics.
Second Edition. Wiley (2007).

[48] Z. Chang.
Fundamentals of Attosecond Optics.
CRC Press (2011).

[49] T. Brabec and F. Krausz.
Intense few-cycle laser fields: Frontiers of nonlinear optics.
Rev. Mod. Phys. **72**, 545–591 (Apr 2000).
URL `http://link.aps.org/doi/10.1103/RevModPhys.72.545`.

[50] P. Agostini and L. F. DiMauro.
The physics of attosecond light pulses.
Rep. Progr. Phys. **67**, 813–855 (2004).

[51] F. Krausz and M. Ivanov.
Attosecond physics.
Rev. Mod. Phys. **81**, 163–234 (Feb 2009).
URL http://link.aps.org/doi/10.1103/RevModPhys.81.163.

[52] C. Spielmann, P. F. Curley, T. Brabec, and F. Krausz.
Ultrabroadband Femtosecond Lasers.
IEEE J. Quantum Electron. **30**, 1100–1114 (1994).

[53] A. Stingl, M. Lenzner, C. Spielmann, F. Krausz, and R. Szipocs.
Sub-10-Fs Mirror-Dispersion-Controlled Ti-Sapphire Laser.
Opt. Lett. **20**, 602–604 (1995).

[54] R. Szipöcs, C. Spielmann, F. Krausz, and K. Ferencz.
Chirped multilayer coatings for broadband dispersion control in femtosecond lasers.
Optics Letters **19**, 201–203 (1994).

[55] D. H. Sutter, G. Steinmeyer, L. Gallmann, N. Matuschek, F. Morier-Genoud, U. Keller, V. Scheuer, G. Angelow, and T. Tschudi.
Semiconductor saturable-absorber mirror–assisted Kerr-lens mode-locked Ti: sapphire laser producing pulses in the two-cycle regime.
Optics Letters **24**, 631–633 (1999).

[56] U. Morgner, F. Kärtner, S.-H. Cho, Y. Chen, H. A. Haus, J. G. Fujimoto, E. P. Ippen, V. Scheuer, G. Angelow, and T. Tschudi.
Sub-two-cycle pulses from a Kerr-lens mode-locked Ti: sapphire laser.
Optics Letters **24**, 411–413 (1999).

[57] S. Kim, J. Jin, Y.-J. Kim, I.-Y. Park, Y. Kim, and S.-W. Kim.
High-harmonic generation by resonant plasmon field enhancement.
Nature **453**, 757–760 (June 2008).
URL http://dx.doi.org/10.1038/nature07012.

[58] A. Vernaleken, J. Weitenberg, T. Sartorius, P. Russbueldt, W. Schneider, S. L. Stebbings, M. F. Kling, P. Hommelhoff, H.-D. Hoffmann, R. Poprawe, F. Krausz, T. W. Hänsch, and T. Udem.
Single-pass high-harmonic generation at 20.8 MHz repetition rate.
Opt Lett **36**, 3428–3430 (Sep 2011).

[59] D. Strickland and G. Mourou.
Compression of Amplified Chirped Optical Pulses.
Opt. Commun. **56**, 219–221 (1985).

[60] S. Backus, C. G. Durfee, G. Mourou, H. C. Kapteyn, and M. M. Murnane.
0.2-TW laser system at 1 kHz.
Optics letters **22**, 1256–1258 (1997).

[61] *Ultrafast Innovations TOD mirrors*.
URL
http://www.ultrafast-innovations.com/index.php/third-order-dispersion-mirrors-

[62] M. Nisoli, S. De Silvestri, and O. Svelto.
Generation of high energy 10 fs pulses by a new pulse compression technique.
Appl. Phys. Lett. **68**, 2793–2795 (1996).

[63] M. Nisoli, S. DeSilvestri, O. Svelto, R. Szipocs, K. Ferencz, C. Spielmann, S. Sartania, and F. Krausz.
Compression of high-energy laser pulses below 5 fs.
Opt. Lett. **22**, 522–524 (1997).

[64] C. P. Hauri, A. Guandalini, P. Eckle, W. Kornelis, J. Biegert, and U. Keller.
Generation of intense few-cycle laser pulses through filamentation - parameter dependence.
Opt. Express **13**, 7541–7547 (2005).

[65] A. Couairon, J. Biegert, C. Hauri, W. Kornelis, F. Helbing, U. Keller, and A. Mysyrowicz.
Self-compression of ultra-short laser pulses down to one optical cycle by filamentation.
Journal of Modern Optics **53**, 75–85 (2006).

[66] R. Szipocs, K. Ferencz, C. Spielmann, and F. Krausz.
Chirped Multilayer Coatings for Broad-Band Dispersion Control in Femtosecond Lasers.
Opt. Lett. **19**, 201–203 (1994).

[67] A. Wirth, M. T. Hassan, I. GrguraÅą, J. Gagnon, A. Moulet, T. T. Luu, S. Pabst, R. Santra, Z. A. Alahmed, A. M. Azzeer, V. S. Yakovlev, V. Pervak, F. Krausz, and E. Goulielmakis.
Synthesized Light Transients.
Science **334**, 195–200 (2011).
URL `http://www.sciencemag.org/content/334/6053/195.abstract`.

[68] T. T. Luu.
Sub-cycle light transients from light synthesis.
private communications (2015).

[69] C. Manzoni, O. D. Mücke, G. Cirmi, S. Fang, J. Moses, S.-W. Huang, K.-H. Hong, G. Cerullo, and F. X. Kärtner.
Coherent pulse synthesis: towards sub-cycle optical waveforms.
Laser & Photonics Reviews **9**, 129–171 (2015).
URL `http://dx.doi.org/10.1002/lpor.201400181`.

[70] T. Popmintchev, M.-C. Chen, D. Popmintchev, P. Arpin, S. Brown, S. Alisauskas, G. Andriukaitis, T. Balciunas, O. D. Mücke, A. Pugzlys, A. Baltuska, B. Shim, S. E. Schrauth, A. Gaeta, C. Hernández-García, L. Plaja, A. Becker, A. Jaron-Becker, M. M. Murnane, and H. C. Kapteyn.
Bright coherent ultrahigh harmonics in the keV x-ray regime from mid-infrared femtosecond lasers.
Science **336**, 1287–1291 (Jun 2012).
URL `http://dx.doi.org/10.1126/science.1218497`.

[71] P. B. Corkum.
Plasma Perspective on Strong-Field Multiphoton Ionization.
Phys. Rev. Lett. **71**, 1994–1997 (1993).

[72] M. V. Ammosov, N. B. Delone, and V. P. Krainov.
Tunnel ionization of complex atoms and of atomic ions in an alternating electromagnetic filed.
Sov. Phys. JETP **64**, 1191–1194 (1986).

[73] S. Augst, D. D. Meyerhofer, D. Strickland, and S. L. Chin.
Laser Ionization of Noble-Gases by Coulomb-Barrier Suppression.
J. Opt. Soc. Am. B **8**, 858–867 (1991).

[74] A. D. Shiner, C. Trallero-Herrero, N. Kajumba, H.-C. Bandulet, D. Comtois, F. Légaré, M. Giguère, J.-C. Kieffer, P. B. Corkum, and D. M. Villeneuve.
Wavelength Scaling of High Harmonic Generation Efficiency.
Phys. Rev. Lett. **103**, 073902 (Aug 2009).
URL `http://link.aps.org/doi/10.1103/PhysRevLett.103.073902`.

[75] M. Chini, K. Zhao, and Z. Chang.
The generation, characterization and applications of broadband isolated attosecond pulses.
Nature Photon **8**, 178âĂŞ186 (Feb 2014).
URL `http://dx.doi.org/10.1038/NPHOTON.2013.362`.

[76] H. G. Kurz, D. S. Steingrube, D. Ristau, M. Lein, U. Morgner, and M. Kovačev.
High-order-harmonic generation from dense water microdroplets.
Physical Review A **87**, 063811 (2013).

[77] T. Fließbach.
Quantenmechanik - Lehrbuch zur Theoretischen Physik III.
4. Auflage. Elsevier, Spektrum Akademischer Verlag (2005).

[78] C. Cohen-Tannoudji, B. Diu, and F. Laloë.
Quantum Mechanics, volume II.
Wiley-Interscience (1977).

[79] M. Chini, X. Wang, Y. Cheng, Y. Wu, D. Zhao, D. A. Telnov, S.-I. Chu, and Z. Chang.
Sub-cycle Oscillations in Virtual States Brought to Light.
Sci. Rep. **3**, 1105 (2013).

[80] *NIST Atomic Spectra Database Levels Form*.
URL `http://physics.nist.gov/PhysRefData/ASD/levels_form.html`.

[81] A. Bürgers, D. Wintgen, and J.-M. Rost.
Highly doubly excited S states of the helium atom.
J. Phys. B **28**, 3163 (1995).

[82] M. Domke, K. Schulz, G. Remmers, G. Kaindl, and D. Wintgen.
High-resolution study of $^1P^o$ *double-excitation states in helium*.
Phys. Rev. A **53**, 1424–1438 (1996).

[83] K. Schulz, G. Kaindl, M. Domke, J. D. Bozek, P. A. Heimann, A. S. Schlachter, and J. M. Rost.
Observation of New Rydberg Series and Resonances in Doubly Excited Helium at Ultrahigh Resolution.
Phys. Rev. Lett. **77**, 3086–3089 (1996).

[84] U. Fano.
Effects of Configuration Interaction on Intensities and Phase Shifts.
Phys. Rev. **124**, 1866–1878 (1961).

[85] C. Cohen-Tannoudji, J. Dupont-Roc, G. Grynberg, and P. Thickstun.
Atom-photon interactions: basic processes and applications.
Wiley Online Library (1992).

[86] M. Schönwald.
Phase-matched few-cycle high-harmonic generation: ionisation gating and half-cycle cutoffs.
Diploma Thesis, Universität Heidelberg (2010).

[87] C. Ott.
Attosecond multidimensional interferometry of single and two correlated electrons in atoms.
Doctoral Thesis, Universität Heidelberg (2012).

[88] A. Kaldun.
Fano Resonances in the Time Domain - understanding and controlling the absorption and emission of light.
Doctoral Thesis, Universität Heidelberg (2014).

[89] Z. H. Loh, M. Khalil, R. E. Correa, and S. R. Leone.
A tabletop femtosecond time-resolved soft x-ray transient absorption spectrometer.
Rev. Sci. Instrum. **79**, 073101 (2008).

[90] R. Kienberger, E. Goulielmakis, M. Uiberacker, A. Baltuška, V. Yakovlev, F. Bammer, A. Scrinzi, T. Westerwalbesloh, U. Kleineberg, U. Heinzmann, M. Drescher, and F. Krausz.
Atomic transient recorder.
Nature **427**, 817–821 (2004).

[91] E. Goulielmakis, M. Uiberacker, R. Kienberger, A. Baltuška, V. Yakovlev, A. Scrinzi, T. Westerwalbesloh, U. Kleineberg, U. Heinzmann, M. Drescher, and F. Krausz.
Direct measurement of light waves.
Science **305**, 1267–1269 (2004).

[92] E. Goulielmakis, V. S. Yakovlev, A. L. Cavalieri, M. Uiberacker, V. Pervak, A. Apolonski, R. Kienberger, U. Kleineberg, and F. Krausz.
Attosecond control and measurement: Lightwave electronics.
Science **317**, 769–775 (2007).

[93] J. Ullrich and H. Schmidt-Böcking.
Time-of-flight spectrometer for the determination of microradian projectile scattering angles in atomic collisions.
Physics Letters A **125**, 193–196 (1987).

[94] J. Ullrich, R. Moshammer, A. Dorn, R. Dörner, L. P. H. Schmidt, and H. Schmidt-Böcking.
Recoil-ion and electron momentum spectroscopy: reaction-microscopes.
Reports on Progress in Physics **66**, 1463 (2003).

[95] N. Camus, B. Fischer, M. Kremer, V. Sharma, A. Rudenko, B. Bergues, M. Kübel, N. G. Johnson, M. F. Kling, T. Pfeifer, J. Ullrich, and R. Moshammer.
Attosecond Correlated Dynamics of Two Electrons Passing through a Transition State.
Phys. Rev. Lett. **108**, 073003 (Feb 2012).
URL `http://link.aps.org/doi/10.1103/PhysRevLett.108.073003`.

[96] L. Fechner, N. Camus, J. Ullrich, T. Pfeifer, and R. Moshammer.
Strong-Field Tunneling from a Coherent Superposition of Electronic States.
Phys. Rev. Lett. **112**, 213001 (May 2014).
URL `http://link.aps.org/doi/10.1103/PhysRevLett.112.213001`.

[97] L. Torlina, F. Morales, J. Kaushal, I. Ivanov, A. Kheifets, A. Zielinski, A. Scrinzi, H. G. Muller, S. Sukiasyan, M. Ivanov, et al.
Interpreting attoclock measurements of tunnelling times.
Nature Physics (2015).

[98] N. Dudovich, O. Smirnova, J. Levesque, Y. Mairesse, M. Y. Ivanov, D. Villeneuve, and P. B. Corkum.
Measuring and controlling the birth of attosecond XUV pulses.
Nature physics **2**, 781–786 (2006).

[99] H. Worner, J. Bertrand, D. Kartashov, P. Corkum, and D. Villeneuve.
Following a chemical reaction using high-harmonic spectroscop.
Nature **466**, 604–607 (2010).

[100] M. Joffre, D. Hulin, J. P. Chambaret, A. Migus, A. Antonetti, and C. Benoit a la Guillaume.
Bleaching of an Exciton Line Using Sub-T_2 Pulses: Artifact or Reality?
Ultrafast Phenomena VI (Springer Series in Chemical Physics Vol 48, p 223) (1988).

[101] M. Miranda, T. Fordell, C. Arnold, A. L'Huillier, and H. Crespo.
Simultaneous compression and characterization of ultrashort laser pulses using chirped mirrors and glass wedges.
Opt. Express **20**, 688–697 (Jan 2012).
URL `http://www.opticsexpress.org/abstract.cfm?URI=oe-20-1-688`.

[102] C. Iaconis and I. A. Walmsley.
Spectral phase interferometry for direct electric-field reconstruction of ultrashort optical pulses.
Opt. Lett. **23**, 792–794 (1998).

[103] D. Kane and R. Trebino.
Characterization of arbitrary femtosecond pulses using frequency-resolved optical gating.
Quantum Electronics, IEEE Journal of **29**, 571–579 (Feb 1993).

[104] *X-Ray Database*.
URL `http://henke.lbl.gov/optical_constants/`.

[105] Y. Mairesse and F. Quere.
Frequency-resolved optical gating for complete reconstruction of attosecond bursts.
Phys. Rev. A **71**, 011401 (2005).

[106] H. Muller.
Reconstruction of attosecond harmonic beating by interference of two-photon transitions.
Applied Physics B **74**, s17–s21 (2002).
URL http://dx.doi.org/10.1007/s00340-002-0894-8.

[107] S. Jennings.
The mean free path in air.
Journal of Aerosol Science **19**, 159 – 166 (1988).
URL
http://www.sciencedirect.com/science/article/pii/0021850288902194.

[108] P. Deuhard and A. Hohmann.
Numerische Mathematik. Eine algorithmisch orientierte Einführung (1991).

[109] J. Eckstein, A. Ferguson, and T. Hänsch.
High-resolution two-photon spectroscopy with picosecond light pulses.
Physical Review Letters **40**, 847 (1978).

[110] C. Gohle, T. Udem, M. Herrmann, J. Rauschenberger, R. Holzwarth, H. A. Schuessler, F. Krausz, and T. W. Hansch.
A frequency comb in the extreme ultraviolet.
Nature **436**, 234–237 (2005).

[111] R. J. Jones, K. D. Moll, M. J. Thorpe, and J. Ye.
Phase-coherent frequency combs in the vacuum ultraviolet via high-harmonic generation inside a femtosecond enhancement cavity.
Phys. Rev. Lett. **94**, 193201 (2005).

[112] J. Zhao and M. Lein.
Probing Fano resonances with ultrashort pulses.
New Journal of Physics **14**, 065003 (2012).
URL http://stacks.iop.org/1367-2630/14/i=6/a=065003.

[113] M. Chini, B. Zhao, H. Wang, Y. Cheng, S. X. Hu, and Z. Chang.
Subcycle ac Stark Shift of Helium Excited States Probed with Isolated Attosecond Pulses.
Phys. Rev. Lett. **109**, 073601 (Aug 2012).
URL http://link.aps.org/doi/10.1103/PhysRevLett.109.073601.

[114] W.-C. Chu and C. D. Lin.
Absorption and emission of single attosecond light pulses in an autoionizing gaseous medium dressed by a time-delayed control field.
Phys. Rev. A **87**, 013415 (Jan 2013).
URL http://link.aps.org/doi/10.1103/PhysRevA.87.013415.

[115] L. Argenti, R. Pazourek, J. Feist, S. Nagele, M. Liertzer, E. Persson, J. Burgdörfer, and E. Lindroth.
Photoionization of helium by attosecond pulses: Extraction of spectra from correlated wave functions.
Phys. Rev. A **87**, 053405 (May 2013).
URL http://link.aps.org/doi/10.1103/PhysRevA.87.053405.

[116] X. Wang, M. Chini, Y. Cheng, Y. Wu, X.-M. Tong, and Z. Chang.
Subcycle laser control and quantum interferences in attosecond photoabsorption of neon.
Phys. Rev. A **87**, 063413 (Jun 2013).
URL http://link.aps.org/doi/10.1103/PhysRevA.87.063413.

[117] M. Lucchini, J. Herrmann, A. Ludwig, R. Locher, M. Sabbar, L. Gallmann, and U. Keller.
Role of electron wavepacket interference in the optical response of helium atoms.
New Journal of Physics **15**, 103010 (2013).
URL http://stacks.iop.org/1367-2630/15/i=10/a=103010.

[118] Y. Tanimura and S. Mukamel.
2-Dimensional Femtosecond Vibrational Spectroscopy of Liquids.

J. Chem. Phys. **99**, 9496–9511 (1993).

[119] M. C. Asplund, M. T. Zanni, and R. M. Hochstrasser.
Two-Dimensional Infrared Spectroscopy of Peptides by Phase-Controlled Femtosecond Vibrational Photon Echoes.
Proc. Natl. Acad. Sci. USA **97**, 8219–8224 (2000).

[120] D. M. Jonas.
Two-dimensional femtosecond spectroscopy.
Annu. Rev. Phys. Chem. **54**, 425–463 (2003).

[121] M. Cho.
Coherent Two-Dimensional Optical Spectroscopy.
Chemical Reviews **108**, 1331–1418 (2008).
URL `http://dx.doi.org/10.1021/cr078377b`.
PMID: 18363410.

[122] I. V. Schweigert and S. Mukamel.
Coherent Ultrafast Core-Hole Correlation Spectroscopy: X-Ray Analogues of Multidimensional NMR.
Phys. Rev. Lett. **99**, 163001 (2007).

[123] A. M. Zheltikov, A. A. Voronin, M. Kitzler, A. Baltuška, and M. Ivanov.
Optical Detection of Interfering Pathways in Subfemtosecond Multielectron Dynamics.
Phys. Rev. Lett. **103**, 033901 (2009).

[124] M. Aymar, C. H. Greene, and E. Luc-Koenig.
Multichannel Rydberg spectroscopy of complex atoms.
Reviews of Modern Physics **68**, 1015 (1996).

[125] S. H. Autler and C. H. Townes.
Stark Effect in Rapidly Varying Fields.
Phys. Rev. **100**, 703–722 (1955).

[126] M. Wu, S. Chen, M. B. Gaarde, and K. J. Schafer.
Time-domain perspective on Autler-Townes splitting in attosecond transient absorption of laser-dressed helium atoms.
Physical Review A **88**, 043416 (2013).

[127] D. Ederer and M. Manalis.
Photoabsorption of the 4d electrons in xenon.
JOSA **65**, 634–637 (1975).

[128] S. Pabst and H. J. Wörner.
Can strong-field ionization prepare attosecond dynamics?
arXiv:1506.98929 (2015).

[129] T. Witting, F. Frank, C. A. Arrell, W. A. Okell, J. P. Marangos, and J. W. Tisch.
Characterization of high-intensity sub-4-fs laser pulses using spatially encoded spectral shearing interferometry.
Optics letters **36**, 1680–1682 (2011).

[130] G. Stibenz and G. Steinmeyer.
Interferometric frequency-resolved optical gating.
Optics express **13**, 2617–2626 (2005).

[131] C. Iaconis, I. Walmsley, et al.
Self-referencing spectral interferometry for measuring ultrashort optical pulses.
Quantum Electronics, IEEE Journal of **35**, 501–509 (1999).

[132] B. Xu, J. Gunn, J. D. Cruz, V. Lozovoy, and M. Dantus.
Quantitative investigation of the MIIPS method for phase measurement and compensation of femtosecond laser pulses.
J. Opt. Soc. Am. B **23**, 750–759 (2006).

[133] M. Chini, S. Gilbertson, S. D. Khan, and Z. Chang.
Characterizing ultrabroadband attosecond lasers.
Optics express **18**, 13006–13016 (2010).

Danksagung

Zum Abschluss meiner Dissertation möchte ich mich bei allen ganz herzlich bedanken, die mich vom Beginn meiner Arbeit am 2.11.2012 bis zur Abgabe am 2.11.2015 unterstüzt haben.

Ganz besonders möchte ich mich bei Thomas Pfeifer bedanken, dafür dass er mir die Möglichkeit gegeben hat, in seiner Gruppe zu promovieren. Danke für die vielen guten Ideen, das Vertrauen, und die Untersützung die ich in den letzten drei Jahren erfahren habe. Insbesondere nach deiner Ernennung zum Direktor, mit der ein Meer aus neuen Aufgaben auf dich zu gekommen ist, hast du dir immer noch viel Zeit für Diskussionen und Hilfestellungen genommen.

Ebenfalls möchte ich mich sehr bei Adrian Pálffy-Buß dafür bedanken, dass Sie meine Arbeit begutachtet.

Ich möchte mich bei allen Mitgliedern der Interatto/X-MuSiC Gruppe ganz herzlich bedanken! Sowohl für die vielen Stunden die wir gemeinsam im Labor verbracht haben als auch für vielen Anregungen und "fruitful discussions". Nicht zu vergessen der viele Spaß den wir auch abseits der Atome, Laser und Vakuumkammern beim Grillen und gelegentlichen Tischkickerspielen hatten. Zu guter Letzt habt ihr mir durch das lesen meiner Arbeit sehr geholfen! Vielen Dank Andreas Kaldun, Kristina Meyer, Huipeng Kang, Martin Laux, Zuoye Liu, Yonghao Mi, Thomas Ding, Veit Stooß, Marc Rebholz, Max Hartmann, Paul Birk, und Lennart Aufleger. Um es im Jargon der Gruppe zu sagen: die Zeit mit euch war/ist "outstanding".

Besonders möchte ich mich noch bei Christian Ott bedanken, von dem ich im ersten Jahr sehr viel gelernt habe, und für die coole Woche die wir in der Bay Area und der Sierra Nevada verbracht haben.

Außerdem möchte ich mich bei allen Mitgliedern der Abteilung Quantum Dynamics & Control bedanken: für die hilfreichen Gespräche und Leihgaben von Laborequipment, sowie die sehr angehme Arbeitsatmosphäre.

Stellvertretend für alle, die bei der Planung und Realisierung größerer und kleinerer Projekte beteiligt waren, möchte ich Herrn Weber danken, der mit seinen herausragenden CAD-Fertigkeiten das Attosecond-Streak-Camera Projekt bereichert hat.

Ich möchte mich herzlichst bei meiner Schwester Isi, meinen Eltern Gundula und Matthias, und meinen Schwiegereltern Sylke und Tom, für die Unterstützung und all die schönen Stunden dir wir trotz der recht großen Entfernungen in den letzten drei Jahren hatten, bedanken.

Am allermeisten möchte ich mich bei meiner Freundin, und nun Frau, Julia bedanken. Die gemeinsame Zeit in Heidelberg, die vielen Reisen, und unsere Hochzeit haben die letzten drei Jahre für mich so schön gemacht, dass ich es nicht in Worte fassen kann. Egal ob nach einem anstrengenden Tag am Laser oder nach stundenlangem Überlegen und Rechnen - wenn ich nach Hause komme und du da bist, ist alles vergessen und ich bin einfach nur glücklich.